Electrical studies on hybrid MIS structures incorporating CdS nanoparticles in organic films.

MOHAMAD, Syed A.M.S.

Electrical Studies on Hybrid MIS Structures Incorporating CdS Nanoparticles in Organic Films

SYED ABDUL MALIK SYED MOHAMAD

A thesis submitted in partial fulfilment of the requirements of

Sheffield Hallam University

for the degree of Doctor of Philosophy

April 2005

DEDICATION

To Aiman, Aqif, and Afif… my lovely sons, who put strength in my life.

To my beloved wife, Zarina… who is always supportive.

To my beloved mother... Sharifah Noor Sahabuddin, who always make du'a for me.

To all my family in Malaysia, who are right now thinking about me,

and

to my beloved late father,... Syed Mohamad bin Syed Yassin Alqadri, whom is not here to celebrate my success.

ABSTRACT

This project involves the investigation of a.c. and d.c. electrical characterisations and low-frequency noise properties of Langmuir-Blodgett (LB) films in metal-insulator-semiconductor (MIS) structure. Two types of insulating films based on hybrid organic-inorganic materials sandwiched between metal and semiconductor were fabricated. The original insulating films (untreated) were 40 layers Y-type LB films of Cd-salt stearic acid ($CdSt_2$). The second type of insulating films were formed after the treatment of $CdSt_2$ films with H_2S gas over a period of 12 hours at room temperature to grow CdS nanoparticles within the stearic acid matrix (treated).

The capacitance-voltage (C-V) measurement of $CdSt_2$ LB films exhibit significant dependence on the measurement frequency in the accumulation region due to high d.c. leakage currents. By embedding CdS nanoparticles into the stearic acid matrix, less frequency dependent C-V curves were obtained. The problem in determining the true insulator capacitance due to frequency dispersion was overcome by using the Yang's model. The corresponding dielectric constant of LB films of $CdSt_2$ was found to be 2.3 and increased to 5.1 when embedded with CdS nanoparticles. The results from the dielectric loss measurement show that both devices agree well with Goswami and Goswami model. By incorporating CdS nanoparticles in the stearic acid matrix, the dielectric loss was found to increase which could be due to electrons being trapped by the CdS nanoparticles.

A large current density was observed in the untreated devices at room temperature giving evidence of a leaky dielectric. The analysis of the temperature dependent I-V characteristics shown that current is independent of temperature, similar to the results published by several researchers which explained the current conduction mechanism in term of electron hopping and tunnelling through each bilayer of the LB films. In contrast, by embedding the CdS nanoparticles in the stearic acid matrix the currents have reduced by one-order of magnitude. The temperature dependence of the I-V characteristics showed the dependence of current on the device temperature at low electric field densities whilst less temperature dependence was observed at higher electric field density. Further investigation into the carrier transport mechanism, has found that the Poole-Frenkel effect was the dominant mechanism in the treated devices.

A low frequency noise measurement setup has been designed and validated. The results of low-frequency noise measurement reported here are new. $1/f$ noise was the only low-frequency noise observed in treated and untreated devices for frequencies up to 1kHz. The current noise spectral density $S_I(f)$, was found to fit well with the modified Hooge's empirical model; $S_I(f)=C\frac{I^\beta}{f^\gamma}$, where C, I, and f are noise magnitude, current and frequency respectively. The exponential values of γ and β were found to lie within the acceptable ranges of $0.7 \le \gamma \le 1.4$ and $1 \le \beta \le 3$ respectively. The current noise power spectral density (PSD) at several fixed bias current was found to be dependent on the bias current with the PSDs for treated devices found to be approximately two-orders of magnitude higher. These results show that low-frequency noise measurement can be used to probe into the microstructure of the electron devices. It is believed that by embedding the CdS nanoparticles into the stearic acid matrix, electron trapping centres have been created which result in different current conduction behaviour from the untreated LB films of cadmium stearate.

ACKNOWLEDGEMENTS

First and foremost, I thank Allah, the all Mighty for giving me the strength to be able to complete this thesis.

I would like to thank the Public Service Department, Malaysia (JPA) and Universiti Pendidikan Sultan Idris (UPSI) for awarding me the scholarship which has made it possible for me to study for a PhD degree at this university.

I would also like to thank my director of studies, Prof. Asim K. Ray for his supervision, guidance and support during my study, and for introducing me to the low-frequency noise measurement (LFNM) which is hard at the beginning, but interesting in the end. I have learnt a lot from his comments and suggestions, which are always very inspiring and fruitful.

My special appreciations and thanks must go to my supervisor Dr Aseel Hassan and Dr Alexei Nabok, for their advice, encouragement, assistance and help especially in the early part of my research.

I would like to take this opportunity to thank all my fellow PhD colleagues whom I am truly indebted, especially to Alistair Vale, for proof reading my thesis, Alan Holloway, who helped me with Labview programs, Abbas Hashim, Anna Tsargorodskaya, Iwantono (Dr), Najla and my country mate Saharuddin Haron for their help and support.

I would also like to thank the visiting researcher Dr Rifat Capan for valuable information, discussions, and suggestions regarding the LB deposition technique. Also to all technical staff especially Ken Duty and Robert Grant for making PCBs and metal shield boxes used in LFNM.

My special thanks go to my Swedish internet mate, Dr. Staffan Bruce for spending his valuable time discussing the LFNM results.

Last but not least, I want to express a heart-felt 'thank you' to my lovely mother, my dearest wife, my charming sons and my supportive families back home for their continuous du'a, patience, and love throughout my difficult years.

LIST OF PUBLICATIONS

Journal Publications

1. ”*Nanocomposite organic films on silicon*”, published in the IEEE Transactions on Nanotechnology, Sept. 2003, vol. 2, number 3, p149-153, 2003.
2. *“1/f noise in Langmuir Blodgett films on silicon”,* published in the Semiconductor Science and Technology, vol. 20, issue 5, p.453-458, 2005.

Conference Publications

1. "***CdS nanoparticles embedded in Metal-Insulator-Semiconductor structures***" presented at the IEEE NANO, 2002, Washington DC, USA.
2. "***Electrical properties of LB films embedded with CdS nanoparticles in MIS structure***", presented at the the 3rd International Conference on Advances in Strategic Technologies (ICAST), 12–14th August 2003, Kuala Lumpur, Malaysia. **- PRIZE WINNER**
3. “***Electrical transport studies of Langmuir-Blodgett films embedded with CdS nanoparticles in metal-insulator-semiconductor structure***", presented at the Postgraduate Research in Electronics, Photonics, Communications and Software (PREP) Conference, 14-16th April 2003, University of Exeter, UK.
4. "***1/f noise in Langmuir-Blodgett thin films***", presented at the Postgraduate Research in Electronics, Photonics, Communications and Software (PREP) Conference, 5-7th April 2004, University of Hertfordshire, UK.

CONTENTS

Dedication i
Abstract ii
Acknowledgements iii
List of publications iv
Contents v
List of figures viii
List of tables xiii

CHAPTER 1

Introduction 1
1.1 Background 1
1.2 Aims and objectives 3
1.3 Organisation of the thesis 4

CHAPTER 2

Theoretical Background and General Review 6
2.1 Langmuir-Blodgett (LB) Films 6
    2.1.1 Basic concepts of LB technique 6
    2.1.2 Surface Pressure-Area Isotherms 9
    2.1.3 Film deposition 11
    2.1.4 Applications of LB films 14
2.2 Metal-insulator-semiconductor (MIS) capacitor 19
    2.2.1 The ideal MIS equivalent circuit and energy-band diagram 20
    2.2.2 Capacitance-voltage of a leaky dielectric material 26
    2.2.3 Yang's model 28
2.3 Leakage current in insulating films 31
    2.3.1 Schottky emission 34
    2.3.2 Poole-Frenkel effect 36
    2.3.3 Fowler-Nordheim tunnelling 41
    2.3.4 Space-charge-limited conduction 43

2.4 Noise in electron devices 46
2.4.1 Thermal noise 47
2.4.2 Shot noise 49
2.4.3 Generation-Recombination (G-R) noise 51
2.4.4 Flicker (1/f) noise 53
2.4.5 1/f noise models 54
2.4.5.1 McWhorter's number fluctuations model 55
2.4.5.2 Hooge's mobility fluctuations model 59
2.4.5.3 Unified Model 61

CHAPTER 3

Experimental Methodology 63
3.1 Introduction 63
3.2 Device fabrication 64
3.2.1 Substrate preparation 64
3.2.2 Film deposition 66
3.2.3 CdS nanoparticles formation 67
3.2.4 Electrical contacts 68
3.3 Leakage current measurement 71
3.4 Low-frequency noise measurement (LFNM) 73
3.4.1 Measurement system design 74
3.4.2 Averaging and Windowing 85
3.4.3 Wide-band measurements 87
3.4.4 Validation of the system performance 89

CHAPTER 4

Admittance Spectroscopy: Results and Discussion 91
4.1 Introduction 91
4.2 Capacitance-voltage (C-V) measurements 92
4.3 Admittance measurements 101
4.3.1 Dielectric loss: Room temperature 102
4.3.2 Dielectric loss: Temperature dependence 107
4.3.3 Cole-Cole (Nyquist) plot 111
4.4 Summary 113

CHAPTER 5

DC Analysis of Leakage Current: Results and Discussion 114
5.1 Introduction 114
5.2 Transport mechanism: Room temperature 115
5.3 Detailed analysis of conduction through LB films 120
5.4 Temperature dependence and activation energy 130
5.5 Summary 138

CHAPTER 6

Low Frequency Noise Measurement: Results and Discussion 139
6.1 Introduction 139
6.2 Current noise spectral density 140
6.3 Parameters extraction 148
6.4 Summary 162

CHAPTER 7

Conclusions and further work 163
7.1 Thesis summary 163
7.2 Contribution to new knowledge 166
7.3 Suggestions for further work 167

References 169

LIST OF FIGURES

Figure 1.1 Comparing various wet technologies for preparing ultrathin organic films (after [Lvov and Decher 1994]) 2

Figure 2.1 Molecular structure of stearic acid (n-octadecanoic) with n=18. The approximate geometrical shape and dimensions of the molecule are shown on the right. (after [Petty 1996]) 8

Figure 2.2 Reaction of Cd^{2+} with an alkanoic acid group. 9

Figure 2.3 Surface pressure versus area per molecule for stearic acid. 11

Figure 2.4 Deposition of first monolayer onto; (a) hydrophilic substrate (upward); (b) hydrophobic substrate (downward) 12

Figure 2.5 Deposition types of LB films (a) X-type (b) Y-type (c) Z-type (d) Alternate Y-type 13

Figure 2.6 Y- type deposition onto hydrophobic substrate (e.g. silicon wafer). 14

Figure 2.7. Hopping process in the multilayer system. An electron moves about the system, sometimes along the interface, sometimes transversing the hydrocarbon barrier, to drift stochastically towards the positive electrode [after Sugi 1985]. 16

Figure 2.8. An ideal metal-insulator-semiconductor capacitor showing a simple equivalent circuit. The capacitor labeled C_S is shown variable to denote its bias dependence. 20

Figure 2.9 Flatband energy diagram of an ideal MIS structure consisting of aluminum metal/insulator/n-type silicon. 22

Figure 2.10 Illustration of the energy-band diagrams of a metal-insulator-semiconductor capacitor in several regimes. (a) accumulation (b) depletion and (c) inversion. E_C and E_V are the energy values at the conduction and valence band edges respectively. E_{FS} and E_{FM} are the Fermi level in the metal and semiconductor respectively. 23

Figure 2.11 Energy-band diagram at the surface of a n-type semiconductor in the inversion region: At the onset of strong inversion the surface potential ψ_S is twice the value of ψ_B in the neutral n-type semiconductor. 25

Figure 2.12 (a) Parallel configuration for small series resistance R, and (b) series configuration for low leakage current, both as modelled by commercial LCR meters. (c) The three-element circuit model of a real capacitor. 27

Figure 2.13 Coulombic potential well in the presence of an electric field illustrating the Poole-Frenkel effect [after Harrel and Frey 1999]. **38**

Figure 2.14 Effect of applied voltage on energy band diagram of MOS structure (a) Fowler-Nordheim and (b) direct tunneling. Note the difference in the barrier shapes. **43**

Figure 2.15 Space-charge-limited current (SCLC) versus voltage characteristics for an insulator containing traps. V_{TFL} is the trap-filled limit voltage. **46**

Figure 2.16 Thermal noise model of a complex two terminal network, (a) voltage noise model (b) current noise model. **50**

Figure 3.1. Processes in substrate preparation. **65**
(a) n type silicon wafer with top surface grown with SiO_2
(b) silicon wafer in (a) cut to the size of a microscopic glass slide
(c) part of SiO_2 in (b) were etched using hydrofluoric acid, resulting in bare silicon area approximately 76mm ×15 mm.

Figure 3.2 A metal plate mask used for top contacts. **69**

Figure 3.3 A schematic diagram of a fabricated device in MIS structure. **70**

Figure 3.4 Equivalent circuit model of MIS device in Figure 3.3. **71**

Figure 3.5 Schematic diagram of the electrical characterisation system **72**

Figure 3.6 Schematic diagram of a low-frequency noise measurement setup **76**

Figure 3.7 A photo of a LFNM setup. The inner metal box and the transimpedance amplifier were inside the black metal box. **76**

Figure 3.8 Noise equivalent model of the measurement setup. $i_{DUT}(t)$ and $i_A(t)$ are the current noise equivalent generators of the device under test and of the amplifier respectively. **77**

Figure 3.9 Schematic model of the transimpedance amplifier including the equivalent resistance of the device under test at the input (R_{DUT}). **77**

Figure 3.10 Current noise PSD of transimpedance amplifier with different gain setting. **79**

Figure 3.11 Printed circuit board layout. **80**

Figure 3.12 Background voltage noise power spectral density of transimpedance amplifier and dynamic signal analyzer. **82**

Figure 3.13 LabView panel window for acquiring PSDs data. **83**

Figure 3.14 LabView program diagrams windows for acquiring PSDs data. **84**

Figure 3.15 The effects of averaging on the PSDs data. 86
(a) Without any averaging
(b) 10 times averaging
(c) 50 times averaging
(d) 100 times averaging

Figure 3.16 Wide-frequency measurement with (a) one and (b) three frequency bands. 88

Figure 3.17 Validation of the measurement set-up. 90

Figure 4.1 Capacitance versus voltage (C-V) characteristics of untreated devices at different frequencies. 94

Figure 4.2 Capacitance versus voltage (C-V) characteristics of treated devices at different frequencies. 94

Figure 4.3 Simulated C-V characteristics obtained by using Yang's technique. 97

Figure 4.4 Capacitance per unit area versus modulating frequency for treated and untreated devices. 103

Figure 4.5 AC conductivity versus modulating frequency for treated and untreated devices. 104

Figure 4.6 Dielectric loss as a function of modulating frequency for treated and untreated devices measured at room temperature. 106

Figure 4.7 Capacitance and AC conductance of treated (SA+CdS) and untreated (SA) devices as a function of signal frequency at temperature between 80K and 380K. 107

Figure 4.8 Dielectric loss as a function of modulating frequency for untreated device (SA) measured at four difference temperatures. 109

Figure 4.9 Dielectric loss as a function of modulating frequency for treated device (SA+CdS) measured at four difference temperatures. 110

Figure 4.10 Dielectric loss as a function of temperature of treated (SA+CdS) and untreated (SA) devices at two difference frequencies, 900Hz and 1MHz. 110

Figure 4.11 Nyquist plot of the experimentally measured admittance of treated device:- conductance normalized to the angular frequency versus capacitance. The points show the experimental data, the curve is a fit to a second-order polynomial. 112

Figure 5.1. A schematic structure diagram of a fabricated device. The LB film is 40 layers of stearic acid incorporating cadmium ions ($CdSt_2$). The film thickness is approximately 100nm. 116

Figure 5.2 I-V characteristic for untreated and treated devices in log-linear scale at room temperature. A, B and C are the accumulation, depletion and inversion regions respectively. **117**

Figure 5.3 Three resistor model. **118**

Figure 5.4 Log I versus Log V for treated (SA+CdS) and untreated (SA) devices. The slope (m) for each region is shown in bracket. **122**

Figure 5.5 Leakage current characteristics of treated (region A and B) and untreated (region A) devices plotted as $\ln(I/V^2)$ against $1/V$ for possibility of Fowler-Nordheim tunnelling. **124**

Figure 5.6 Plot of $\ln I$ versus $V^{1/2}$ for dark forward bias current-voltage charac-teristics of LB films for both untreated and treated samples at room ambient temperature. **129**

Figure 5.7 Log-linear scale of forward leakage current for SA and SA+CdS over temperature range between 80K and 380K. The temperature is set at 80K, 130K, 180K, 230K, 280K, 300K, and 380K. Arrows (→) show the increase in temperature. **131**

Figure 5.8 Plot of ln J versus 1000/T for untreated device at several bias voltage (a) 0.7V, (b) 1.0V, (c) 1.5V, (d) 2.0V, (e) 2.5V and (f) 3.0V **133**

Figure 5.9 Plot of ln J versus 1000/T for treated device at several bias voltage (a) 0.7V, (b) 1.0V, (c) 1.5V, (d) 2.0V, (e) 2.5V and (f) 3.0V **133**

Figure 5.10 Plot of log J vs 1000/T for untreated [(b) and (d)] and treated devices [(a) and (c)] at 1V [(a) and (c)] and 2.5V [(b) and (d)]. **135**

Figure 5.11 A plot of $\ln G$ vs $1000/T$ for the SA+CdS nanocomposite films at V=1.5V. **137**

Figure 6.1 The measured ac conductance (G) of the treated and untreated devices. **142**

Figure 6.2. The measured system background (Johnson) noise for (a) untreated device and (b) treated device. **143**

Figure 6.3 Forward bias I-V characteristics of treated (SA+CdS) and untreated (SA) devices in regime of interest A and B. **144**

Figure 6.4 Current noise spectral density for untreated devices. System background noises are shown as reference. **146**

Figure 6.5 Current noise spectral density for treated devices. System background noises are shown as reference. **147**

Figure 6.6 The dependence of exponent γ in the $1/f^{\gamma}$ spectrum on the bias current for frequency range 1 to 1 kHz for (a) untreated and (b) treated devices. **152**

Figure 6.7 Trap distribution parameter, E_t as a function of leakage current for (a) untreated and (b) treated devices, corresponding to γ in fig.6.6. **153**

Figure 6.8 Current noise spectral density versus leakage current for untreated devices. **155**

Figure 6.9 Current noise spectral density versus leakage current for treated device. **157**

Figure 6.10 $1/f$ noise magnitude as a function of leakage current for untreated devices. **159**

Figure 6.11 $1/f$ noise magnitude as a function of bias current for treated devices. **159**

Figure 6.12 AFM image of 8-layer of Cd-salt LB films (a) before and (b) after H_2S treatment [after Iwantono 2003]. **161**

LIST OF TABLES

Table 2.1 Long chain fatty acid compounds commonly used in the LB technique. **7**

Table 2.2 Basic conduction processes in insulators (after [Sze 1981). **33**

Table 2.3 The brief relationship between defect model and basic conduction processes (after [Lin 1990]). **34**

Table 3.1 Maximum dc current and noise current at each sensitivity. **79**

Table 4.1 Parameters derived from C-V measurement. **101**

Table 5.1 The extracted resistances of the untreated and treated devices. **120**

Table 5.2. Tunnelling metal-insulator barrier height of the treated and untreated devices. **124**

Table 5.3. Poole-Frenkel and Schottky coefficients for treated device in region A and B. **129**

Table 5.4. Poole-Frenkel and Schottky coefficients for untreated device. **130**

Table 5.5. Activation energy of untreated (SA) and treated (SA+CdS) devices for two different ranges of temperature and at two different bias voltages. **135**

Table 6.1 1/f noise parameter for untreated (SA) and treated (SA+CdS) devices. **160**

CHAPTER 1

Introduction

1.1 Background

Silicon wafer is widely dominating the microelectronics industry due to its stability and low manufacturing cost making it technologically an important substrate. By depositing organic thin films directly on top of the silicon surface, the formed electron devices can be tuned through precise control of the insulating layers. Central to the application of organic films in electron devices is the electrical properties of the monolayers. The metal-insulator-semiconductor (MIS) devices can be produced by using a hybrid organic-inorganic composite film as the dielectric material which offers a wide range of interesting applications especially in optoelectronics. By embedding semiconductor nanoparticles such as cadmium sulphide (CdS) into the organic films matrix, a device with novel electrical and optical properties is created.

The organic materials can be deposited by using the conventional dry method such as molecular beam epitaxy (MBE), and sputtering technique. MBE is a highly sophisticated and precise technique used for the deposition of thin film and inorganic nanoparticles. However it is very costly. In the sputtering technique, although the film thickness can be controlled easily by adjusting the sputtering time, RF power, gas pressure and flow rate, the control of the molecular orientation on the substrate is difficult [Petty et al 1995].

An alternative technology is by using low cost wet technology such as chemical bath deposition, electrodeposition, spin-coating and Langmuir-Blodgett (LB). Out of these, the LB technique has proved to be the most promising method for the preparation of organic thin films [Grunfeld 1993]. This is primarily due to the their variable layer architecture with a high degree of molecular order and the exact control of the films thickness [Grisser et al 1992]. Figures 1.1 compares the methods used for assembly of ultra thin films with various degrees of molecular order and stability (due to mechanical strength) which shows the advantages of the LB technique. The optimum combination or molecular order and stability of films obtained usually determine the usefulness of these technologies.

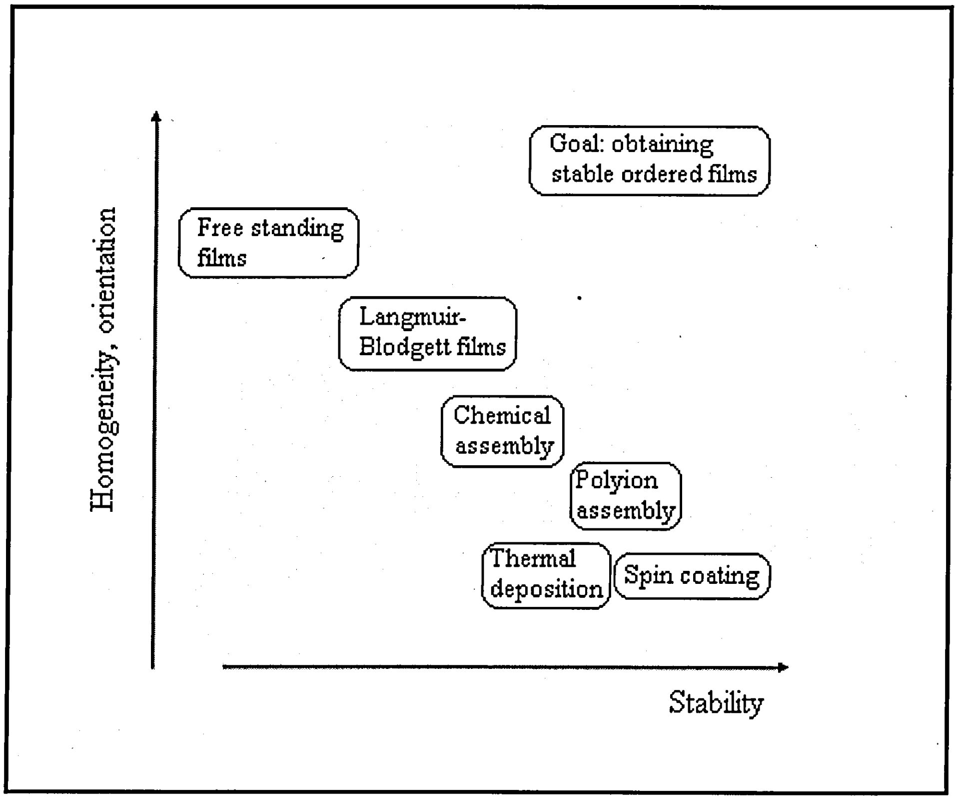

Figure 1.1 Comparing various wet technologies for preparing ultra thin organic films (after [Lvov and Decher 1994])

The metal-insulator-semiconductor (MIS) structure is an important part of many semiconductor devices. The presence of a dielectric material between two conductors gives the device the properties of a capacitor. The capacitance-voltage measurement is a powerful way to investigate the quality of the dielectric and the quality of the insulator-semiconductor interface [Ouennoughi 1997].

The knowledge of the electrical conduction of LB layers is not fully understood because this depends on several parameters such as molecular structure and multilayer architecture. Furthermore, the knowledge of the conduction mechanisms of LB films containing CdS nanoparticles is still lacking since most of the investigations are focused on the structural morphologies and optical properties. On top of that, the study of low-frequency noise in LB films is hardly reported. Low-frequency noise in semiconductor devices is a vital topic for investigation in view of the fact that it is associated with fluctuations in the electrical conductance and is important in low-level signal applications. Low-frequency noise measurement (LFNM) can be a means of probing and understanding electronic processes occurring within LB films in MIS structures. The results can be used in the estimation and prediction of the electron device reliability [Jevtic 1995].

1.2 Aims and Objectives

The main purpose of the research is to study the a.c. and d.c. characteristics and the low-frequency noise properties of the hybrid organic-inorganic LB films in MIS structure with and without incorporating CdS nanoparticles. The organic and inorganic material used were stearic acid and cadmium ions (Cd^{2+}) respectively. In order to achieve these goals the objectives of this research are listed below.

1. To fabricate MIS capacitors of LB films of stearic acid incorporating
    (i) Cadmium ions (untreated device)
    (ii) CdS nanoparticles (treated device).

2. To design and validate a low-frequency noise measurement (LFNM) setup.

3. To study the a.c. and d.c. electrical properties of the produced samples such as, a.c conductance and capacitance, dielectric constant and dielectric loss and d.c. current transport mechanisms at room temperature and over the temperature range extending from 80K up to 380K.

4. To investigate the 1/f noise properties in the produced devices at room temperature using the LFNM technique.

1.3 Organisation of the Thesis

The thesis is presented in seven chapters with the current chapter presents the introduction to the thesis.

Chapter 2, which comprises four sections, provides the physical theories and mathematical models related to this study. It begins with brief theory of Langmuir-Blodgett thin film deposition technique briefly described in section 2.1. Section 2.2 is devoted to the basic theory of the metal-insulator-semiconductor (MIS) capacitor which is the structure of the device used in this study. Section 2.3 describes the typical current transport mechanisms as observed in leaky insulating materials Finally, the noise in electron devices and the related 1/f noise models are discussed in section 2.4.

Chapter 3 is devoted to sample preparation and experimental methodology used in this study. The procedures followed in the fabrication of the device are discussed in detail and the measurement techniques employed for device characterizations are fully explained. Emphasis is given to the design of the low-frequency noise setup for use in noise characterization.

The experimental results and data analysis are presented in the next three chapters. The admittance spectroscopy measurement results are discussed in chapter 4 with emphasis given to C-V measurements. A mathematical model which is widely used in determining the oxide thickness of the MOS devices affected by large leakage current has been successfully adapted for estimating the dielectric constant of the LB films. The results for both devices (treated and untreated) are compared and conclusions are drawn.

Chapter 5 presents the experimental results of leakage current in LB films of stearic acid. Due to the fact that the current transport mechanism in LB films of cadmium stearate ($CdSt_2$) is already known, emphasis was given to determination of the current transport mechanisms in treated devices. Data were analysed and the possible current transport mechanism is proposed.

The results obtained from low-frequency noise measurement for treated and untreated devices are presented in chapter 6. The 1/f noise properties were investigated and their results were compared. This is believed to be the first reported finding on low-frequency noise measurements for LB film devices.

Finally in chapter 7, the thesis is summarized with conclusions and suggestions for further work.

CHAPTER 2

Theoretical Background and General Review

2.1 Langmuir-Blodgett (LB) films

The LB-technique is found to be one of the most promising methods for preparing organic thin films. This method is usually used to fabricate highly ordered ultra thin films of various organic materials based on amphiphilic molecules. It has some advantages such as precise control of the monolayer thickness, homogeneous deposition of the monolayer over large areas and the possibility to make multilayer structures with varying layer composition [Bykov 1996]. An additional advantage of the LB technique is that monolayer can be deposited on almost any kind of solid substrate. Nowadays molecular coating on solid surfaces is important in physics, chemistry, material science, and electronics with potential application in optoelectronic devices such as sensors and transducers.

2.1.1 Basic Concepts of the LB Technique

The Langmuir-Blodgett (LB) technique involves the transfer of single monolayer of water-insoluble organic material, floating on the water surface at a certain fixed surface pressure, onto a suitable solid substrate by dipping the substrate through an air-liquid interface. The resulting LB films can be either a single monolayer, multilayer or alternate layers. The basic requirement for the preparation of a floating single monolayer is a clean and enclosed water surface. That means the quality of water used in LB film work is of utmost important and impurities on the water surface can be a problem. The normally accepted practice is to use water from a reverseosmosis/deionising system. The LB technique requires film forming materials known as "surface active substances" (or surfactants) to be trapped at the interface between two dissimilar phases, either liquid-liquid or liquid-gas. Surface active substances are amphiphilic molecules; molecules which are composed of hydrophilic ("water loving") headgroup and hydrophobic ("water hating") tail. A classic monolayer forming material suitable for LB film is a fatty acid with long alkyl chain and carboxylic headgroup. Table 2.1 lists some of the common fatty acids which can be used for monolayer studies. Figure 2.1 shows the chemical structure of n-octadecanoic acid or commonly known as stearic acid [$CH_3(CH_2)_{n-2}COOH$] where n=18, (or $C_{17}H_{35}COOH$) one of the well known film forming materials used in LB deposition technique.

Structure	Chemical name	Common name	Melting point, °C
$C_{15}H_{31}COOH$	n-hexadecanoic	Palmitic	63
$C_{17}H_{35}COOH$	n-octadecanoic	Stearate	71
$C_{19}H_{39}COOH$	n-eicosonoic	Arachidic	77
$C_{21}H_{43}COOH$	n-docosonoic	Behenic	80

Table 2.1 Long chain fatty acid compounds commonly used in LB technique.

The stearic acid molecule consists of sixteen CH_2 groups forming a long hydrocarbon chain with one end of the chain terminated with a COOH group. The molecule is flexible and has cylindrical shape with length and cross-sectional area of approximately $2.5\,\text{nm}$ and $0.19\,\text{nm}^2$ respectively [Petty 1996]. The hydrocarbon part $-CH_2-$ of the molecule is responsible for the material's repulsion of water whilst the polar carboxylic acid -COOH or -OH group has sufficient affinity for water to anchor the molecule in the aqueous sub phase [Petty 1996]. That means, the carboxylic acid groups (head groups) of stearic acid are immersed in water surface whilst the long alkyl chain groups (tail groups) remain outside. As a result, the floating monolayer on the water surface displays unique orientation behaviour and tends to orient with the polar head groups in contact with water and tail groups aligning approximately orthogonally to the plane of water surface.

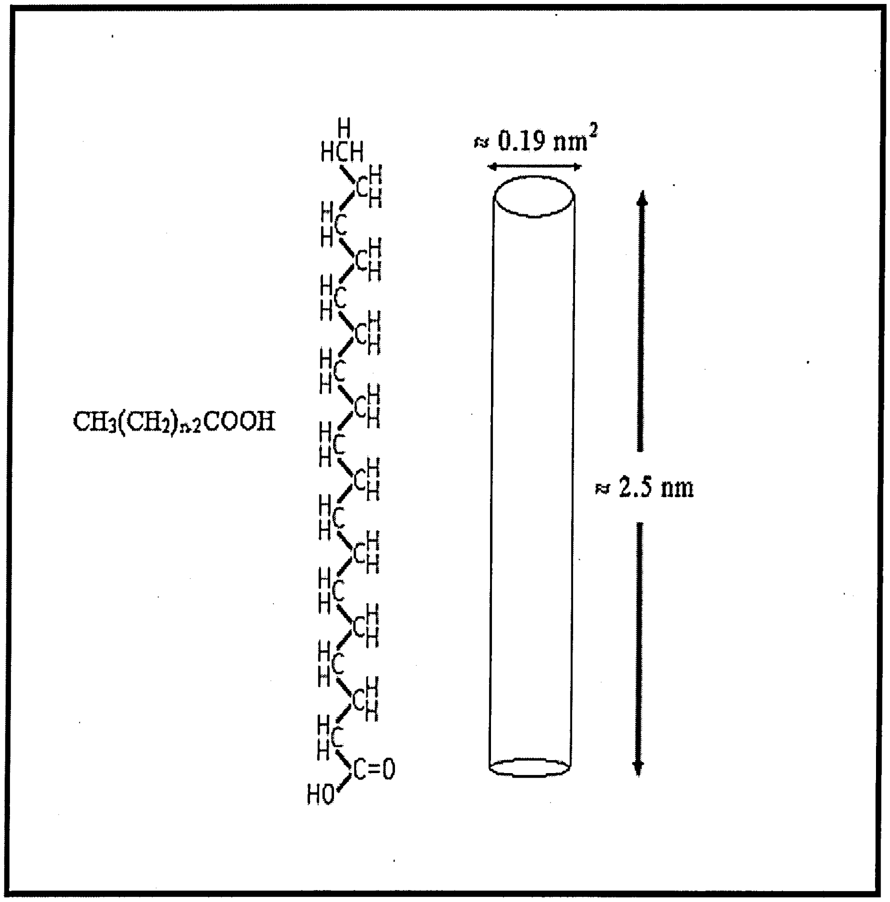

Figure 2.1. Molecular structure of stearic acid (n-octadecanoic) with n=18. The approximate geometrical shape and dimensions of the molecule are shown on the right. (after [Petty 1996]).

Hydrophilic molecules have either charged or polar end groups which interact with water, whilst hydrophobic non-polar molecules repel water. As a result, monolayer deposition depends strongly on the substrate nature due to different wetting angle. The technique for the fabrication of LB metal-stearic acid films begins with spreading a solution of a straight-chain stearic acid, $[CH_3(CH_2)_{n-2}COOH](C_n, n=18)$, onto a subphase of ultra pure water containing divalent metal ions. On pure water stearic acids form free acid LB films [Eliot 1999]. The chemical reaction of the cadmium ions and stearic acid is given by Equation 2.1 and their proton exchanges can be represented as shown in Figure 2.2.

$$Cd^{2+}(Cl^{-})_2 + 2HOOC(CH_2)_nCH_3 \rightarrow Cd^{2+}({}^{-}OOC(CH_2)_nCH_3)_2 + 2HCl \qquad (2.1)$$

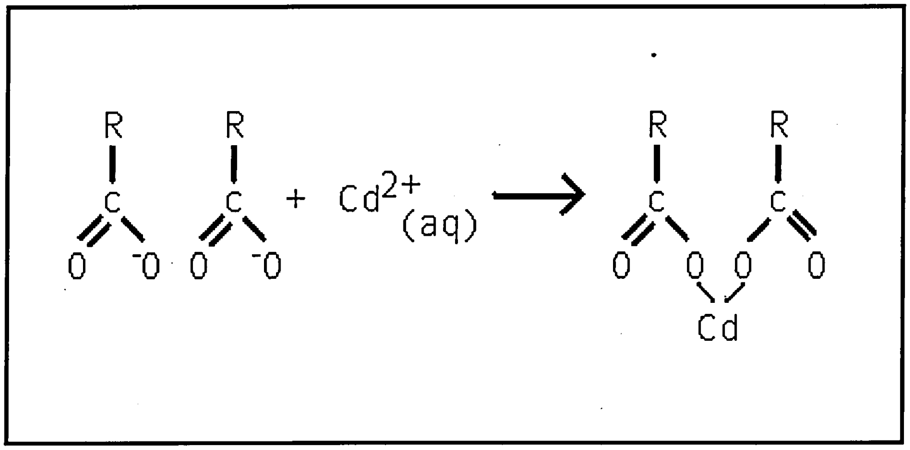

Figure 2.2. Reaction of Cd^{2+} with an alkanoic acid group.

2.1.2 Surface Pressure-Area Isotherms

The surface pressure isotherm is an important graph in the investigation of the characteristic surface behaviour of the LB material on the water surface and also to estimate the suitable pressure for the stability of a monolayer [Capan 1998]. The surface pressure is monitored continuously and the pressure-area isotherm $(\Pi - A)$ graph is plotted by a computer. Figure 2.3 shows an ideal $\Pi - A$ isotherm graph for stearic acid. Three distinct regions can be seen from the graph, 'gas', 'liquid', and 'solid' phases.

When the surfactants are spread onto the water surface, the molecules will occupy a large area per molecule and this region is known as the "gas" region. Upon compression of the monolayer that is by moving the barrier very slowly forward the confinement area is reduced, the molecules are forced closer together. The area per molecule decreases and at a certain point the surface pressure starts to increase which indicates low compressibility in the monolayers, the monolayers are said to be in the "liquid" region. When the barrier is closed even further, at one point, there will be a sharp increases of the slope with a small change in area per molecule of the Π-A isotherm. This is called the "condensed" or "solid" region of the isotherm, in which the molecules are arranged in a closely-packed and well-ordered structure, which reflects the presence of strong chain-chain interactions between the molecules. In this range of pressure it is possible to deposit LB films with uniform molecular thickness. By extrapolation of the graph, the area/molecule is found to be approximately 21Å^2 for stearic acid [Martin and Szablewski 1999].

If the barrier is closed much further, the pressure will increases and the film will be liable to collapse at critical pressure Π_C. In this case the monolayer order is destroyed. It is crucial that the surface pressure of the monolayer should be maintained at a constant fixed value in solid phase throughout the deposition process. A constant pressure is achieved by means of an electronic feedback mechanism which enables the area available to the film to be reduced until the preset pressure is regained [Petty et al. 1995]. Film transfer is characterized by measurements of the deposition ratio, τ, known as transfer ratio. This is the decrease in the area occupied by the monolayer on the water surface (A_L) divided by the coated area of the solid substrate (A_S), i.e.,

$$\tau = \frac{A_L}{A_S} \tag{2.2}$$

Ideally, a transfer ratio of unity would always be obtained, but in practice values between 0.9 and 1.0 are achieved for fatty acid [Richardson 1995].

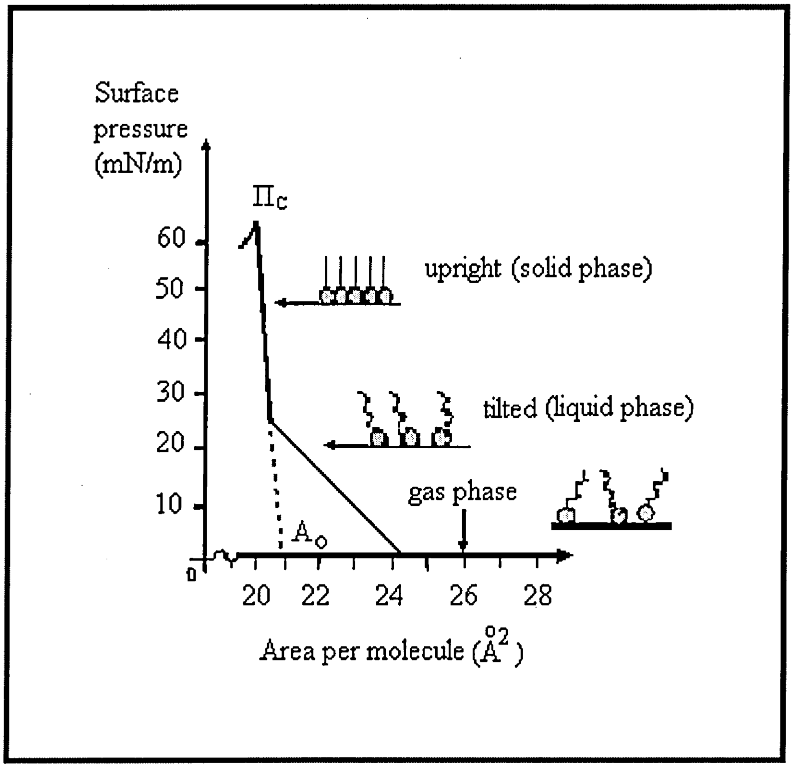

Figure 2.3. Surface pressure versus area per molecule for stearic acid.

2.1.3 Film deposition

LB films can be deposited onto a solid substrate by moving the substrate downwards and upwards through the sub phase surface by vertical lift. Several types of solid substrates are suitable for LB films. Glass slides are the most popular choice because of their availability and films deposited on them can subsequently be examined optically. For a wider transparency window, fused silica or quartz are the best candidates [Kajzar et al. 1988]. Silicon wafers are also used as a substrate due to their extremely smooth surface [Peterson 1990]. In order to measure the electrical characteristics of the film, a metal contact is required. The most widely used metals are Aluminium [Mann and Kuhn 1971; Tredgold et al. 1986] and gold [Mann and Kuhn 1971; Samokhvalov et al. 2002].

Substrates can be divided into two categories; hydrophilic and hydrophobic. Deposition onto a hydrophilic substrate (e.g. Al coated glass slide) only begins on the upward motion of the substrate whilst transferring a monolayer onto a hydrophobic surface (e.g. silicon wafer) begins on the downward motion. Figure 2.4 shows the upward and downward motion of the hydrophilic and hydrophobic substrates respectively.

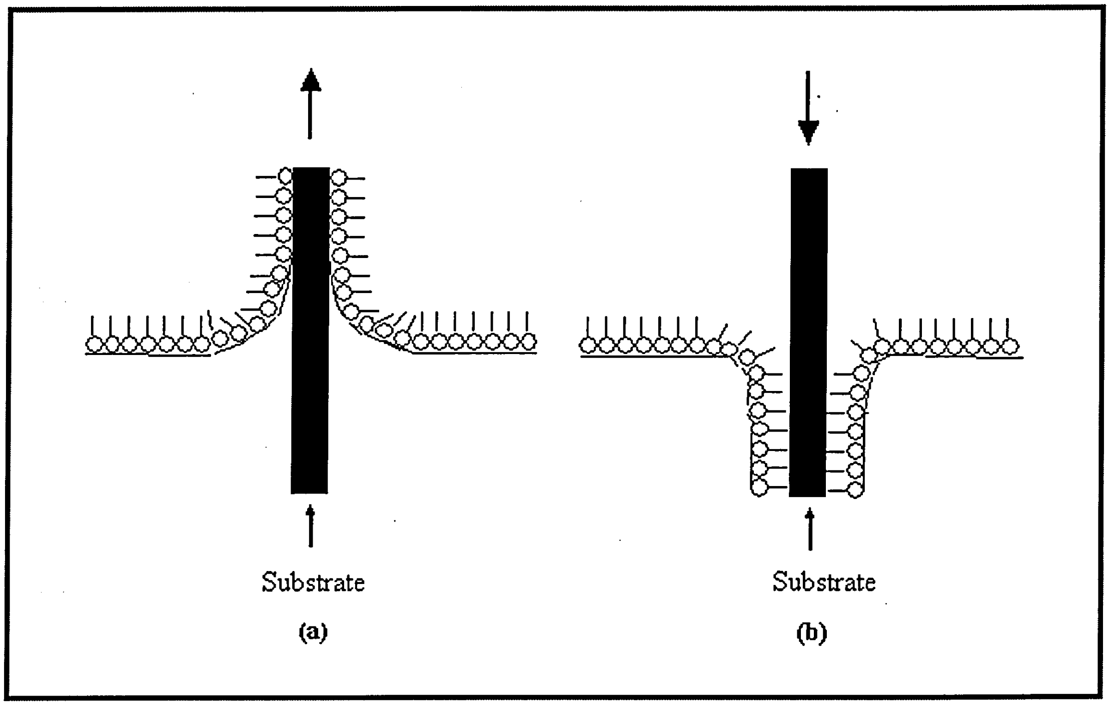

Figure 2.4. Deposition of first monolayer onto; (a) hydrophilic substrate (upward); (b) hydrophobic substrate (downward)

Floating monomolecular layers can be transferred onto solid substrates in a number of different ways depending on the dipping schemes which results in predominantly three types of LB films, namely as either X, Y, or Z types. Films may be picked up on immersion from air into the water only, known as X-type, or on passing from air into water and vice versa, Y-type deposition, or only on passing from water to air, Z type. Sometimes when two different monolayers were used, the resulting film is known as alternate layer type. Figure 2.5 shows all possible types of LB films. In LB deposition technique, the success of the first layer is very important since it will effect the following layers due to the fact that LB films are highly dependent on the surface of the first layer [Capan 1998].

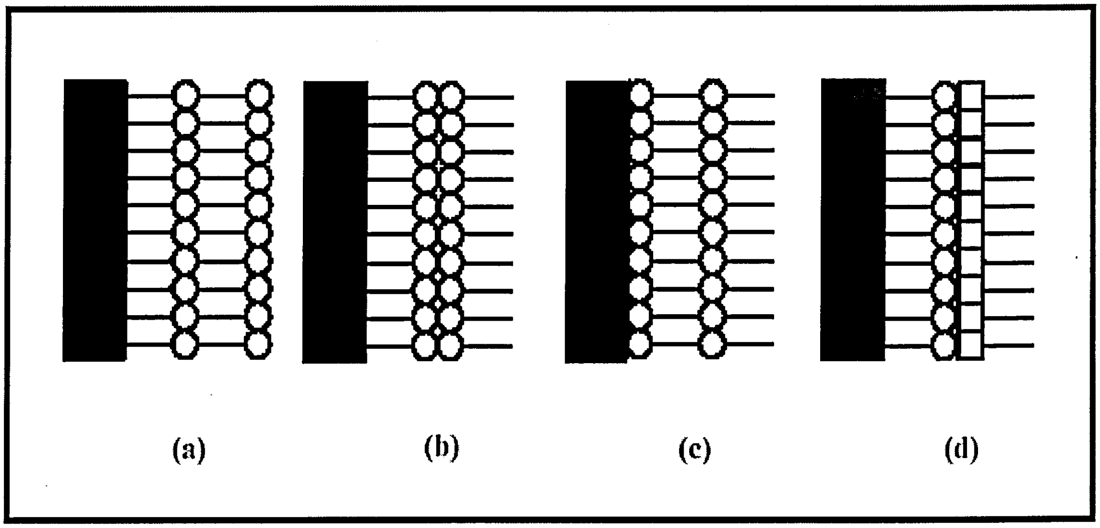

Figure 2.5. Deposition types of LB films (a) X-type (b) Y-type (c) Z-type
(d) Alternate Y-type

The most common type of LB film is Y-type, a centro-symmetric type. In Y type deposition, the hydrophobic tails of the stearic acid are attracted to the hydrophobic substrate, such as silicon wafer, on the downward pass. When the substrate with the first monolayer is subsequently raised, the hydrophilic head groups are attracted and thus a second monolayer is applied. The structural configuration of Y-type LB films is the head-to-head and tail-to-tail (HHTT) as shown in Figure 2.6 for hydrophobic substrate. For hydrophilic substrates the film formation will be in reverse order, tail-to-tail and head-to-head (TTHH). The LB films of stearic acid consist of regions of hydrocarbon chains, where van der Waals interactions predominate, and regions where the head groups (COO- and COOH) interact through dipole-dipole or H-bonding which is stable.

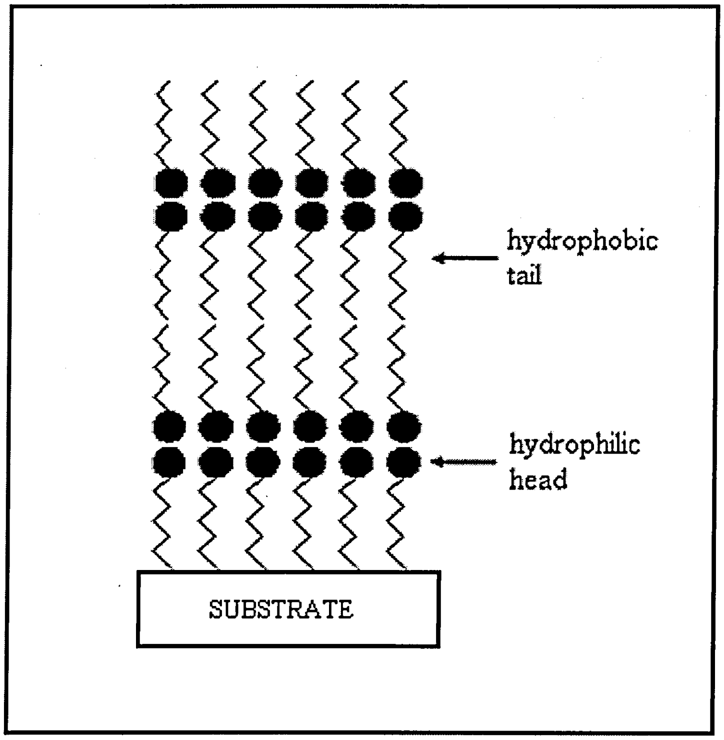

Figure 2.6. Y- type deposition onto hydrophobic substrate (e.g. silicon wafer)

However, by incorporating metal ions e.g. divalent cations such as Cd^{2+}, Ca^{2+}, Pb^{2+} into the head group regions of these types of films, the stability of the monolayer of stearic acid films could be increased by the addition of ion-dipole interactions. This is due to the cross linking action of the metal ions and triply charged cations tend to give extremely rigid monolayer with a high shear modulus [Roberts et al. 1990]. The exact degree of cations uptake depends on the pH of the sub phase as well as the stability of the aqueous ion. Metal ions can introduce special semiconducting, magnetic or quantum physical properties to the LB films [Werkman 1998; Swalen et al. 1987]

2.1.4 Applications of LB films

The Langmuir-Blodgett technique enables homogeneous ultra-thin organic films to be deposited onto solid substrates. It is one of the deposition techniques which allows manipulation of materials at the molecular level, i.e. molecular engineering [Petty, 1991]. Therefore there are many possible applications of LB films in various fields of science and engineering.

The modern era of research in LB films was started in 1970's, which coincided with the microelectronics revolution era. A considerable amount of work in LB film has begun to emerge. The earliest motivation arose from the fundamental work of Kuhn and colleagues on energy transfer in multilayer systems. They have successfully studied the possibility of utilising monolayers to construct precise super molecular structures. One of their findings which appears to be the first specific research towards functional systems on a molecular scale was the process of energy transfer between LB films composed of fatty acid salts and long-chain substituted dye molecules, that is between two different molecular species. Mann and Kuhn demonstrated for the first time the electron tunnelling through the barrier as the current transport mechanism in monolayer LB film of fatty acid salts of difference chain lengths (n=18 to 22) [Mann and Kuhn 1971]. They found the exponential decrease of conductivity as a function of film thickness which is predicted by the current tunnelling theory. These results have stimulated more investigations in electrical measurements by other researchers.

Polymeropolous (1977) reported the electron tunnelling through fatty-acid monolayers (n=16,18 and 20) in metal-LB film-metal (MIM) structure with different types of metal for top electrode. Later several other workers; Roberts et al. (1978), Ginnai et al. (1980) have reported the same behaviour. They found an empirical law of current-voltage characteristic of the form $I \alpha V^{1/4}$. The same occurrence was reported by [Tredgold and Winter 1981] in monolayer LB films of stearic acid. However, based on their current-temperature and current-time measurements, they concluded that the tunnelling current was not through the organic layer but via defects in it. Tredgold et al. found that the defect current could be reduced significantly by annealing the films after metal deposition process had been completed [Tredgold et al. 1984].

In the case of a thicker film, which goes beyond the tunnelling distance, Nathoo and Jonscher (1971) were the first researchers to reported their findings. Based on their results in dc and ac measurements, they suggested hopping conduction as the possible mechanism. Later Sugi et al. (1974;1975) and Iizima et al. (1976) investigated the conduction mechanism in Cd^{2+} salt films and found that the conduction in multilayer systems takes place according to a hopping mechanism associated with interface states. Figure 2.7 shows schematically the hopping model as proposed by [Sugi 1985]. Under an electrical field, an electron moves about the system, sometimes along an interface between the adjacent monolayer, sometimes transversing the hydrocarbon barrier, and drifts towards the positive electrode.

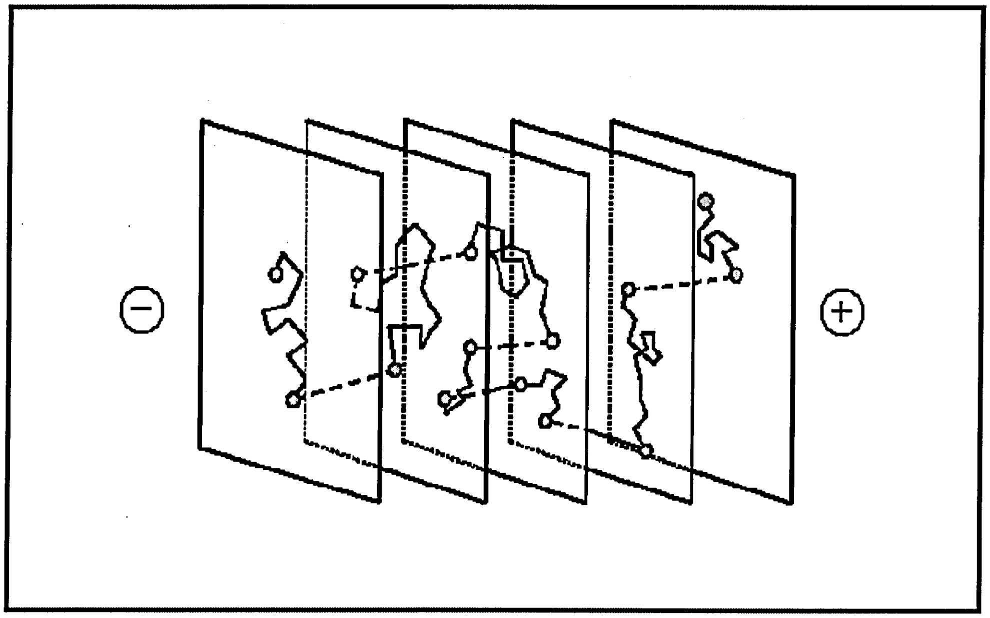

Figure 2.7. Hopping process in the multilayer system. An electron moves about the system, sometimes along the interface, sometimes transversing the hydrocarbon barrier, to drift stochastically towards the positive electrode [after Sugi 1985].

The assumptions involved are that each monolayer is associated with localized electronic states at both surfaces and that the current transport is via thermally assisted tunnelling between these states through the hydrocarbon barrier.

Nowadays nanoparticulate materials of semiconductors, metals and group II-VI semiconductors are the focus of intense research due to their novel electrical and optical properties. The LB technique plays a substantial role in contributing to the study of inorganic nanoparticles embedded in an organic matrix. Smotkin et al. (1988) reported the formation of inorganic nanometer-size semiconductor particles by exposing the fatty acid salt LB films to gaseous H_2S atmosphere. They observed a blue-shift in the absorbance spectrum by 0.38 eV with respect to bulk CdS which proved the existence of CdS nanoparticles embedded inside the fatty acid matrix. They also reported an increase in the film thickness of about $3\,\mathring{A}$ per layer. Since then, CdS and other II-VI compound semiconductor nanoparticles, such as HgS [Zylberajch et al. 1988], ZnS [Huang et al. 1997], CdSe [Grieser et al. 1992; Vossmeyer et al. 1994], and CdTe [Grieser et al. 1992; Zhavnerko et al. 1999] have been formed by the same method (by H_2S, H_2Se or H_2Te gaseous). Also, semiconductor nanoparticulates such as PbS [Erokhin et al. 1991], have been formed by the same technique.

Their structure has been characterized by several techniques such as UV-visible optical absorbance [Smotkhin et al. 1988; Facci et al. 1994; Dhanabalan et al. 1996; Mayya et al. 1998; Nabok et al. 2002], X-ray diffraction (XRD) [Erokhin et al. 1991], optical ellipsometry [Nabok et al. 1998] and X-ray photoelectron spectroscopy (XPS) [Elliot et al. 1999]. Characterisation of CdS nanoparticles by atomic force microscopy (AFM) was reported by several groups [Yang et al. 1998; Hanhong Li et al. 2000; Nabok et al. 1999].

They observed an increased in film roughness after being exposed to H_2S gas. Apart from single type nanoparticles there has also been research to investigate the formation of dual types nanoparticles in the LB films matrix. Elliot et al. (1999) have reported the formation of CdS and HgS nanoparticles in the LB films of behenic acid by using UV-visible and XPS.

Surface morphologies and optical properties of the LB films incorporating nanoparticles were studied by a large number of researchers. Unfortunately work in investigating the current transport mechanism is still lacking. One of the pioneering works to investigate the electron transport in such films was performed by Erokhin et al. in 1995. By using scanning tunnelling microscopy to form two tunnelling junctions, they observed the mono-electron phenomena in the behaviour of the I-V characteristics of single CdS particle formed in LB films of cadmium arachidate at room temperature [Erokhin et al. 1995]. In contrast there are several works on d.c. electrical characterization of films containing CdS nanoparticles prepared by different techniques. For example, Gupta et al. (1995) have reported variable range hopping within the Coulomb gap, quantum mechanical tunnelling and thermionic emission as the electron transport mechanisms in their nanostructured CdS films deposited by high-pressure magnetron sputtering.

Abdulkhadar and Thomas (1998) have studied the dc conductivity of CdS and ZnS nanoparticles prepared by chemical method and reported an increase in conductivity compared to that of bulk cystals. However no report on the conduction mechanism involved was mentioned. Liang et al. (2001) have reported the electroluminescence at room temperature of CdS nanoparticles prepared by spin coating technique on Si wafer. Again the conduction mechanism involved was not revealed but only mentioned that electroluminescence was due to quantum tunnelling of carriers into the nanoparticles.

2.2 Metal-Insulator-Semiconductor (MIS) Capacitor

The metal-insulator-semiconductor (MIS) capacitor is the most useful device in the study of semiconductor surfaces. Since the reliability and stability of all semiconductor devices are intimately related to their surface conditions, an understanding of the surface physics with the help of MIS capacitors is of a great importance to device operations [Sze 1981]. The MIS capacitor consists of insulating thin films (dielectric materials) sandwiched between metal and a semiconductor as illustrated in Figure 2.8. Insulators are essentially like semiconductors except that their bandgaps are larger so that there are negligible electrons or holes available for conduction. The Fermi level lies close to mid-bandgap. The resisitivity of these materials, as well as the breakdown fields, are extremely high [Singh 2001]. From the electrical point of view, the MIS (or MOS) structure with a metallic top electrode, also referred to as a gate, can be regarded as two plate capacitors mounted in series. The insulator capacitance C_i depends on the insulator permittivity ε_i and thickness d_i. The semiconductor capacitance $C_S(\psi_S)$ is field dependent, varies as

$$C_S(\psi_S) = -\frac{dQ_S}{d\psi_S} \tag{2.3}$$

where ψ_S is the time-dependent band bending established by the applied gate voltage V_g, and Q_S is the semiconductor charge induced by V_g. The total gate-to channel capacitance C can therefore be written as:

$$\frac{1}{C} = \frac{1}{C_S(\psi_S)} + \frac{1}{C_i} \tag{2.4}$$

Equation 2.4 expresses the total capacitance of the MOS capacitor as the series combination of the silicon capacitance and the oxide capacitance.

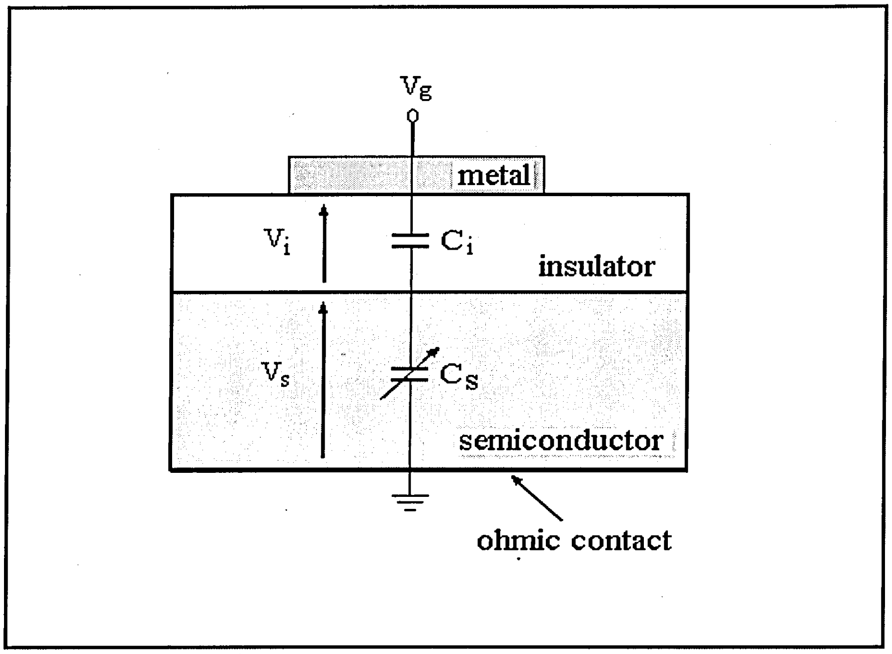

Figure 2.8. An ideal metal-insulator-semiconductor capacitor showing a simple equivalent circuit. The capacitor labeled C_S is shown variable to denote its bias dependence.

2.2.1 The ideal MIS equivalent circuit and energy-band diagram

The surface effects that arise in an apparently simple MIS structure are quite complicated. Normally the study of the MIS capacitor begins by assuming the capacitor is ideal, and later include effects encountered in real surfaces. The ideal MIS capacitor theory is very important and serves as a foundation for understanding practical MIS structures and for the exploration of the physics of semiconductor surfaces.

An ideal MIS capacitor is defined as follows [Sze 1981]:

(i) At zero applied bias, the energy difference between the metal work function ϕ_m and the semiconductor work function ϕ_S is zero $(\phi_m = \phi_S)$ or the band is flat.

(ii) The only charges that can exist in the structure under any biasing conditions are those in the semiconductor and those with equal but opposite sign on the metal surface adjacent to the insulator.

(iii) There is no carrier transport through the insulator under dc biasing conditions, or the resisitivity of the insulator is infinity.

The work function characteristic of the metal (or semiconductor) can be defined as the energy required to move an electron from the Fermi level to outside of the metal (or semiconductor) that is the vacuum level [Streetman and Banerjee 2000]. In MIS or MOS structure, it is more convenient to use a modified work function $q\phi_m$ for the metal-insulator interface (not the vacuum level). The energy $q\phi_m$ is measured from the metal Fermi level to the conduction band of the insulator. Similarly, $q\phi_S$ is the modified work function at the semiconductor-insulator interface.

The energy band-diagram of an ideal n-type MIS capacitor at equilibrium condition or flat band is shown in Figure 2.9. The term χ is the electron affinity, E_g the bandgap, ϕ_b the potential barrier between the metal and the insulator, and ψ_B the potential difference between the Fermi level E_F and the intrinsic Fermi level E_i of the bulk semiconductor. The energy bands are flat due to the fact that the device is at thermal equillibrium and the applied gate (V_G) voltage is equal to flatband voltage (V_{FB}) i.e. $V_G = V_{FB} = \phi_{MS}$. The term flat band refers to the fact that the energy band diagram of the semiconductor is flat, which implies that no un-neutralised charge exists in the semiconductor. The work function of a semiconductor, ϕ_S, varies with the doping type as well as with the doping concentration. ϕ_S equals the sum of the electron affinity in the semiconductor, χ, the difference between the conduction band energy and the intrinsic energy divided by the electronic charge in addition to the bulk potential. The equation for the flat-band condition for n-type semiconductor is given by [Sze 1981]

$$\phi_{ms} \equiv \phi_m - \phi_S = \phi_m - \left(\chi + \frac{E_g}{2q} - \psi_B \right) = 0 \tag{2.5}$$

The potential difference between the Fermi level E_F and the intrinsic Fermi level E_i is a function of doping concentration (N_D) and can be determined by

$$\psi_B = -\frac{kT}{q} ln\left(\frac{N_D}{n_i} \right) \tag{2.6}$$

where n_i is the intrinsic carriers concentration.

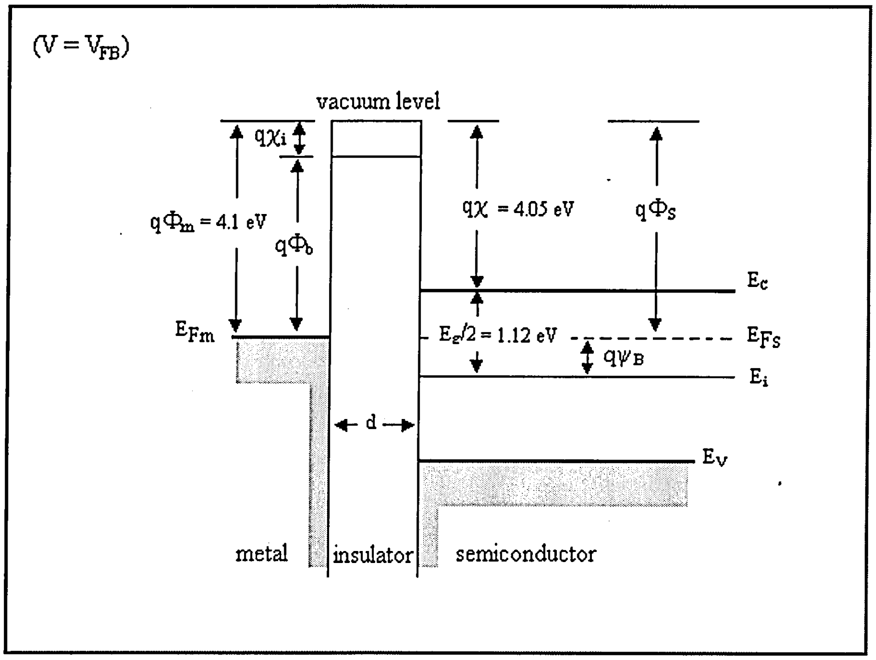

Figure 2.9. Flatband energy diagram of an ideal MIS structure consisting of aluminum metal/insulator/n-type silicon.

When an ideal MIS capacitor is biased, depending on the bias direction, either forward or reverse bias, there will be three different regimes of band bending existing at the semiconductor surface. When the top electrode is positively biased with respect to bottom contact (forward bias; $V_G > V_{FB}$), the bands bend downward and closer to the

Fermi level (Figure 2.10a). For an ideal MIS capacitor, no current flows in the structure, so the Fermi level remains constant in the semiconductor.

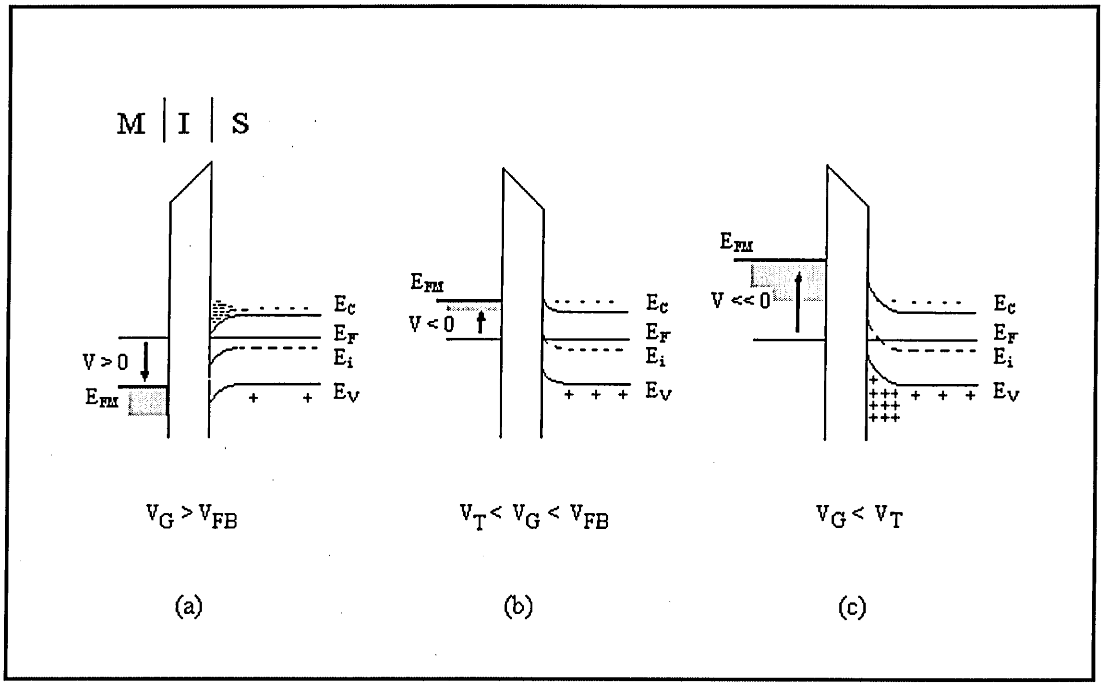

Figure 2.10. Illustration of the energy-band diagrams of a metal-insulator-semiconductor capacitor in several regimes. (a) accumulation (b) depletion and (c) inversion. E_C and E_V are the energy values at the conduction and valence band edges respectively. E_{FS} and E_{FM} are the Fermi level in the metal and semiconductor respectively.

As can be seen from Figure 2.10(a), the Fermi level near the interface lies closer to the conduction band, indicating a larger electron concentration than that arising from the bulk semiconductor. Since the carrier density depends exponentially on the energy difference $(E_C - E_F)$, this band bending causes an accumulation of majority carriers (electrons) near the semiconductor interface. This is known as the "accumulation" region. Accumulation occurs when gate voltage is higher than the flatband voltage $(V_G > V_{FB})$. When a small negative voltage $(V < 0)$ is applied, this reduces the potential of the metal, increasing the metal Fermi level by qV relative to its equilibrium position. As a result, the bands bend upward, and the majority carriers (electrons) are depleted from the semiconductor surface. This is known as the "depletion" region (Figure 2.10(b)). The flat band voltage V_{FB} separating the accumulation and depletion regime. The depletion region occurs when the gate voltage is between the flat band voltage and threshold voltage (V_T) $(V_T < V_G < V_{FB})$. In the depleted region the electron concentration decreases, moving E_C further from E_F at the surface, and bending the bands up near the semiconductor surface. When a larger negative voltage is applied, the bands bend even more upward. A sufficiently large voltage can bend the intrinsic level E_i at the surface crosses over the Fermi level E_F. At this point the number of holes (minority carriers) at the interface is larger than that of the electrons, the insulator-semiconductor interface is thus inverted, as shown in Figure 2.10(c). This is known as the "inversion" region. Inversion occurs at voltages smaller than the threshold voltage $(V_G < V_T)$.

If the negative voltage is further increased, the bands at the semiconductor surface bend upward more strongly until a strong inversion occurs. This condition occurs when the surface potential ψ_S is twice the potential difference between the Fermi level E_F and the intrinsic Fermi level E_i given by [Sze 1981]

$$\psi_S(\mathrm{inv}) = 2\psi_B = 2\frac{kT}{q}\ln\frac{N_D}{n_i} \qquad (2.7)$$

Figure 2.11 illustrates the bending of the semiconductor bands at the onset of strong inversion. In the strong inversion regime, the surface has become a strong p-type material. Accordingly, the maximum width W_m of the surface depletion region under steady-state condition can be obtained by [Sze 1981]

$$W_m \approx \sqrt{\frac{2\varepsilon_S \psi_S(\mathrm{inv})}{qN_D}} = \sqrt{\frac{4\varepsilon_S kT\ln(N_D/n_i)}{q^2 N_D}} \qquad (2.8)$$

The charge per unit area in the depletion region at strong inversion is given by [Streetman and Banerjee 2000]

$$Q_d = qN_D W_m = 2\sqrt{\varepsilon_S q N_D \psi_B} \tag{2.9}$$

The corresponding applied voltage to create this depletion charge plus the surface potential $\psi_S(\text{inv})$ is called threshold voltage. The threshold voltage represents the minimum voltage required to achieve strong inversion. For ideal MIS capacitors it is given by

$$V_T = -\frac{Q_d}{C_i} + 2\psi_B \tag{2.10}$$

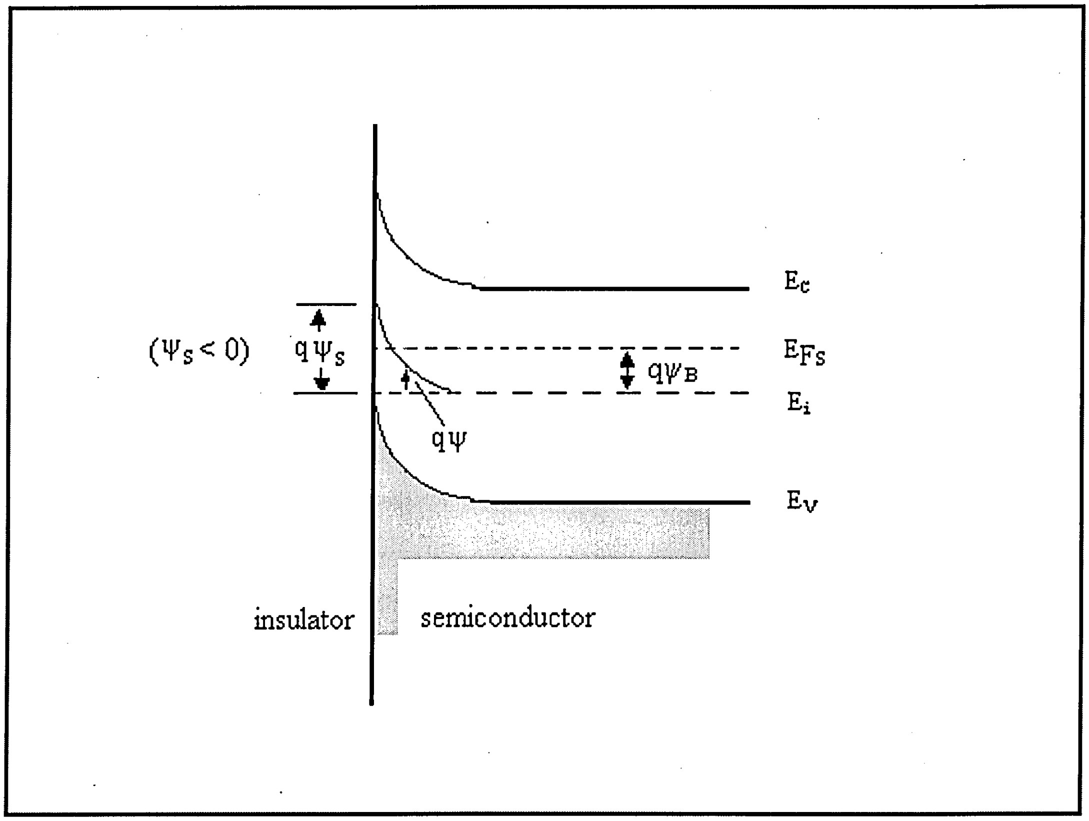

Figure 2.11. Energy-band diagram at the surface of a n-type semiconductor in the inversion region: At the onset of strong inversion the surface potential ψ_S is twice the value of ψ_B in the neutral n-type semiconductor.

This assumes the negative charge at the semiconductor surface Q_S at inversion is mostly due to the depletion charge Q_d. In real MIS capacitor, charges at the Si-insulator interface and within the insulator must be taken into account. The corresponding threshold voltage now is given by

$$V_T = \phi_{MS} - \frac{Q_i}{C_i} - \frac{Q_d}{C_i} + 2\psi_B \tag{2.11}$$

where $\phi_{MS} - \frac{Q_i}{C_i} = V_{FB}$ is the the flat-band voltage shift due to charges at the interface, $Q_i\ (C/m^2)$. It can be seen from Equation 2.11, the voltage required to create strong inversion must be large enough to first achieve the flat band condition (ϕ_{MS} and Q_i/C_i), then accomodate the charge in the depletion region (Q_d/C_i), and finally to introduce the inverted region $(2\psi_B)$. This equation accounts for the dominant threshold voltage effects in typical MIS or MOS devices.

2.2.2 Capacitance-voltage of a leaky dielectric material

Capacitance versus voltage (C-V) measurement is an important technique to analyze the properties of metal-insulator-semiconductor (MIS) devices. For thin film insulator devices, (or for leaky insulator) however, accurate C-V data is difficult to obtain for two reasons [Chen et al. 2004];

(1) exponentially increasing direct tunnelling leakage current

(2) large film capacitance make even modest series resistance terms important.

An ideal capacitor without any parasitic resistance has an infinite quality factor Q or zero dissipation factor D, while an ideal resistor has an infinite D. The direct result of a large D is a roll-off of the C-V curve in the inversion or accumulation region.

A potential source of error in all C-V profiling methods arises due to the inability to measure directly the dielectric capacitance and the voltage across the dielectric. Instead, the measurements were made on the entire device. The commercial LCR meters model the device as either a parallel combination of a capacitor and a conductive element $(C_p - R_p)$ or a series combination of a capacitor and a resistor $(C_S - R_S)$. The most common method by which such measurements are evaluated is to assume that the impedance of those parts of the circuit in series with the true dielectric capacitance is negligibly small [Briggs and Stagg 1988]. Thus, the data may be interpreted on the basis of either a parallel or series equivalent circuit as shown respectively in Figure 2.12(a) and 2.12(b). A parallel resistance accounts for leakage current in the insulator layer, whilst series resistance accounts for contact and substrate resistance. In thicker oxide (or insulator) the leakage current is negligible and the parallel resistance can be omitted from the model, thus only series equivalent circuit is needed to model the capacitor.

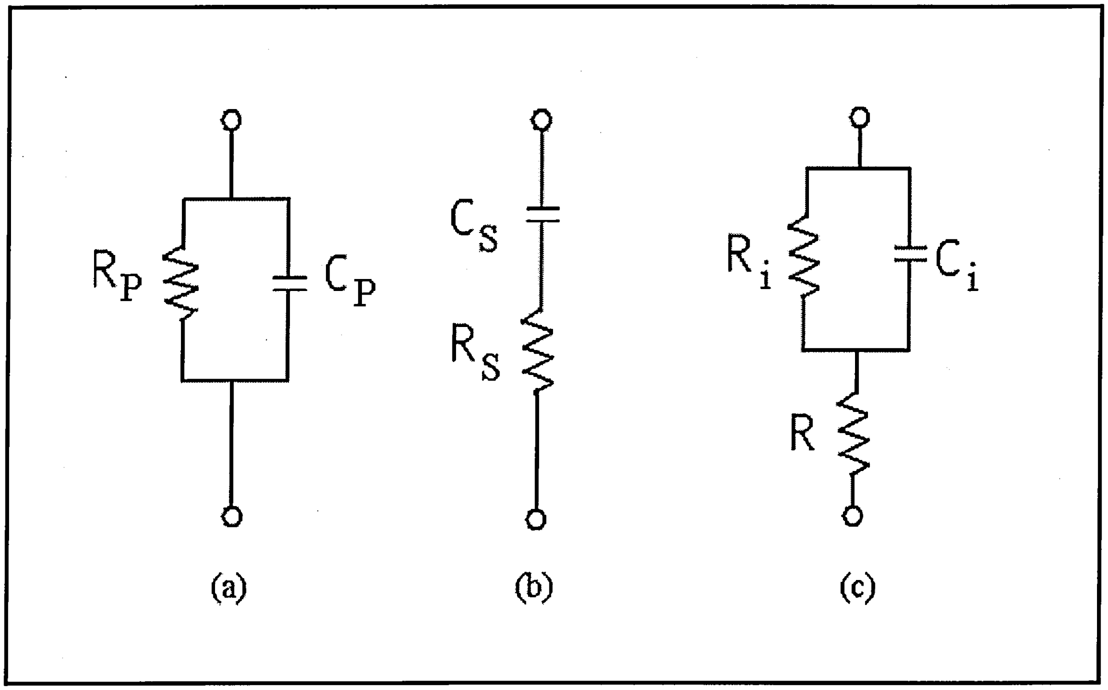

Figure 2.12 (a) Parallel configuration for small series resistance R, and (b) series configuration for low leakage current, both as modelled by commercial LCR meters. (c) The three-element circuit model of a real capacitor.

However, in leaky insulator or as the thickness of the oxide (insulator) is reduced, direct tunnelling leakage current will become a problem and quasi-static capacitance measurements becomes impossible. One technique to avoid this problem is by measuring the capacitance at a very high frequency so that the capacitive current is dominant. However, at very high frequency the series resistance (in the substrate and electrodes) becomes significant due to low impedance of the oxide capacitor. The C-V measurements of very thin oxides (or leaky insulator) with large leakage currents are often performed using parallel circuit model as shown in Figure 2.12(a), which neglects series resistance. However, this method is only accurate for capacitor with negligibly small series resistance (R). For a system with series resistance which cannot be neglected the results will not be accurate. Hence, series and shunt parasitic component of resistances must be dealt with simultaneously.

A technique which can overcome the above problem and can determine the acurate MOS (or MIS) oxide capacitance when the thickness of oxide is less than $2.5\,\mathrm{nm}$ was proposed by [Yang and Hu 1999]. It is also can be used in determining the true capacitance of a leaky insulator system.

2.2.3 Yang's model

Yang's method is normally known as a "three-element lumped circuit model" or a "two-frequency model" which takes into account the effects of the substrate, contact resistance as well as the parallel resistance across the capacitor. It is a mathematical model which takes into account all the three elements involved in the real MOS structure. The three-element circuit model of a MOS (or MIS) capacitor with leaky gate oxide (or insulator) is shown in Figure 2.12(c). C_i represents the actual frequency-independent device capacitance, R_i represents the effective device resistance due to leakage current (direct tunnelling) through the oxide/insulator, and R represents the series resistance of the substrate and the electrodes. Both resistances are voltage dependent. This model should reveal the accurate insulator capacitance in the accumulation region $(C = C_i)$ and in the strong inversion region with $1/C = 1/C_i + 1/C_{Dep}$ where C_{dep} is the depletion capacitance in the semiconductor. By using this technique, the true insulator capacitance can be determined from measurements made at two different frequencies.

The impedance of the three-element circuit model shown in Figure 2.12(c) is given by

$$
\begin{aligned}
Z &= \mathrm{Re}(Z) + j\,\mathrm{Im}(Z) \\
&= R + \frac{R_i(1 - j\omega R_i C_i)}{1 + \omega^2 R_i^2 C_i^2} = \frac{R + R_i + (\omega R_i C_i)^2 R}{1 + \omega^2 R_i^2 C_i^2} - j\frac{\omega R_i^2 C_i}{1 + \omega^2 R_i^2 C_i^2}
\end{aligned}
\tag{2.12}
$$

where $\omega = 2\pi f$, with f being the frequency of the AC stimulus.

The impedance of the parallel circuit model in Figure 2.12(a) is given by

$$
Z = \frac{R_m}{1 + \omega^2 R_m^2 C_m^2} - j\frac{\omega R_m^2 C_m}{1 + \omega^2 R_m^2 C_m^2} \tag{2.13}
$$

Equation 2.13 can also be written in term of dissipation factor D, as

$$
Z = \frac{D_m}{\omega C_m (1 + D_m^2)} - j\frac{1}{\omega C_m (1 + D_m^2)} \tag{2.14}
$$

where $D_m = \dfrac{1}{\omega R_m C_m}$ is the dissipation factor or dielectric loss (tan δ), and R_m and C_m refer to measured values. Equating the imaginary parts of the true impedance (Equation 2.12) and the measured impedance (Equation 2.14), one obtains

$$
\frac{1 + \omega^2 R_i^2 C_i^2}{\omega R_i^2 C_i} = \omega C_m \left(1 + D_m^2\right) \tag{2.15}
$$

Measuring the capacitance and dissipation at two different frequencies, substituting into Equation 2.15 for each frequency, subtracting, and solving for C_i, one obtains

$$C_i = \frac{f_1^2 C_{m1}(1+D_{m1}^2) - f_2^2 C_{m2}(1+D_{m2}^2)}{f_1^2 - f_2^2} \tag{2.16}$$

where C_{m1} and D_{m1} refer to the values measured at the frequency f_1 and C_{m2} and D_{m2} refer to the values measured at the frequency f_2. Proceeding in a similar manner with the real parts of the impedance, one obtains the relations for shunt (R_i) and parasitic series (R) resistances

$$R_i = \frac{1}{\sqrt{\omega^2 C_m C_i (1+D_m{}^2) - \omega^2 C_i{}^2}} \tag{2.17}$$

and

$$R = \frac{D_m}{\omega C_m (1+D_m{}^2)} - \frac{R_i}{1+\omega^2 R_i{}^2 C_i{}^2} \tag{2.18}$$

Many researchers have reported the usefulness of this technique to determine the equivalent oxide thickness (EOT) of MOS and MIS capacitors from the true capacitance value when the oxide thickness is reduced below 2.5nm, due to leakage current in their dielectric materials. Most of the researchers applied this technique to determine the equivalent oxide thickness (EOT) of ultra-thin SiO_2.

The International Technology Roadmap for Semiconductors predicts the approaching need for a sub-1.5nm gate oxide for a sub-0.1μm complementary metal-oxide-semiconductor (CMOS) technology [ITRS] which means that, the era of conventional SiO2 will soon end due to excessive quantum tunnelling leakage current. With respect to conventional SiO_2, Yang's technique also attracted reseachers in determining EOT of new materials with high-k materials such as Ta_2O_5, ZrO_2, HfO_2, TiO_2, and Al_2O_3 which have dielectric constant ranging from 10 to 80. These materials provide the required EOT without further reduction in the insulator physical thickness, which is the key issue to limit the gate leakage current and to maintain comparable MOSFET operation and reliability [Ghibaudo et al. 2000]. Among them, Zirconium silicate films have been widely studied due to their high thermal stability and good electrical properties.

Zhu and Liu have successfully used the model to extract the EOT of Zr-Al-O dielectric films deposited on Si substrates [Zhu and Liu 2003]. Ramanathan et al. [Ramantahan et al. 2002], and Chim et al. [Chim et al. 2003] have demonstrated the usefulness of Yang's model to determine the true capacitance value of a zirconium oxide (ZrO_2) thin film which was affected by frequency dispersion in the accumulation region due to leakage current. Recently, Zhu et al. (2005) have studied the Zirconium silicate films on Silicon and Platinum substrates and reported the use of Yang's technique in extracting the EOT.

Until now, Yang's model has been cited more than 100 times, as found in Web of Science portal [http://portalt.wok.mimas.ac.uk/portal.cgi]. The only limitation in Yang's model is that, the difference in impedance values at the two different frequencies must be large, only then the accurate capacitance value can be obtained. If however the different is not wide enough, the obtained parameters may be inaccurate [Agilent].

2.3 Leakage current in insulating films

High field electrical conduction in insulating materials is quiet complex because of the possibilities of several transport mechanisms involved [Lamb 1967], which make it difficult to distinguish them. These mechanisms are usually governed by a number of factors such as the work function of the electrodes and that of the sandwich insulating layer, applied field and structural defects [Nataraj et al. 1999]. In an ideal MIS (or

MIM) device the conductivity of the insulating film is assumed to be zero. However, in reality, insulators show carrier conduction when the applied electric field or temperature is sufficiently high [Sze 1981]. Under such circumstances, various conduction processes are possible. Due to organic (insulator) materials typically having a large band gap, the electronic conduction is hence likely assisted by the states inside the band gap. The energy levels inside the band gap can be regarded as defect states which are acting as potential trapping centers for current carriers. Several types of defects which are typical in organic thin films include [Lin 1990]:

(i) point-like defects (e.g. vacancy, interstitial-like)
(ii) extended defects (e.g. dislocation-like, grain boundaries, melt spots)
(iii) undesired impurities (e.g. foreign atoms)
(iv) surface states (on interfaces)
(v) disorder (e.g. localization)
(vi) free volume (e.g. structure fluctuation)
(vii) fluctuations.

If electrons are trapped mainly by defects on the metal-insulator interfaces then either Schottky or tunnelling conduction dominates. If electrons are mainly trapped by defects inside the insulating film, then space-charge-limited conduction dominates. Others like Ohmic and Poole-Frenkel conduction are directly related to defects. Ionic conduction can be considered as the drift of structural defects under the influence of an applied electric field. Several type of current conduction processes in insulators are summarised in Table 2.2 and the relation with the defects inside the insulating layers are given in Table 2.3.

Process	Expression	Voltage and Temperature Dependence
Schottky emission	$J = A^{*}T^{2}\exp\left[\frac{-q\left(\phi_B - \sqrt{qE/4\pi\varepsilon_i}\right)}{kT}\right]$	$\approx T^{2}\exp(\beta_S V^{1/2}/kTd^{1/2} - q\phi_B/kT)$
Poole-Frenkel effect	$J \approx E\exp\left[\frac{-q\left(\phi_B - \sqrt{qE/\pi\varepsilon_i}\right)}{kT}\right]$	$\approx V\exp(\beta_{PF}V^{1/2}/kTd^{1/2} - q\phi_B/kT)$
Tunnel or field emission (Fowler-Nordheim)	$J \approx E^{2}\exp\left[-\frac{4\sqrt{2m_o}(q\phi_B)^{3/2}}{3q\hbar E}\right]$	$\approx V^{2}\exp(-a/V)$
Space-charge-limited	$J = \frac{9\varepsilon_i \mu V^{2}}{8d^{3}}$	$\approx V^{2}\exp(-b/T)$
Ohmic	$J \approx E\exp(-\Delta E_{ae}/kT)$	$\approx V\exp(-c/T)$
Ionic conduction	$J \approx \frac{E}{T}\exp(-\Delta E_{ai}/kT)$	$\approx \frac{V}{T}\exp(-d/T)$

Table 2.2 Basic conduction processes in insulators (after [Sze 1981]).

note:

A^{*} is the effective Richardson constant, $\hbar = h/2\pi$ where h is the Planck's constant, ϕ_B = the barrier height, E = the electric field, ε_i = insulator dynamic permittivity, m_o = electron effective mass, d = insulator thickness, ΔE_{ae} = activation energy of ions, and $\beta_{PF} = 2\beta_S = \left(\frac{q^{3}}{\pi\varepsilon_0\varepsilon_r}\right)^{1/2}$. Positive constants independent of V and T are a, b, c and d.

Process	Description	Relation with defects
Schottky emission	Electrons emitted from the cathode jump (or thermally assisted) over the potential barrier at the interface	Surface states modification leads to lowering of barriers
Poole-Frenkel effect	At high field the trapped electrons are responsible for the conduction	Defect state control the conduction
Tunnelling or field emission	The electron from the cathode tunnel through the potential barrier without . thermal excitation (the position of the Fermi level is fixed)	The electron tunnel from defect to defect (the position of the Fermi level is varied)
Space-charge limited	Charged carriers are trapped by the deep level defects, and there are no free electrons in dielectric to balance these trapped charges	Trapped charges control the conduction
Ohmic	The electrons hop from one defect to another	Defect states (at the same energy levels) control the conduction
Ionic conduction	Conduction is controlled by the hopping or diffusion of the ions	Ion behave as charged defects.

Table 2.3. The brief relationship between defect model and basic conduction processes (after [Lin 1990]).

Several type of current conduction processes will be discussed in the following sub-sections.

2.3.1 Schottky emission

The current (or current density, J) flow through the semiconductor due to thermionic emission of majority carriers is given by the Richardson equation [Simmons 1970; Kasap 1997]:

$$I = A^{**}AT^2 \exp\left[-\frac{q\phi_b}{kT}\right] \quad \text{or} \quad J = A^{**}T^2 \exp\left[-\frac{q\phi_b}{kT}\right] \tag{2.19}$$

where A, q, k, T and ϕ_b are the device area, electron charge, Boltzmann's constant, temperature and barrier height respectively.

$$A^{**} = \frac{4\pi m^* q k^2}{h^3} \tag{2.20}$$

is the effective Richardson's constant which is equal to $1.12 \times 10^6 \ \mathrm{A\,m^{-2}\,K^{-2}}$ for n-type silicon [Rhoderick 1988] when the electron effective mass m^* is approximated to the electron mass. This current saturates if the barrier height is independent of the applied voltage, but due to the inclusion of image force effect (Schottky effect), the current varies with the applied voltage by the following relation:

$$J = A^* T^2 \exp\left[-\frac{q\phi_b}{kT}\right] \exp\left[\frac{\beta_S E^{1/2}}{kT}\right] \tag{2.21}$$

where

$$\beta_S = \left[\frac{q^3}{4\pi\varepsilon_r\varepsilon_o}\right]^{1/2} \tag{2.22}$$

known as Schottky barrier lowering coefficient. Equation 2.21 is known as Schottky emission where ϕ_b in Equation 2.19 is replaced by $\phi_b - \Delta\phi_S$. $\Delta\phi_S$ is the total lowering of the potential barrier height due to image force effect at a metal-semiconductor contact and is given by

$$\Delta\phi_S = \beta_S E^{1/2} \tag{2.23}$$

A plot of ln J versus $V^{1/2}$ (or $E^{1/2}$) should yield a straight line with the slope and intercept giving information regarding the Schottky barrier constant β_S and barrier height ϕ_b respectively. The effect of a Schottky barrier at a metal-semiconductor contact is to provide a rectifying contact, which means the current conducts more easily in one direction than in the other. Schottky emission processes have been reported at high fields $(>10^7 \ \mathrm{V/m})$ in LB films of fatty acids and their salts [Petty 1996].

2.3.2 Poole-Frenkel effect

The Poole-Frenkel effect is the lowering of the Coulombic potential barrier when it interacts with an electric field, i.e. when the electric field interacts with the coulombic potential barrier of a donor centre or trap, the height of the barrier is lowered. The field lowering of the potential barrier was first considered by Frenkel in insulators and semiconductors [Frenkel 1938]. The Poole-Frenkel effect is often observed in amorphous materials, usually dielectrics, due to the relatively large number of defect centres present in the energy gap [Harrell and Frey 1999]. This model is often used to explain electronic conduction in thin dielectric films, as well as in some semiconductor materials. Frenkel's original model (classical model) incorporates the Boltzmann approximation for the electron energy distribution, and assumes that the Fermi level is in the middle of the energy gap [Harrel and Gopalakhrisnan 2002].

A first-order model for the field induced barrier lowering, known as the PF effect, was developed by Frenkel in order to explain the increase in electrical conductivity at high fields observed in insulators and low-mobility semiconductors prior to electric breakdown [Frenkel 1938]. The material is considered to be a system of neutral atoms, and when an atom is ionized, the resulting free electron exists in a medium of neutral, polarisable atoms and the field of the fixed positive ion. Frenkel's model thus considers this potential energy field as a barrier in which the electron is trapped. For the electron to be emitted from the trap, and thus be available for conduction, it must gain sufficient energy to surmount the peak of the potential energy barrier.

According to Frenkel's classical model, electron emission is primarily controlled by the electric field (E), which effectively reduces the barrier height on one side of the trap. As a result, the probability of the electron escaping from the trap will increase. Figure 2.13

illustrates this process where a Coulombic potential well is shown in the presence of an electric field. The term $q\phi$, defined as the ionization potential (in eV), is the energy required for the trapped electron to escape the influence of the positive nucleus of the trapping centre in the absence of an electric field. $\beta\sqrt{E}$ is a measure of the reduction in trap barrier height due to the applied electric field. When the applied electric field is increased, the potential barrier is reduced as shown in Figure 2.13. This will make it easier for the electron to vacate the trap by thermal emission and enter the conduction band (or quasi-conduction band) of the host material. The term quasi-conduction band is only used when discussing amorphous solids, which have no real band structure [Harrel and Gopalakhrisnan 2002]. According to Frenkel's classical model, the reduction in barrier height by the applied electric field, is given by

$$\Delta q\phi = \beta\sqrt{E} \tag{2.24}$$

where β is the Poole-Frenkel field lowering coefficient which depend on material dielectric constant, given by

$$\beta = \sqrt{\frac{q^3}{\pi\varepsilon_o\varepsilon_r}} = 2\beta_S \tag{2.25}$$

where ε_o and ε_r are the free-space permittivity and the relative dielectric constant respectively.

The effective ionization potential, $q\phi_{eff}$, of the Coulombic trap in an applied electric field can be written as:

$$q\phi_{eff} = q\phi - \beta\sqrt{E} \tag{2.26}$$

The ionization potential, $q\phi$, in Equation 2.26 is a constant reference potential when no electric field is applied, whilst $q\phi_{eff}$ is the reduction in barrier height relative to this reference due to electric field.

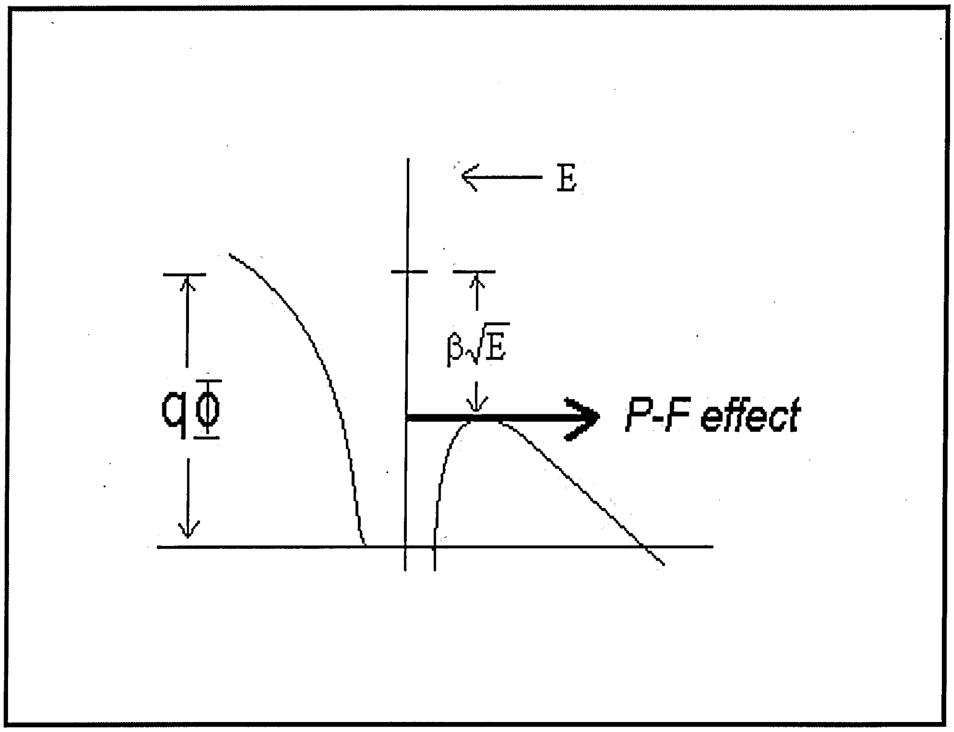

Figure 2.13. Coulombic potential well in the presence of an electric field illustrating the Poole-Frenkel effect [after Harrel and Frey 1999].

The classical model for current density is based on several assumptions [Harrel and Frey 1999]. Conductivity, σ, is approximated to be proportional to the free carrier concentration in the quasi-conduction band, and the Fermi level is assumed to be midway between the ground state of the trap and the quasi-conduction band of the host material. Furthermore, the Boltzmann approximation is used for the electron energy distribution. Using this assumption, along with Equation 2.25 for the field-induced barrier lowering, the conductivity, σ, can be written as [Harrel and Frey 1999]:

$$\sigma = \sigma_o \exp\left[-\frac{q\phi - \beta\sqrt{E}}{\xi kT}\right] \tag{2.27}$$

and thus the current density is given by:

$$J = \sigma_o E \exp\left[\frac{\beta\sqrt{E} - q\phi}{\xi kT}\right] \tag{2.28}$$

where ξ is the slope parameter between 1 and 2. σ_o is the saturation in conductivity which only occurs when all of the traps have been ionized i.e. $q\phi = \beta\sqrt{E_S}$ where E_S is the electric field at saturation. When this condition happens, the concept of a trap has no meaning and the model is no more valid. An expression for the density of electrons in the conduction band due to the PF effect was first presented by [Pillonnet and Ongaro 1989 ; Harrel and Gopalakhrisnan 2002].

Equation 2.24 to 2.28 constitutes Frenkel's classical model for field-assisted thermal ionization of electrons from Coulombic traps, later known as the Poole-Frenkel effect. This model assumed that each Coulombic centre is independent of each other which means the potentials do not overlap. Equation 2.27 (and 2.28) was derived under the assumption of a 'midgap' Fermi level, and ξ is taken to equal 2 ($\xi = 2$). These equations are applied to a material with donor traps only, no acceptor traps [Harrel and Gopalakhrisnan 2002]. When the acceptor concentration is high enough that the Fermi level is lowered to the donor trap level, ξ will have a value of 1 [O'Dwyer 1973]. Equation 2.28 will becomes

$$J = \sigma_o E \exp\left[\frac{\beta\sqrt{E} - q\phi}{kT}\right] \tag{2.29}$$

The plot of $\ln(J/E)$ versus $\sqrt{E}$ will yield a straight line given by

$$\ln\left(\frac{J}{E}\right) = \frac{\beta}{kT}\sqrt{E} + \left[\ln\sigma_o - \frac{q\phi}{kT}\right] \tag{2.30}$$

The slope of the PF plot, m, is proportional to β, and is given as

$$m = \frac{\beta}{kT} \tag{2.31}$$

Since $E = V/d$ where V is the applied voltage and d is the film thickness, Equation 2.29 can also be written in a traditional current density-voltage (J-V) terms as [Gould and Ismail 1998]

$$J = J_o \exp\left[\frac{\beta_{PF} V^{1/2}}{kTd^{1/2}}\right] \tag{2.32}$$

where $J_o = \sigma_o E$ is the low field current density. The term $\beta\sqrt{E}$ is dominant in the PF effect whilst the term $q\phi$ can be neglected. This simplification equation still yields the same value of β_{PF} from the slope of the PF plot as in the classical model (equation 2.30). From Equation 2.32 the plot of ln J versus $V^{1/2}$ will give a linear equation as

$$\ln J = \ln J_o + \frac{\beta_{PF} V^{1/2}}{kTd^{1/2}} \tag{2.33}$$

where the slope m of the plot is given by

$$m = \frac{\beta_{PF}}{kTd^{1/2}} \tag{2.34}$$

The linear sections of the curve may be interpreted in terms of either Schottky effect or the Poole-Frenkel effect. The difference between them is the Schottky effect is the field lowering of the interfacial barrier at the injecting electrode interface whilst the Poole-Frenkel effect is the field-enhanced thermal excitation from impurity centres.

The Poole-Frenkel (PF) effect has been observed in many dielectric materials by many researchers. Gould et al. have reported the PF conduction mechanism in CdTe thin films doped with $PbCl_2$ [Gould and Ismail 1998], Au-SiO_x-Au [Gould and Lopez 1999], and Al-SiN_3N_4-Al structures [Awan et al. 1999]. Sharpe and Palmer (1996) have reported the PF effect at low voltage bias in Cu-SiO_x-Cu devices. Werner et al. have observed the field-induced lowering of trap depth in organic dye;- tris-8-(hydroxyquinoline) aluminium (Alq_3) and explained it in the framework of the PF effect [Werner et al.

2001]. Poole-Frenkel emission process has also been reported at high fields ($>10^7\ \mathrm{V/m}$) in LB films of fatty acids and their salts [Petty 1996].

2.3.3 Fowler-Nordheim tunnelling

Basically there are two types of tunnelling mechanisms involved in metal-insulator-metal (MIM) or metal-insulator-semiconductor (MIS or MOS) structures, direct tunnelling and Fowler-Nordheim field emission. If the insulating layer is relatively defect free and extremely thin, normally less than 5nm, electrons can tunnel from metal to metal or to semiconductor conduction bands due to quantum mechanical tunnelling (direct tunnelling). For oxide layer larger than 5nm, electron cannot tunnel directly through the oxide. It requires high applied voltage to make the effective distance small, then only electrons can tunnel. For insulator layer greater than 5nm, electrons tunnel from silicon conduction band to SiO_2 (insulator) conduction band. The energy-band diagram of a MOS capacitor due to Fowler-Nordheim tunnelling and direct tunnelling are illustrated in Figure 2.14.

The Fowler-Nordheim conduction is related to the tunnel emission of trapped electrons towards the conduction band [Hajji 1999]. Lenzlinger and Snow (1969) have derived the expression for the density of conduction current in conventional SiO_2 films due to Fowler-Nordheim tunnelling as a function of the external electric field (E) in the form of

$$J_{FN} = A E^2 \exp(-B/E) \tag{2.35}$$

where the constant A and B depend on the barrier height and the effective mass of the tunnelling electron in the insulator. The pre-exponent A and the slope B, are given by [Ravindra and Zhoa 1992]

$$A = \frac{q^3 m_o}{16\pi^2 \hbar m_{ox} \phi} \qquad (A/V^2) \tag{2.36}$$

$$B = \frac{4}{3}\frac{(2m_{ox})^{1/2}}{q\hbar}\phi^{3/2} \qquad (V/m) \tag{2.37}$$

where q is the electron charge, $\hbar (= h/2\pi)$ is the reduced Plank's constants, m_o and m_{ox} are the electron mass in free space and in the SiO2 (insulator), respectively, $m_{ox} = 0.44m_o$ [Depas et al. 1995] is the effective mass of an electron in silicon dioxide, and ϕ is the barrier height (in electron volts) between the emitting electrode and the oxide. Since Equation 2.35 involves many known constants, it can be simplified as [Yang et al. 2004]

$$J_{FN} = 1.54 \times 10^{-6} \frac{m_o}{m_{ox}\phi} E^2 \exp\left[-6.83 \times 10^9 \left(\frac{m_{ox}}{m_o}\right)^{1/2} \frac{\phi^{3/2}}{E}\right] \tag{2.38}$$

where E is in V/m and ϕ in eV.

To check for this current mechanism, experimental *I-V* characteristics are typically plotted as $\ln(I/E^2)$ versus $1/E$, a so-called Fowler-Nordheim plot. Provided the effective mass of electron in insulator is known one can then fit the experimental data to a straight line with negative slope yielding a value for the barrier height. Since 1969, the FN model has been widely used to explain very well the conduction behavior in the conventional SiO2 films [Sze 1981; Depas et al. 1995].

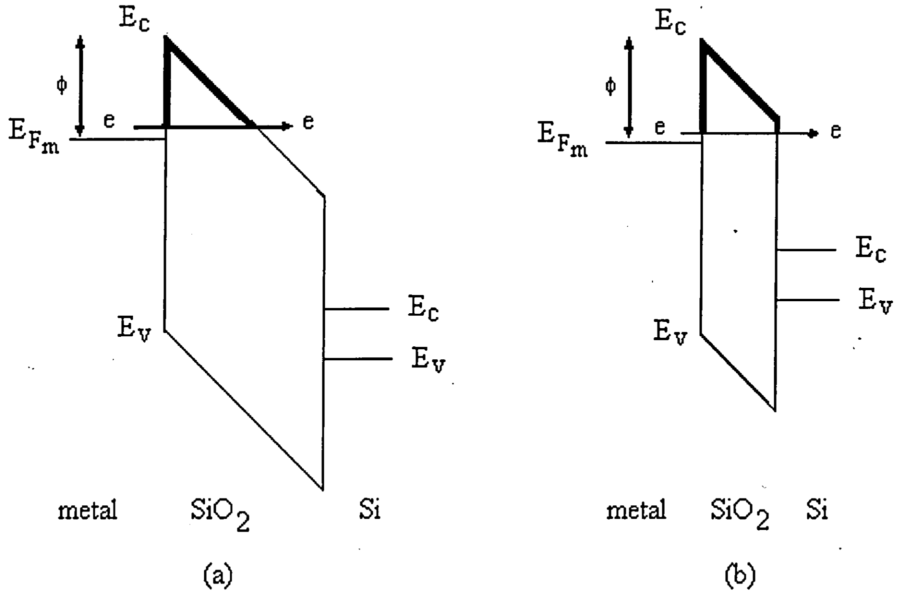

Figure 2.14. Effect of applied voltage on energy band diagram of MOS structure. (a) Fowler-Nordheim and (b) direct tunneling. Note the difference in the barrier shapes.

2.3.4 Space-charge-limited conduction

If the electrical contacts to an insulating or semiconducting sample are Ohmic, electrons can transfer between the electrodes and the sample and the resulting current is proportional to the applied voltage $(I \alpha V)$. However under certain conditions, the contacts can become super-ohmic and the current is only limited by the space-charge between the electrodes. This conductivity regime is called space-charge-limited [Tredgold 1966; Petty 1996]. The lowest voltage region of the curve corresponds to the situation in which the injection of excess carriers is negligible. At these voltages the volume conductivity dominates (i.e. Ohm's law). Only when the injected carrier density exceeds the volume generated carrier density will space-charge effects be observed and the quadratic current versus voltage dependence be observed.

In the absence of any trapping effects the current density J is given by the Mott-Gurney Law (1940)

$$J = \frac{9}{8}\mu\varepsilon\frac{V^2}{d^3} \tag{2.39}$$

where μ is the free carrier mobility, ε the permittivity of the material, V is the applied voltage and d is the distance between the electrodes. The current is assumed to be due to carriers of one sign only, the effect of diffusion is neglected, and the mobility is assumed to be independent of the field. For the case of a single set of traps, situated at energy E_t below the conduction band, and provided that the proportion of traps which are empty is not too small, a modified form of Equation 2.39 may be derived as [Murgatroyd 1969]

$$J = \frac{9}{8}\mu\varepsilon\frac{V^2}{d^3}\theta \tag{2.40}$$

The parameter θ represents the ratio of free to trapped charges given by

$$\frac{\rho_f}{\rho_f + \rho_t} = \theta = \frac{N_C}{N_t}\exp\left(-\frac{E_t}{kT}\right) \tag{2.41}$$

where ρ_f and ρ_t are respectively the free and trapped charge densities, N_C is the effective density of states in the conduction band and N_t is the density of traps. This equation has the form of the original Mott-Gurney law except that it shows that the presence of shallow traps in the forbidden gap reduces the total current density current by a factor of θ. As can be seen from Equation 2.41, the parameter θ is constant for a given value of temperature and is independent of the applied voltage. Figure 2.15 shows the SCLC characteristic as a function of bias voltage. The transition from Ohmic conduction $(I \alpha V)$ at low bias voltage to space-charge limited conduction $(I \alpha V^2)$ dominated by a single trapping level takes place at a certain value of applied voltage called transition voltage given by

$$V_t = \frac{q n_o d^2}{\theta \varepsilon} \tag{2.42}$$

where n_o is the concentration of thermally-generated electrons in the conduction band. The steep increase in the current observed after the square law regime corresponds to the filling of the traps. When the concentration of injected carriers from the contact are far more numerous than the density of traps, additional injected carriers are not trapped. The traps become filled (saturated) and the current density increases more rapidly. The threshold voltage at which all the traps become filled is called trap-filled-limit voltage. Density of the traps, N_t can be evaluated from trap filled limit voltage V_{TFL} [Lampert 1964]

$$V_{TFL} = \frac{q N_t d^2}{2\varepsilon} \tag{2.43}$$

Space-charge effects has been noted in several LB film systems. Roberts et al. have reported the I-V characteristic which followed SCLC in LB films of anthracene [Roberts et al. 1980]. Charge-injection effects have also been reported in multilayers of some charge-transfer complexes deposited onto glass substrates by the LB technique [Pearson et al. 1992].

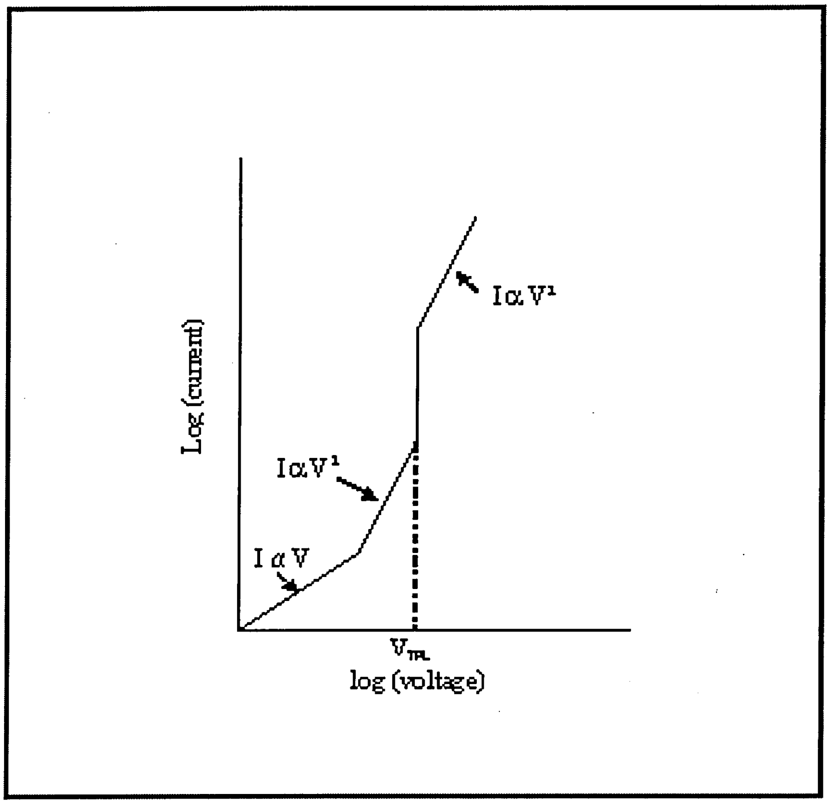

Figure 2.15. Space-charge-limited current (SCLC) versus voltage characteristics for an insulator containing traps. V_{TFL} is the trap-filled limit voltage.

2.4 Noise in electron devices

Electrical noise is the fluctuation of an electrical quantity, e.g. a current, a voltage or a resistance, changes unpredictably over time (stochastic process), which are superimposed to its average value and are influenced by the presence of localized defects and irregularities in the microstructure of the electron devices [Ciofi 2000]. The noise in electron devices is a useful parameter for estimation of device reliability analysis according to the fact that low frequency noise is sensitive to hidden device defects and degradation processes. The term 'noise' is normally used when such a stochastic process is stationary which means the average value and the variance of the quantity under observation are constant when evaluated at different time interval, as with power spectrum, whose behaviour against frequency does not depend on the time interval in which the estimation is performed [Ciofi 2000]. The power spectrum density of the measured fluctuation is a function of frequency and this spectrum contains infinite number of data. The examination of noise dependence on bias current and on temperature are the methods of discrimination between possible noise sources. In the case of bulk material, $1/f$ noise coming from the mobility fluctuations is proportional to the square of bias current. In diodes, where a diffusion or a recombination current dominates and the base region is wide, the noise scales linearly with the bias current. When the relation $S_I \alpha I^2$ is obtained in diodes, it is attributed to the influence of series resistances or to the surface recombination mechanism [Van der Ziel 1986]. The noise properties of forward biased diodes can provide information on the location of and nature of noise sources, as well as on the properties of traps located at the interface and in the space-charge region of the diode.

There are two types of sources of electrical noise, intrinsic and extrinsic noises (or excess noise). The former ones directly result from the conduction mechanisms within any electron device while the latter ones arises from the interaction between charge carriers and defects.

2.4.1 Thermal Noise

Thermal noise is the main type of noise which exists in almost all kinds of electronic systems. It does not depend on frequency thus, it is also called "white" noise. In general, the noise is due to random Brownian motion of charge carriers which occurs in all conductors under force-free environment regardless of the underlying conduction mechanism. By means of principles in thermodynamics and statistical mechanics Nyquist showed that the square of voltage within the frequency interval $d\nu$ across a pure resistance R and of temperature T is given by [Nyquist 1928]

$$E^2 = 4kTRd\nu \tag{2.44}$$

By using Equation 2.44 the mean-square open-circuit thermal noise voltage across a complex impedance of a two terminal network can be found as

$$\overline{v_{Th}^2} = 4kTBR(f) \tag{2.45}$$

and the equivalent mean-square short-circuit thermal noise current as

$$\overline{i_{Th}^2} = \frac{\overline{v_t^2}}{|Z|^2} = 4kTBG(f) \tag{2.46}$$

where k is Boltzmann's constant $\left(1.38\times10^{-23}\ \mathrm{J/K}\right)$, T is the absolute temperature, $R(f)$ and $G(f)$ are the real part of the impedance (Z) and the admittance $(\mathrm{Y} = {}^{1}\!/_{\mathrm{Z}})$ at frequency f, and B is the bandwidth over which the noise is measured. The equivalent open circuit and close circuit models are shown in Figure 2.16. The equivalent thermal noise voltage and current spectral density are given by [Burgess 1955].

$$S_V(f) = \frac{\overline{v_{Th}^2}}{B} = 4kTR(f) \tag{2.47}$$

and

$$S_I(f) = \frac{\overline{i_{Th}^2}}{B} = 4kTG(f) \tag{2.48}$$

respectively. For a capacitor with a dielectric modelled by a two terminal network of parallel RC circuit, where $Z = \dfrac{R}{1+j\omega RC}$, the thermal noise voltage spectral density $S_V(f)$ is given by [Kleinpenning 1998],

$$\begin{aligned} \mathrm{S_V(f)} = 4\mathrm{kT}\,\mathrm{Re}[\mathrm{Z}] = \frac{4\mathrm{kTR}}{1+\omega^2\mathrm{R}^2\mathrm{C}^2} = \frac{4\mathrm{kT}\varepsilon'/(\varepsilon''\omega\mathrm{C})}{1+(\varepsilon'/\varepsilon'')^2} \\ \approx \frac{4\mathrm{kT}\tan\delta}{\omega\mathrm{C}} \end{aligned} \tag{2.49}$$

where $Re[Z] = \frac{R}{[1+(\omega RC)]^2}$, ω the angular frequency $\omega = 2\pi f$, ε' and ε'' the real and imaginary part of the dielectric constant, $\varepsilon_r = \varepsilon' - j\varepsilon''$. The loss tangent is defined by $\tan\delta = \varepsilon''/\varepsilon'$, the capacitance $C = \varepsilon'\varepsilon_0 A/d$, and the loss resistance $R = d/(\omega\varepsilon''\varepsilon_0 A)$ with d and A are the thickness and area respectively. The corresponding thermal noise current spectral density is given by,

$$S_I(f) = 4kT\,\mathrm{Re}[Y] = \frac{S_V(f)}{R^2} = 4kTG = \frac{4kT\tan\delta}{R^2\omega C} \qquad (2.50)$$

where $G = 1/R$.

2.4.2 Shot Noise

The term "shot noise" was originally applied to the fluctuations of current in a saturated vacuum diode due to randomness of electron emission from the cathode. In 1918, Walter Schottky (1918) reported that shot noise ("schroteffekt") is one of the fundamental shortcomings (apart from thermal noise) of ideal vacuum tubes when all sources of spurious noise have been eliminated. In a vacuum tube, electrons are emitted by the cathode randomly and independently. The discreteness of electron charge q causes the current to be a Poisson process, which means that the mean squared fluctuation of the number of emission events is equal to the average count. The corresponding mean square current fluctuations equal to the product of q and the average current I divided by the total time of averaging.

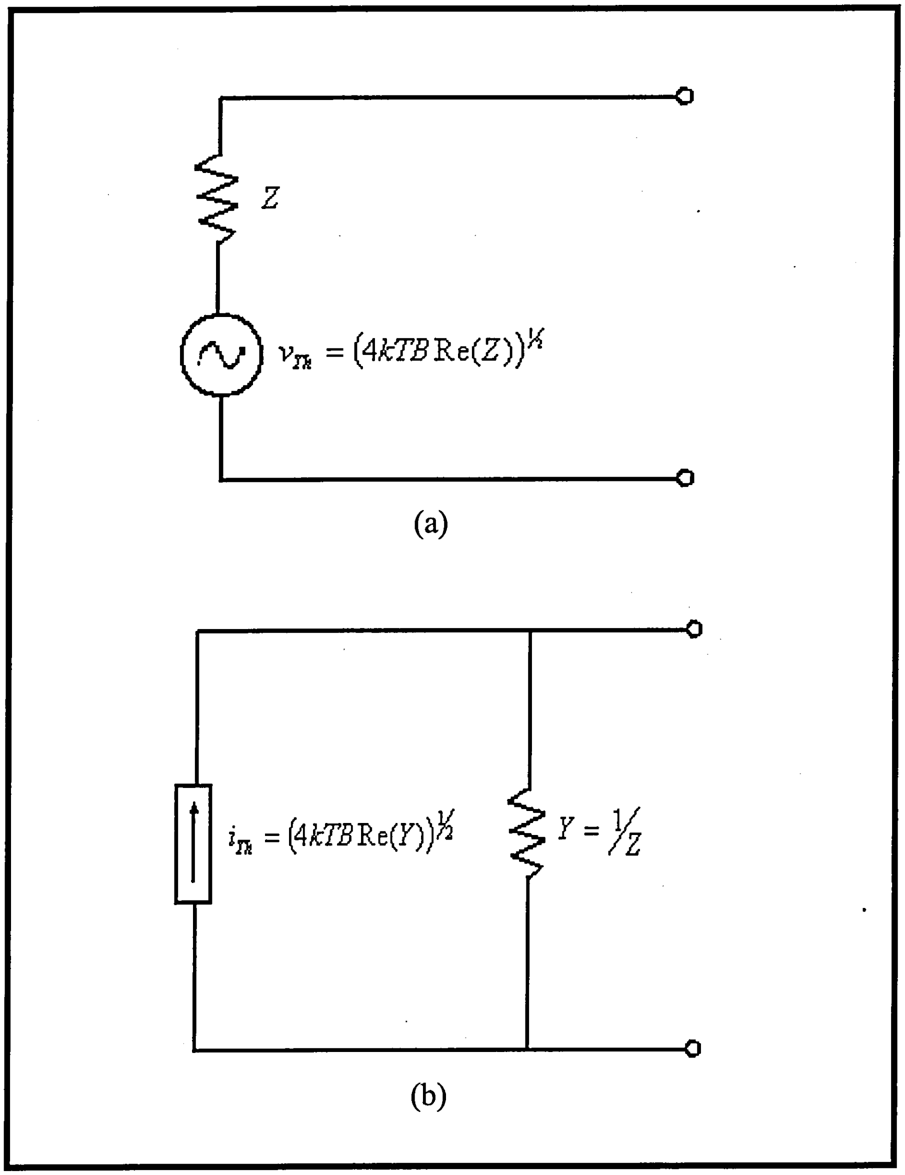

Figure 2.16. Thermal noise model of a complex two terminal network, (a) voltage noise model (b) current noise model.

This type of noise is present in all kinds of devices, including microscopic conductors as long as the applied voltage V is large compared to the thermal energy $qV >> 2kT$ [Nauen 2004]. The corresponding noise power spectra density $S(f)$ is given by

$$S(f) = 2qI \tag{2.51}$$

displays a linear dependence on the dc current I. The factor of 2 appears because positive and negative frequencies contribute identically [Beenakker 2003]. The noise power spectra density $S(f)$ is independent of frequency, thus it is a "white" noise. In general, shot noise is due to time-dependent fluctuations in the electrical current caused by the random transfer of discrete units of charge.

2.4.3 Generation-Recombination (G-R) Noise

G-R noise is classified as a "nonfundamental" noise sources since it relates the low-frequency noise to the existence of traps and imperfections in the crystal rather than basic crystal defect properties. The magnitude of the noise spectra is proportional to the trap density. The generation-recombination (G-R) fluctuations of the semiconductor conductivity are random processes and are due to generation and recombination of free charge carriers. The origin of G-R noise is related to the fluctuation of the number of free carriers caused by the presence of G-R centres in the semiconductor material and/or its interface. Each G-R centre can be characterized by a trapping energy level, E_T, in the bandgap and by a relaxation time, τ related to the capture, τ_C, and emission, τ_e time constants given by

$$\frac{1}{\tau}=\frac{1}{\tau_C}+\frac{1}{\tau_e} \tag{2.52}$$

If there are electron traps or donor atoms in the channel, and the temperature is so chosen that not all these centres are either occupied or empty, then the number of carriers in the sample will fluctuate due to processes of trapping and detrapping of the electrons. The continuous trapping and detrapping of the charge carriers causes a fluctuation in the number of carriers in the conduction and valence bands

The general equation for the rate of carrier number N in a semiconductor device is

$$\frac{dN}{dt}=g(N)-r(N) \tag{2.53}$$

where $g(N)$ and $r(N)$ are the generation and the recombination rates of carriers, respectively, are known function of N. By using Taylor expansion of $g(N)$ and $r(N)$ around the equilibrium value N_0, and Fourier expansion for $0 \le t \le T$, Van der Ziel has shown that for weakly n-type material, when a d.c. current I_0 flowing through a semiconductor device in which the number N of carriers fluctuates, the spectral density of the fluctuating current due to a single trap level with time constant τ is given by [Van der Ziel 1976]

$$S_I(f) = 4\frac{I_0^2}{N_0^2}\overline{\Delta N^2}\frac{\tau}{1+\omega^2\tau^2} \tag{2.54}$$

Where N_0 is the equilibrium number of carriers, $\Delta N = (N - N_0)$, $\overline{\Delta N^2}$ is the mean square value and τ the carrier lifetime. As can be seen from Equation 2.54 above, $S_I(f)$ α I_0^2, meaning that the above equation is a resistance (or conductivity) fluctuation model.

Equation 2.54 shows that a spectrum of the GR noise of conductivity in a semiconductor can be expressed, under equilibrium conditions, by a superposition of a number of lorentzians, $S_I(f) = \frac{A\tau}{1+\omega^2\tau^2}$, where A and τ depend strongly on temperature and on the parameters of the trap centers [Lukyanchikova 1997]. If more than one trap centre occurs in the semiconductor, the total G-R noise current spectrum is given by a summation of spectra by each individual trap centre,

$$S_I(f) = \sum_i^n \frac{A_i\tau_i}{(1+\omega^2\tau_i^2)} \tag{2.55}$$

At low frequencies ($\omega\tau \ll 1$) the spectrum is white (flat spectrum), that is independent of frequency, while at high frequencies ($\omega\tau \gg 1$) it varies as $1/_{f^2}$, and its half power point is at a corner frequency of $f_C = \frac{1}{2\pi\tau}$. The usefulness of G-R noise spectroscopy as a diagnostic tool is related to the fact that the relaxation time is strongly temperature dependent. By changing the temperature, the Fermi level shifts and thus τ. By plotting the current noise spectral density times frequency at a constant f vs. temperature, a peak-shaped curve is obtained. The peak maximun will shift toward higher temperatures for higher frequencies allows determination of activation energy of the trapping center [Claeys and Simoen 1998].

2.4.4 Flicker ($1/f$) Noise

Flicker ($1/f$) noise is an interesting ubiquitous type of fluctuation, appearing not only in measurements on electronic systems but also in a diverse range of observations elsewhere such as in biological systems [Evangelos 1997], musical [Gardner 1978, Voss and Clarke 1978], as well as in environmental phenomena e.g. thunderstorm and earthquake [Machlup 1981]. It is categorized by having the noise power spectral density $S(f)$ varying inversely to the frequency.

The first observations of $1/f$ noise were made in 1925 when J.B. Johnson found, in a thermionic tube, a noise whose spectral density increased with decreasing frequency. He proposed that this excess noise was due to the fluctuations in the work-function of the cathode surface due to particle migration. In 1926, W. Schottky suggested that this noise arises from slow random changes of the thermocathode's surface, and given the name "Fackelneffekt" ("flicker effect") or "flicker noise" [Kogan 1996]. After that, flicker noise in electronic devices received increasing attention and became an active research topic in electronics and physics. Bernamont (1937) reported the investigation of low frequency noise in non-metallic resistors which have similar behaviour with what Johnson discovered earlier in vacuum tubes. The same type of current noise spectrum was found in carbon microphones [Christensen and Pearson 1936].

After world war II, measurements of the low frequency noise spectra in electronic devices and materials have been performed on a vast number of samples, such as in semiconductors e.g. Germanium [Herzog and Van Der Ziel 1951; Montgomery 1952; McWhorter 1956], amorphous silicon [Bathaei and Anderson 1987; Johanson et al. 1996], in metals and contacts [Hooge 1969], on devices such as Schottky diodes [Hsu 1970] pn diodes [Kleinpenning 1985], laser diodes [Jang and Wu 1993], pin diodes [Wieczorek 1995], MOSFETs [Klaassen 1971; Celik-Butler and Hsiang 1987], MESFETs [Lambert et al. 2001], MODFETs [Viktorovitch et al. 1996], bipolar transistors [Sanchez et al. 2000], thin film transistors [Rhayem et al. 2000], and quite recently in dielectric materials [Gerard et al. 2001; Pavelka et al. 2002; Crupi et al. 2002; Min et al. 2005], organic thin film transistors [Martin et al. 2000; Necliudov et al. 2000; Ferrari et al. 2002], and nanostructure materials [Collins et al. 2000; Hoel et al. 2002; Ouacha et al. 2002; Kurdak et al. 2005].

2.4.5 $1/f$ noise models

Although there have been numerous work on $1/f$ noise in electron devices, during the past 45 years, the physical origin of the noise is still not fully understood, still a controversial dispute and is open to debate [Claeys and Simoen 1998]. Even though several models for $1/f$ noise have been proposed, no conclusive theory appears to be applicable for all electron devices. In general, there exist two main schools of thought, both with their own model and followers: the carrier number fluctuation (ΔN) model and the mobility fluctuation $(\Delta\mu)$ model. The first model was proposed by McWhorter

[Mcwhorter 1957] while the latter by Hooge [Hooge 1969]. For years, controversy exists between both models to explain the $1/f$ noise in MOSFETs. Experimental results indicate that the $\Delta\mu$ model is better suited for p-type MOSFETs, whereas the ΔN model is better suited for n-type MOSFETs [Chang et al. 1994]. Ideally, a single model, based on physical principles, should describe the low frequency $1/f$ noise in both n-type and p-type MOSFETs and in all operating regimes. As a result, unified $1/f$ noise models were proposed for that purpose.

2.4.5.1 McWhorter's number fluctuations model

McWhorter, working with germanium filaments at MIT Lincoln Laboratory, [McWhorter 1955,1957] has proposed a model which explained the existence of $1/f$ noise in semiconductor materials. In this model, the carriers number fluctuation due to trapping and detrapping of charge carriers in traps located at a distance from semiconductor-oxide interface is considered as the source of noise and concluded that the noise is a 'surface effect'.

In general, surface states are defined as any electronic state which is localised at the surface, with its wavefunction having a maximum amplitude at or near the surface and vanishes at sufficiently great distance from the surface. In this respect, states in the oxide near the interface or at the interface and in the accumulation or inversion-layer region of the silicon can be classified as 'suface states' [Hooge 1981]. In electron devices, trapping and detrapping of free carriers can be by surface traps in the MOS capacitor of MOSFETs, in the surface oxide on the base of a BJT, and on the surface of the space-charge region of a p-n junction or in bulk space-charge region of a JFET. This type of noise is called "nonfundamental" $1/f$ noise since the magnitude of their spectra is proportional to the trap density which means that, the noise effect can be reduced by eliminating most of the traps.

The McWhorter school of thought believes that the $1/f$ noise;

(i) originates from the *surface* (not from the bulk materials)

(ii) is generated by fluctuations in the *number of carriers* due to charge trapping in surface states (not due to fluctuation in the carrier mobility)

McWhorter obtained the necessary $1/f$ spectrum by assuming that the time constant τ of the surface states varied with $1/\tau$ distribution. By analogy to a single trap level with a time constant τ responsible for Lorenzian G-R noise, (as mentioned in section 2.5.3 G-R noise) the discrete, multiple-trap levels can produce a G-R spectra according to

$$S_N(f) = 4\sum_{i}^{n} \overline{\Delta N_i^2} \frac{\tau_i}{[1+(\omega\tau_i)^2} \tag{2.56}$$

It has been found that the G-R spectra from discrete multiple-trap levels lead to a $1/f$ rather than Lorenzian spectrum by a proper distribution of the time constants. By analogy to Equation 2.56, the noise spectra can be wtitten as

$$S_N(f) = 4\overline{\Delta N^2} \int_0^{\infty} \frac{\tau g(\tau)d\tau}{1+\omega^2\tau^2} \tag{2.57}$$

where $g(\tau)d\tau$ is the time constant distribution with distribution function proportional to $1/\tau$. Mcwhorter proposed a distribution of time constants over a wide range of τ between τ_1 and τ_2 with statistical weight $g(\tau)$ as

$$g(\tau)d\tau = \frac{1}{\ln(\tau_2/\tau_1)}\frac{1}{\tau}d\tau \qquad \text{for} \quad \tau_1 < \tau < \tau_2 \tag{2.58}$$

$$= 0 \qquad\qquad \text{elsewhere}$$

where τ_1 and τ_2 are the two limits of the time constant of G-R centers. The above distribution gives a $1/f$ noise as the discrete multiple trap levels merge to form a continuous trap distribution in the frequency range $\frac{1}{\tau_2}$ to $\frac{1}{\tau_1}$ given by [Hooge 1981]:

$$S(f)=\int_{\tau_1}^{\tau_2} g(\tau)\overline{\Delta N^2}\frac{4\tau}{1+(2\pi f\tau)^2}d\tau=\frac{4\overline{\Delta N^2}}{ln(\tau_2/\tau_1)}\frac{1}{f}\int_{\tau_1}^{\tau_2}\frac{1}{1+(2\pi f\tau)^2}d\tau$$
$$=\frac{\overline{\Delta N^2}}{ln(\tau_2/\tau_1)}\frac{2}{\pi}(tan^{-1}2\pi f\tau_2-tan^{-1}2\pi f\tau_1)\frac{1}{f} \qquad (2.59)$$

This equation can be approximated and give the $1/f$ spectrum in three different sections of frequency as follows:

$$S(f)=\begin{cases}\dfrac{\overline{\Delta N^2}4\tau_2}{ln(\tau_2/\tau_1)} & \text{for } f \ll 1/2\pi\tau_2\\[2ex] \dfrac{\overline{\Delta N^2}}{\ln(\tau_2/\tau_1)}\dfrac{1}{f} & \text{for } 1/2\pi\tau_2 < f < 1/2\pi\tau_1\\[2ex] \dfrac{\overline{\Delta N^2}}{\pi^2\tau_1\ln(\tau_2/\tau_1)}\dfrac{1}{f^2} & \text{for } f \gg 1/2\pi\tau_1\end{cases} \qquad (2.60)$$

The noise spectrum shows $1/f$ behaviour for $1/\tau_2 < \omega < 1/\tau_1$, a flat spectrum for $\omega\tau_2 \ll 1$ and varies as $1/f^2$ for $\omega\tau_1 \gg 1$. The above derivation is limited only when there is no interaction between trap levels at different energies (isolated traps). If the levels are interacting with each other, a Lorentzian spectrum is found instead of a $1/f$ noise spectrum [Hooge 1994]. In most cases τ_2 is very long and τ_1 is very short that only the $1/f$ part of the spectrum is observed.

Christensson et al. [1968a, 1968b] were the first to apply the McWhorter theory to MOSFETs using the assumption that the necessary time constants are caused by the tunneling of carriers from the channel into traps located inside the oxide. Until now Mcwhorter's model has remained the most accepted model for $1/f$ noise in MOSFETs. For MOSFETs, at weak inversion, the $1/f$ noise current spectral density, can be expressed as [Wong 2003]

$$S_{I_D}(f) = \frac{kTq^2 I_D^2 N_T(E_F)}{C_i^2 LW(V_{GS} - V_T)^2 \ln(\tau_2/\tau_1)} \frac{1}{f} \qquad (2.61)$$

for $\frac{1}{\tau_2} < \omega < \frac{1}{\tau_1}$

where $N_T(E_F)$ is the trap density per unit energy at in the vicinity of the fermi level (E_F), τ_1 and τ_2 the lower and the upper boundaries of the time constants involve in the trapping-detrapping process, k is the Boltzmann constant, and C_i, V_G, V_T, LW, are the oxide (or insulator) capacitance per unit area, gate voltage, threshold voltage and channel area (length x width) respectively. As a note, although many investigations have been made on $1/f$ noise in MOS devices, inconsistencies in the experimental results still exist among different reseachers.

It has been found that the McWhorter theory can be applied succesfully in devices where current transport is parallel to the semiconductor surface i.e. all field effect transistors and metal-oxide-semiconductor devices [Dobrzanski 2004]. In devices where transport is vertical such as in diodes and heterojunction bipolar junction transistors, this $1/f$ noise mechanism may be considered as a special surface contribution to the noise especially in the case where the ratio of the devices perimeter to its area is high [Takanashi and Fukano 1998]

2.4.5.2 Hooge's mobility fluctuations model

In 1969, Hooge F.N. [1969] has proposed a simple mathematical model based on carrier mobility fluctuations $(\Delta\mu)$ which well decribe $1/f$ noise phenomena in bulk material. He correlated a large number of experimental data obtained by different authors on the magnitude of $1/f$ noise in semiconductor and metal films and found that $1/f$ noise is inversely proportional to the total number of mobile charge carriers in homogeneous samples. Later, [Hooge and Hoppenbrouwers 1969] measured the $1/f$ noise voltage generated in homogeneous gold films in the presence of a steady current. They found that the noise power spectrum density of the current fluctuations across the homogeneous sample under constant voltage conditions at room temperature could be expressed by an empirical formula:

$$S_I(f) = \frac{\alpha}{N}\frac{I^2}{f} \tag{2.62}$$

where $N = l^2 / q \mu R$ is the number of the charge carriers in the sample, where R is the sample resistance, l the length of the resistor, μ the mobility of free charge carriers, q the elementary charge, f is the frequency, and α is a dimensionless constant known as Hooge parameter. According to this model, the spectral density is independent of temperature and material parameters and is a power law at all frequencies. The $1/f$ noise is considered as arising from resistance fluctuations that generate a fluctuation voltage in the presence of a steady current. The Hooge formulation relies on the low frequency interactions between carriers and phonons in the bulk material, resulting in carrier mobility fluctuations.

The Hooge school of thought believes that the $1/f$ noise;

(i) originate from the bulk materials and not from the surface

(ii) is due to fluctuation in the carrier mobility instead of fluctuation in the number of carriers.

Due to Ohm's law, Equation 2.62 can be written in a more diverse way in Ohmic or homogeneous systems as [Hooge 1981]

$$\frac{S_I(f)}{I^2} = \frac{S_V(f)}{V^2} = \frac{S_R(f)}{R^2} = \frac{S_G(f)}{G^2} = \frac{\alpha}{Nf} \tag{2.63}$$

where I, V, R, and G are the dc current, dc voltage, resistance, and dc conductivity respectively.

According to this equation, the spectral density is independent of the measuring conditions, such as current (or voltage), temperature and material parameters, and is a quadratic power law at all frequencies. This empirical equation was based on the mobility fluctuations of simple homogeneous materials such as bulk metals. Over the years after Hooge derived his formula in 1969, the value α_H was found to be a "magic number", fixed at about 2×10^{-3} for all samples. Over the years, Hooge and many other reseachers have reported devices which show flicker noise that is consistent with this magic number such as that given in [Hooge 1976; vandamme 1974; Hooge and Kleinpenning 1975; Kleinpenning 1976; Strocken and Kleinpenning 1976; Vandamme et al. 2002; Zhao et al. 2004].

But now, it is clear that α_H is not a constant. More recent experiments have suggested that α_H is not as independent of the sample material, size and temperature as originally thought. Its value has been found to vary from 10^{-2} to 10^{-9} in different semiconductors and under different conditions [Lukyanchikova 1997]. However the α_H value can be used as a quality assessment of materials.

2.4.5.3 Unified Model

As described in the previous section, $1/f$ noise in MOSFETs can be modelled by either the number of fluctuation model, or by mobility fluctuations model. However, trapped channel carriers not only change the number of carriers but also influence mobility due to Coulombic scattering by these traps. As a result, it is difficult to differentiate between the two models (Hooge and McWhorter) when it involves nonhomogeneous materials/devices. The current fluctuations (ΔI) can be a combination of both carrier number and mobility fluctuations as given by [Claeys and Simoen 1998].

$$\Delta I \approx \mu \Delta N + N \Delta \mu + \Delta(\mu N) \tag{2.64}$$

The origin of the $1/f$ noise is usually governed by carrier number fluctuations (ΔN) with a $\Delta\mu$ correction as a second-order effect, which can be noncorrelated $(N\Delta\mu)$ or correlated $\Delta(\mu N)$ with the ΔN process. The conductance fluctuations are characterized by a power spectral density proportional to $1/f^{\gamma}$.

The $1/f$ noise is often expressed in circuit simulation-oriented equations modeling such as BSIM3v3 without bothering about ΔN or $\Delta\mu$. Futhermore, many reseachers such as [Simoen and Claeys 95], [Jang et al. 1993] and [Chen et al. 2000], have found that by summarizing their experimental data, the current noise spectral density can be well represented by an equation which is a modification of Hooge's empirical model, given as

$$S_I(f) \propto \frac{I^{\beta}}{f^{\gamma}} = C\,\frac{I^{\beta}}{f^{\gamma}} \tag{2.65}$$

where C is a flicker noise coefficient or magnitude, which is a device-dependent factor and can be considered as a quality indicator of the device. It is strongly dependent on device processing and technology [Martin et al. 2000]. Typical value for β and γ in semiconductor materials are in the range of $0.7 < \gamma < 1.4$ [Celik-Butler and Hsiang 1987] and $1 < \beta < 3$ [Leach 1994] respectively. The origin of the $1/f$ noise can be investigated by analyzing the bias-current dependence of $S_I(f)$. The flicker noise exponent β, which depends on diode ideality factor and the bias current range, will determine the origin of the $1/f$ noise in the device under test (DUT) [Chen et al. 2000]. This value is a measure of the mixing of various noise sources in the device or of the volume versus surface nature of the noise mechanism [Martin et al. 2000]. γ is a measure of the distribution of traps responsible for carrier number fluctuations [Martin et al. 2000]. For $1/f$ noise associated with pure G-R events, the current exponent β becomes 2/n with n being the ideality factor.

This empirical equation is more appropriate in describing the $1/f$ noise in complex structures since the noise can be a combination of bulk and surface effect [Dutta and Horn 1981]. It has been used widely in nonhomogeneous devices such as in semiconductor diodes, e.g. a-Si:H pin diodes, [Wieczorek 1995], AlGaInP laser diodes [Chen et al. 2001] and organic materials e.g. conducting polymers [Bruschi et al. 1996].

CHAPTER 3

Experimental Methodology

3.1 Introduction

The films investigated in this study were insulating LB films of stearic acid transferred from the subphase containing metallic cadmium (Cd^{2+}) cations. Composite LB films were deposited onto n-type silicon substrate and MIS structures were fabricated containing these stearic acid films and will be refered as as "untreated" samples. Some LB films of composite stearic acid were then treated with hydrogen sulphide gas in order to introduce cadmium sulphide (CdS) nanoparticles into the untreated matrix. These MIS structures will be named as "treated" samples. The fabrication of MIS structures involved careful preparation of silicon (Si) substrates, and deposition of thin organic film and electrical contacts.

This chapter is organised into three major sections. Section 3.2 is devoted to the procedures utilised for the fabrication of devices used in this study. Sections 3.3 and 3.4 are concerned with the experimental methods employed to investigate the device characteristics. Carrier transport mechanisms were studied by making d.c. and a.c. measurements on both types of samples and these techniques are described in section 3.3. The investigation of low frequency noise forms an important component of this work and the design of the low-frequency noise measurements set-up will be presented in Section 3.4.

3.2 Device fabrication

The fabrication of devices used in this study were performed in a clean room (class 100) environment following carefully drawn up procedures including health and safety guidelines. A cleanroom is an environment where airborn particulates are controlled through an exchange of highly filtered air using a high effeciency particulate air (HEPA) filtering system, and through minimization of activities that generate particles. A class 100 cleanroom maintains less than one hundred particles larger than 0.5 microns in each cubic foot of air space. The methods for device fabrication involved etching and cleaning of silicon substrates, preparation of the LB trough, LB film deposition, cadmium sulphide (CdS) nanoparticles formation, and metal contact deposition.

3.2.1 Substrate preparation

Subtrates in this investigation were n-type silicon wafers (100). The thickness and resistivity (ρ) were approximately 300 μm and 4.5 Ω.cm, respectively. As part of the device requirements, silicon dioxide (SiO_2) layers with thickness in the range of 0.8 μm to 1.5 μm were thermally grown on top of the silicon wafers. The wafers were then cut to the dimension of a glass slide which was approximately 76 mm x 26 mm. A part of the SiO_2, approximately 15 mm, was then etched in a mix of hydroflouric (HF) acid and milipore water (18 MΩ.cm) with a moderate concentration ratio of 1:5, resulting in 15 mm width of bare silicon substrate.

Figure 3.1 illustrates the steps of work involved in substrate preparation. LB film deposition took place on the etched area. The remaining silicon dioxide layer was used to prevent undesirable effects due to short-circuiting when wire contacts are made using silver conducting paste. As part of health and safety requirements, special hand gloves, coat, and protective glasses were worn in order to minimize the risks associated with the HF etching process.

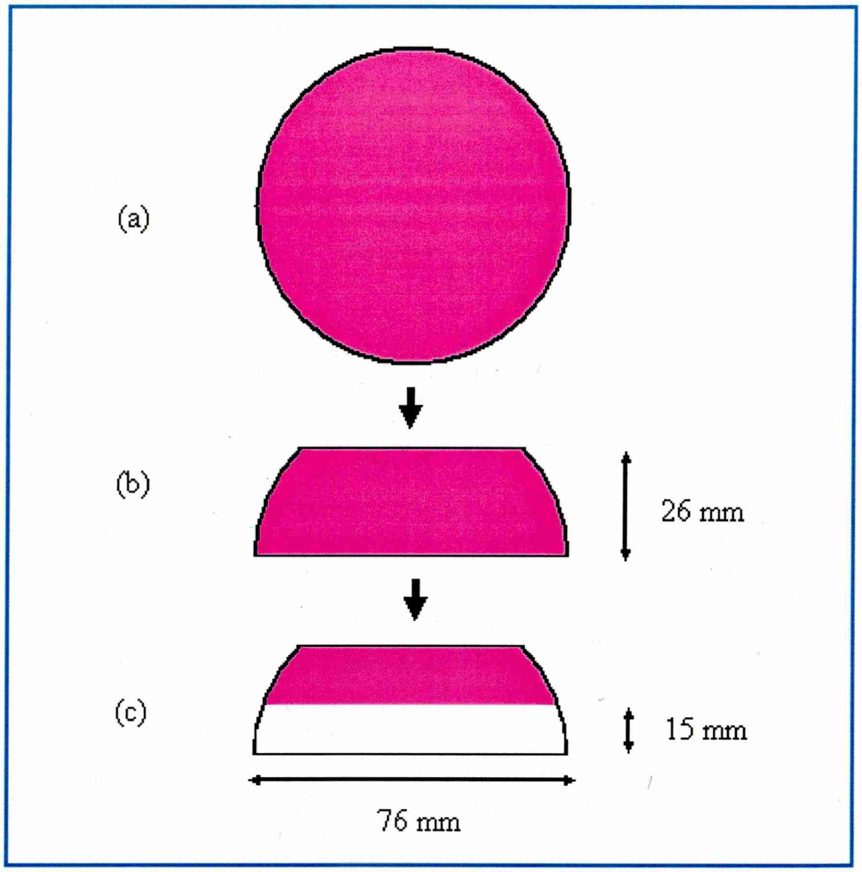

Figure 3.1. Processes in substrate preparation.

(a) n type silicon wafer with top surface grown with SiO_2

(b) silicon wafer in (a) cut to the size of a microscopic glass slide

(c) part of SiO_2 in (b) were etched using hydrofluoric acid, resulting in bare silicon area approximately 76mm ×15 mm.

The etching process was undertaken with sufficient care in order to achieve the targeted area for device fabrication. The junction between silicon dioxide and silicon wafer was made graded over a relatively large area in order to avoid possible undesired effects caused by abrupt edge. Upon completion of the etching process, the substrates were then thoroughly washed with Millipore water for 5 minutes and dried with nitrogen gas. Further substrate cleaning was performed by washing with Decon Neutracon in an ultrasonic bath for 30 minutes and washed with flowing Millipore water for at least 5 minutes and finally dried with nitrogen gas. Prior to the film deposition, the silicon substrates were exposed to hexamethydisilazane vapours overnight in order to produce hydrophobic surfaces.

3.2.2 Film deposition

A PC-controlled Langmuir-Blodgett trough (model 622D2) from Nima Technology Ltd., UK with a total trough volume of approximately 1.4 liter was used in this work. The trough was cleaned thoroughly by using chloroform and propanol alternately with dust-free wipes (Kimberly-Clark) which are recommended for an LB trough. The water used for subphase is purified Mili-Q water of resistivity of about 18 MΩ.cm and pH value of 5.5. Cadmium chloride solution with concentration of 0.1 mol/l was prepared by dissolving 18.3 g of $CdCl_2$ salt into 1 liter of water. An amount of 6 ml of the solution was mixed thoroughly into the subphase and a $CdCl_2$ solution was produced with a concentration of approximately 5×10^{-4} M. The molecular weight of $CdCl_2$ is 183.3 g/mol.

Monolayers of stearic acid molecules were formed by carefully spreading 80 μl of its solution drop by drop, at different places onto the surface of water subphase. The concentration of the stearic acid solution used was 1 mg/ml in chloroform. Cadmium chloride salt, chloroform and stearic acid used were of high purity grade. A period of 20 - 30 minutes was found to be sufficient for the evaporation of any residual solvent to take place prior to the compression of the barriers. The surface of the subphase was visually monitored and contaminations on the surface were removed by siphoning using a vacuum pump, prior to the spreading of stearic acid solution.

Films deposition took place at room temperature and the pH of the subphase was held at 5.5. The monolayer was compressed at target pressure of 28 mN/m and the pressure was maintained at that level throughout the deposition process. Dipping speeds for downward and upward strokes were set to 15 mm/min and 20 mm/min respectively, with a 3 minutes time interval to allow sufficient drying of the film. Forty monomolecular layers of LB film of stearic acid (SA) molecules were transferred from the subphase onto the n-type silicon substrate by the vertical dipping method. This required spreading stearic acid solution several times onto the water surface. The thickness of the film was estimated to be 100nm due to the fact that monolayer thickness of stearic acid is approximately 2.5 nm [Petty 1996].

After the deposition process had been completed, the back of the silicon substrate was cleaned with chloroform to remove the LB films there. Part of the silicon substrate was then cut into two similar halves. One half was used for nanoparticles formation by exposure to H_2S gas. The other part was kept in a sealed glass dessicator and was not exposed to any gas.

3.2.3 CdS nanoparticles formation

Smotkhin et al. have found that Langmuir-Blodgett films of fatty acid salts were suitable materials for the formation of inorganic nanometer-size semiconductor particles within their matrix [Smotkin et al. 1988]. By placing the films into hydrogen sulfide (H_2S) atmosphere it was found that metal-sulfide particles were grown in the form of nanocrystals. CdS nanoparticles in LB films were formed according to the following chemical reaction of bivalent metal ions in LB films with H_2S [Erokhin et al. 1998].

$$[CH_3(CH_2)_nCOO]_2^- M^{2+} + H_2S \rightarrow 2[CH_3(CH_2)_nCOOH] + MS \qquad (3.1)$$

where, M is a bivalent metal, cadmium (Cd) is this case. Hydrogen sulphide gas (H_2S) was generated by adding a small amount of ferrous sulphide (FeS) into hydrochloric acid (HCl) diluted with water (ratio1:1) and the following chemical reaction took place:

$$2HCl + FeS \rightarrow H_2S + FeCl_2 \tag{3.2}$$

Hydrogen sulphide exposure of multilayer LB films was carried out in a sealed glass chamber at room temperature and under atmospheric pressure for a period of 12 hours. The formation of CdS nanoparticles in stearic acid matrix was confirmed using atomic force microscopy (AFM) and UV-Vis absorption spectroscopy [Nabok et al. 2003].

The blue shift in the absorption spectra of similar composite films was attributed to quantum confinement effects associated with the formation of CdS nanoparticles [Dhanabalan et al. 1996]. Large CdS clusters inside the LB films matrix were formed due to particles agregation. AFM images showed pseudo three dimensional (3D) CdS clusters having a shape of hexagonal platelets with lateral dimensions of 20-30 nm [Iwantono 2003]. The increase in LB film roughness was attributed to nanoparticles formation in the multilayer structure. In contrast, these effects were not observed in untreated stearic acid LB films, which showed a smooth suface morphology.

3.2.4 Electrical contacts

Using an Edwards E306A thermal evaporator, aluminium electrodes were deposited on top of the LB film surface (top contact) and on the back of the silicon substrate (bottom contact). The procedure for metal contact deposition started with placing the metal source on a tungsten filament. The evaporation chamber was then pumped down to a pressure lower than 2 x 10^{-5} mbar .When sufficiently large current is passed through the filament, the metal sublimed onto the target substrate above the source, producing a thin metal film. The thickness of the contacts and the rate of coating were both monitored in-situ by using a quartz crystal microbalance (QCM).

Aluminium has the work function (ϕ_{Al}) of 4.1 eV. Since work function ϕ_{nSi} of the silicon was estimated to be $4.35eV$, an Ohmic contact was believed to have formed between aluminium and the n-type silicon substrate. For top contacts, a stainless steel masking plate, as depicted in Figure 3.2, was used to pattern the top electrodes so that the multiple device structures were obtained.

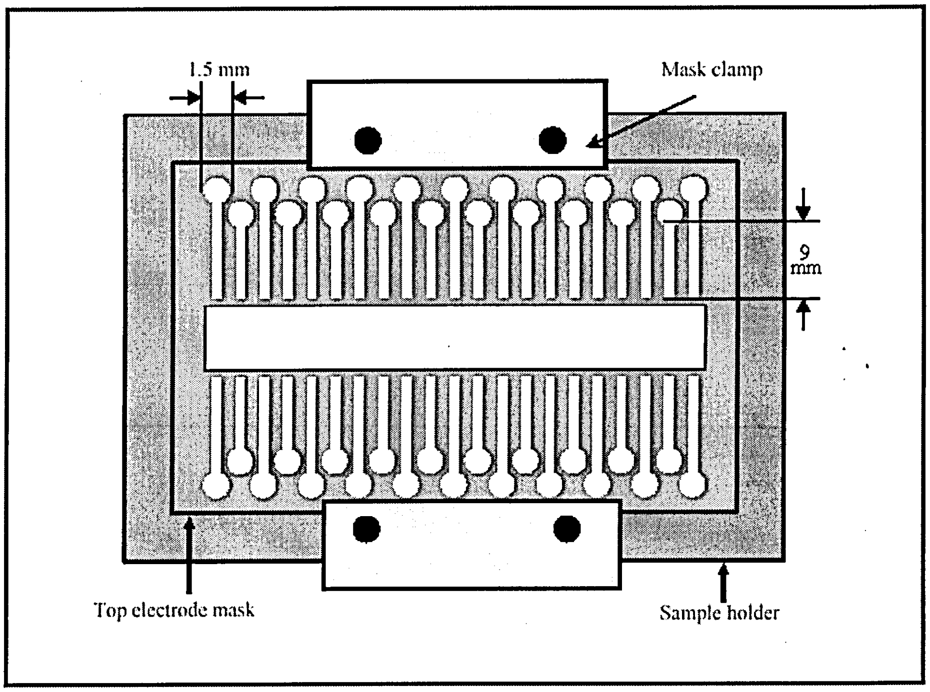

Figure 3.2. A metal plate mask used for top contacts

Great care was taken during evaporating the top contact to avoid damage to the LB films. A very slow evaporation rate of less than 0.1nm/s was carried out for top electrodes while a fast rate of 0.5 to 5 nm/s for bottom electrode. The metal film thicknesses were measured by quartz crystal film thickness monitor and were approximately 40nm and 100nm for top and back contacts respectively. Once the metallisation process was completed, silicon-based devices of metal-insulator-semiconductor (MIS) structure are formed as shown in Figure 3.3. The active area for the MIS structures containing untreated and treated LB films was in the range of 2.5 mm^2 to 3.5 mm^2. The electrical connection to the devices was made by cementing thin copper wires to the metallic contacts using silver paste. The untreated device (SA) was used as a reference sample for comparing the experimental results.

Figure 3.4 shows the equivalent circuit model of MIS capacitor for device shown in Figure 3.3. C_{SiO_2} is the equivalent capacitance of the SiO_2 layer which is in parallel with the frequency independent insulator capacitor (C_i). R_i is the insulator resistance, R_S is the series resistance of the substrate and contacts and C_{Dep} is a depletion capacitance in the substrate.

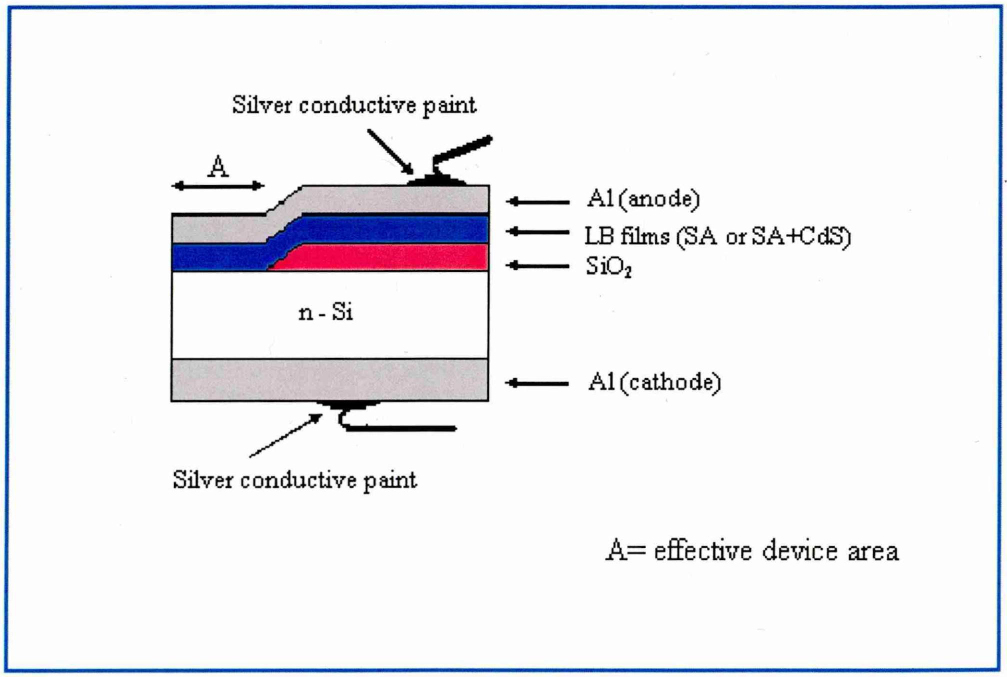

Figure 3.3. A schematic diagram of a fabricated device in MIS structure.

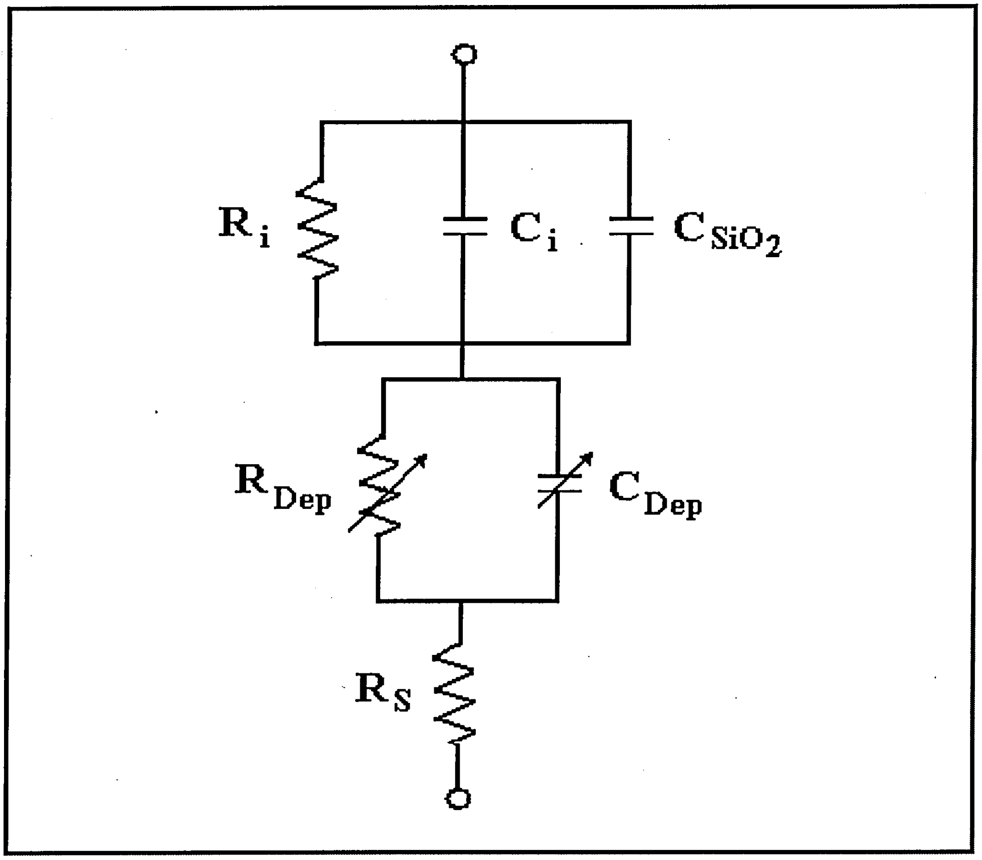

Figure 3.4. Equivalent circuit model of MIS device in Figure 3.3.

3.3 Leakage current measurements

A schematic diagram of the electrical measurement arrangement is shown in Figure 3.5. The set-up consisted of a Hewlett Packard 4284A Presicion LCR meter (impedance analyser), a Keithley 6517A digital electrometer, an Oxford Instrument cryostat, and an Intelligent Temperature Controller ITC-4. A personal computer (PC) was used to control the measurements via a GPIB IEEE-488 interface card. A Farnell SW1B IEEE-488 switching unit provided the measuring equipment connection to the PC whilst the temperature controller was controlled directly by a PC via a serial port.

Electrical measurements which consist of dc leakage current-voltage (I-V) characteristics and ac impedance measurements were carried out on both treated (SA+CdS) and untreated (SA) LB films of stearic acid in MIS structure devices. The measurements were performed in the dark at room temperature and also under vacuum in a cryostat for temperatures in the range between $80\,\text{K}$ and $380\,\text{K}$. I-V characteristics measurements were performed in the dc voltage bias range of -3V to 3V with a 50mV step and with a time delay of 5 seconds between successive measurement.

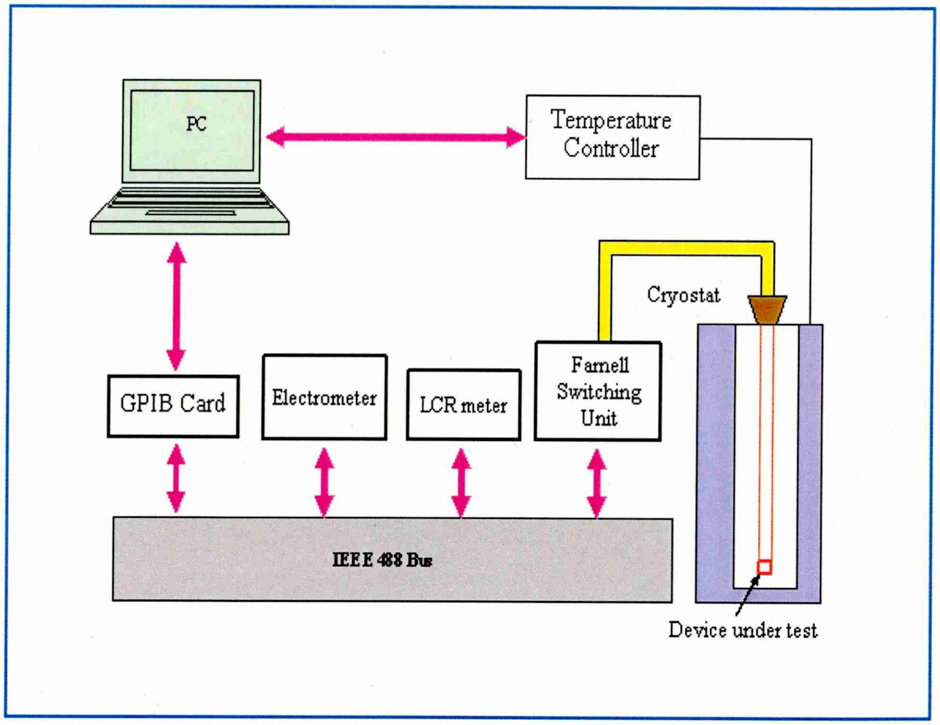

Figure 3.5. Schematic diagram of the electrical characterisation system

Impedance spectroscopic measurement was used to measure capacitance (C) and conductance (G) simultaneously as a function of either frequency (CGF) or dc voltage (CGV). Prior to measurement the LCR meter was calibrated for conductor cables used in connecting the samples by open and short-circuit test. For CGF, measurements were made by applying a small a.c. signal of $V = 20\,mV_{rms}$ with frequency varied in a semi-logarithmic preset steps from 20 Hz to 1 MHz at zero dc voltage. For CGV, a small a.c. signal of $V = 20\,mV_{rms}$ with modulating frequency set to several chosen values was superimposed on a d.c. voltage and swept between $\pm 3V$ which is found to be low enough in order to avoid any possibility of device damage. The d.c. bias sweep was

$0.01\,\mathrm{Vs}^{-1}$. It was found that the chosen time delays ($5\,\mathrm{s}$ for the d.c. and $10\,\mathrm{s}$ for the a.c. measurements) were appropriate in order to get stabilised measurements.

3.4 Low-frequency noise measurement (LFNM)

The same MIS devices (treated and untreated) were used as devices under test (DUT) to perform the low frequency noise measurement. When measuring the low-frequency noise, the challenge is to be able to measure the noise introduced solely by the DUT without the contribution of the rest of the system such as bias sources, amplifiers, and power line frequency. With an extremely low level of signal fluctuations in the DUT which need to be measured in performing meaningful LFNMs, the task is always difficult. The movement of the people near to the measurement system causes significant fluctuations in the measured signal. Futhermore, unwanted noise contributed by other components of the measuring system, such as cables, amplifier noise, mains power, has an adverse effect on the signal. In order to overcome these problems, appropriate instruments and techniques were employed in the first place.

The noise power spectral density (PSD) contains a wide range of signal levels. It is important that the measurement equipment is able to resolve the lowest level in presence of the highest level input to the equipment. Two instrumental issues need to be resolved in order to have a correct measurement; the dynamic range and the analog bandwidth of the measurement equipment. In this work, the equipment used in the designing of the measurement set-up met these two requirements. Since the noise arising from the DUT was our main concern, care was taken to reduce the system background noise (or noise floor) of the measurement system to as low as possible. Because of that, the equipment and the electronic components used in designing the measurements set-up had some special requirements. As a result, the whole measuring system was at maximum performance and was not prone to external influences, on the measurement results. An extensive amount of work was performed to make sure that the system noise (or noise floor) was not influenced by noise other than that from the DUT.

3.4.1 Measurement System Design

Different low frequency noise measurement setups are used in practice, but some common features were found in all cases. The basic requirements for any low frequency noise measurement system are an amplifier system with high gain and very low background noise, a spectrum analyser with suitable dynamic range and bandwidth to cover the frequency range of interest and shielding and filtering to avoid influence of external interference.

The measurement set-up used for low frequency noise investigations consisted of low noise biasing circuit, DUT, transimpedance amplifier, dynamic signal analyser and a personal computer which runs a LabView-based program, as schematically presented in Figure 3.6. A photograph of this experimental set-up is shown in Figure 3.7. This set-up was designed based on a circuit presented by [Hadap et al. 1999] for measuring low frequency noise in a two terminal device. The noise equivalent model of the measurement set-up is depicted in Figure 3.8.

The transimpedance amplifier was the most important piece of equipment in this set-up. It detected the fluctuation in the dc bias current, amplifies and converts it to voltage signal fluctuations at the output which will be picked up by the dynamic signal analyser and display the output as voltage power spectral density ($S_V(f)$).The amplifier used in this study was a popular EG&G 5182 current preamplifier which is an ultra low noise amplifier (ULNA) designed for use whenever the input signal is a current with maximum analogue bandwidth of 100 kHz. The sensitivity is switch-selectable with five settings enabling the amplifier, on its most sensitive range (10^{-8} A/V Low Noise) to detect fractions of a nanoampere without noise degradation, while on its lowest sensitive range (10^{-5} A/V) can sink current up to 9 mA without overload. At its highest sensitivity, the background noise current spectral density is extremely low, of at most $2.3\times10^{-28}\,A^2/Hz$, in the frequency range of $1Hz < f < 1kHz$ which is excellent for low level current noise measurements. This is the minimum noise level measurable in any measurements.

The dynamic signal analyzer calculates the voltage noise spectral density of the trans-impedance amplifier ac output voltage as expressed by

$$S_V(f)=\left|S_{I_A}(f)+S_{I_{DUT}}(f)\right|\bullet A(f) \tag{3.4}$$

where $A(f)$ is the gain, $S_{I_A}(f)$ and $S_{I_{DUT}}(f)$ are the current noise spectral density of the transimpedance amplifier and device under test (DUT) respectively. By using Equation 3.4 the current noise spectral density of the device under test can easily be obtained. The schematic diagram of the transimpedance amplifier is shown in Figure 3.9.

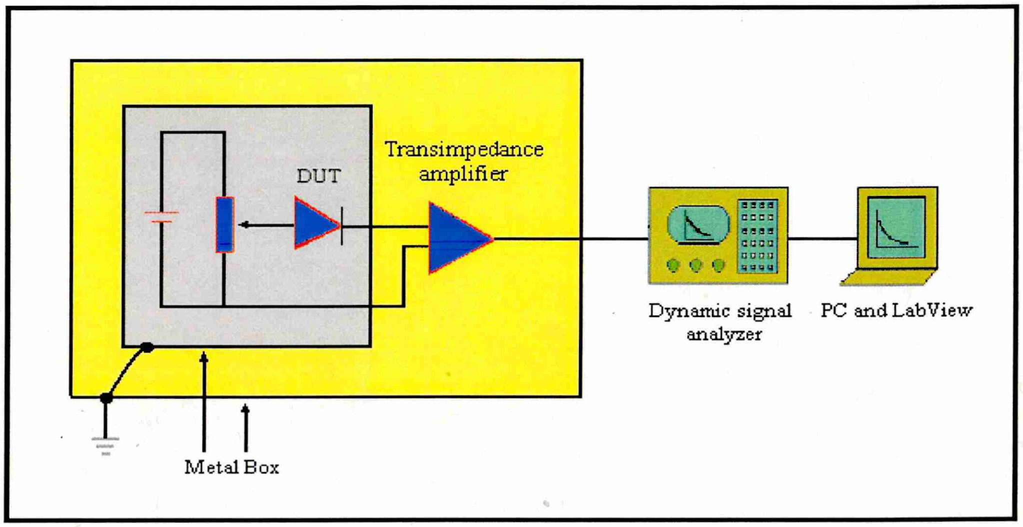

Figure 3.6. Schematic diagram of a low-frequency noise measurement set-up

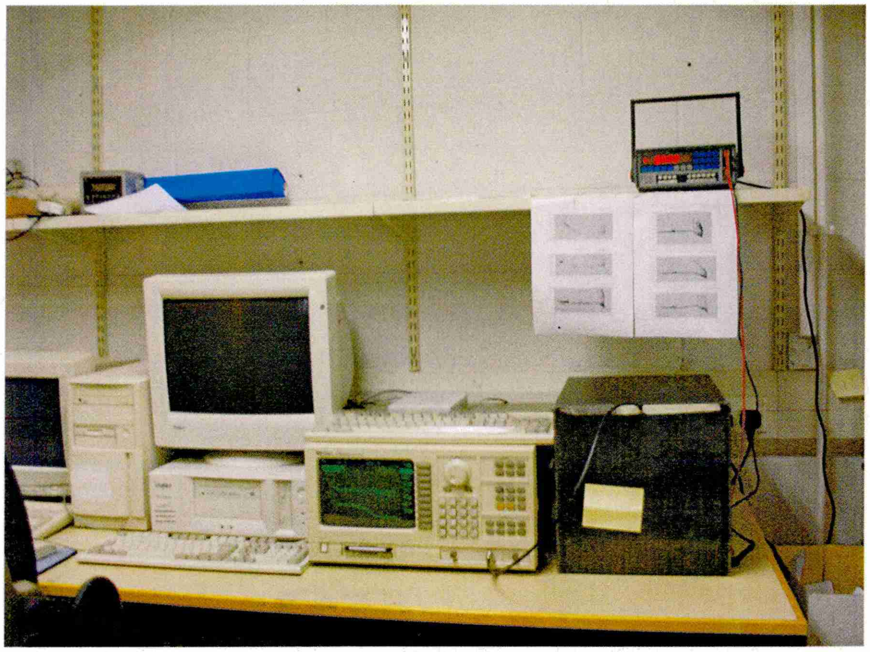

Figure 3.7. A photo of a LFNM set-up. The inner metal box and the trans-impedance amplifier were inside the black metal box.

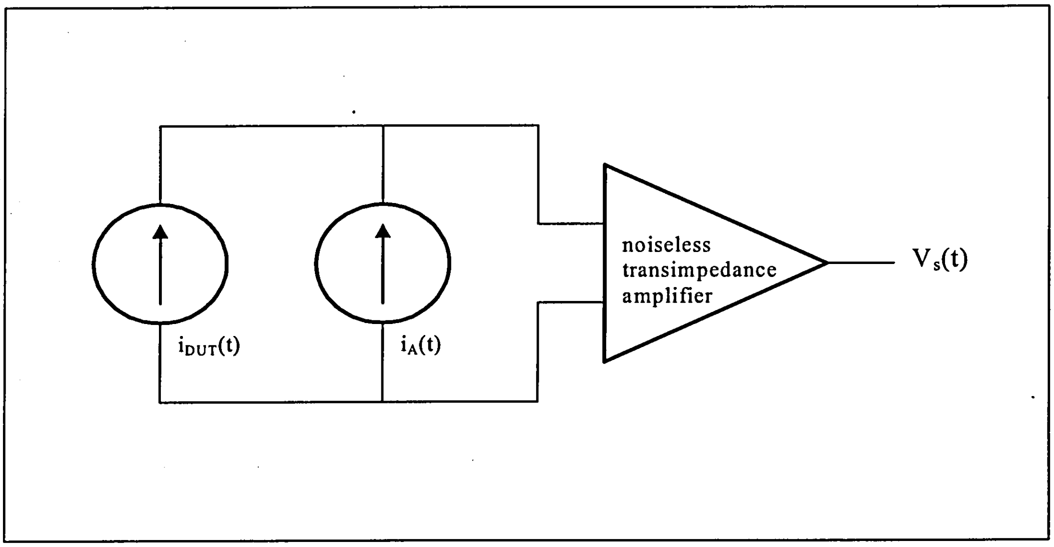

Figure 3.8 Noise equivalent model of the measurement set-up. $i_{DUT}(t)$ and $i_A(t)$ are the current noise equivalent generators of the device under test and of the amplifier respectively.

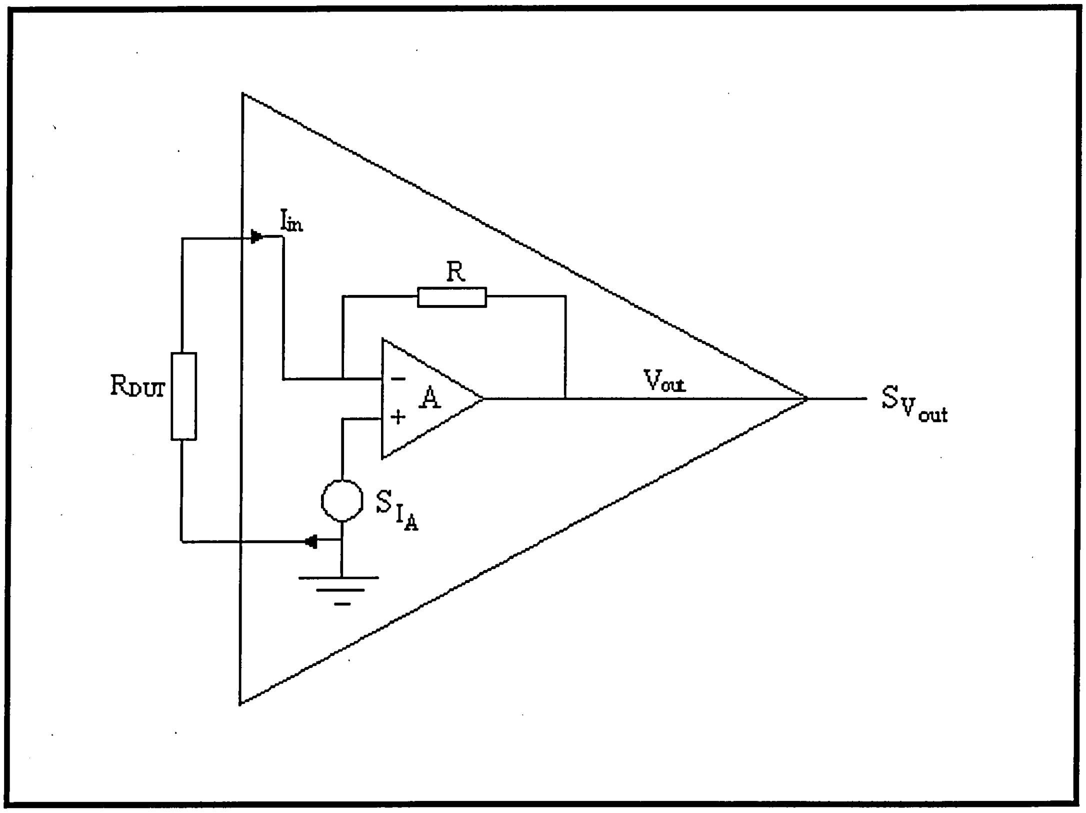

Figure 3.9. Schematic model of the transimpedance amplifier including the equivalent resistance of the device under test at the input (R_{DUT}).

The contribution of the background noise of the transimpedance amplifier was found to be negligible and was thus neglected. Typical data for background noise current spectral density and the maximum dc input current for each gain are shown in Table 3.1. From the transimpedance amplifier technical specifications, the noise floor of the amplifier was found to depend on its gain. Lowest noise floor $(\sim 10^{-28} A^2 / Hz)$ was achieved at the highest gain $(10^{-8} A/V\ LN)$ but at the expense of a decrease in the measurement bandwidth as shown in Figure 3.10.

Similar behaviour has been reported before [Blecher et al. 1998] using Ithaco model 564 current amplifier. Due to tail effect present in high gain sensitivity, the measurement bandwidth for a meaningful noise power spectral data, as in the present case, has been limited to 1 kHz. There is also some elevated $1/f$ noise contribution introduced by the transimpedance amplifier at lower frequencies which set a lower frequency limit to 1 Hz. Nevertheless, the reduced measurement bandwidth of less than 10 kHz and lower limit of 1 Hz (10 Hz for 10^{-5} A/V) was still applicable for this work.

The output of the solid-state power supplies is affected by high level of flicker noise which is produced by the Zener diode used as a reference [Ciofi and Neri 2000]. To avoid this problem, batteries were used for powering the DUT and the transimpedance amplifier. External noise is the most troublesome contribution to the failure in low level measurements and was thus eliminated. To protect the set-up from the surrounding electromagnetic interference (external noise), metal shielding with high-permittivity metallic material was used [Ciofi and Neri 2000]. Iron, aluminium, or Mumetal, are good candidates for effective shielding material. At Technical University of Eindhoven, of The Netherlands, a three-layer metal shielding box composed of Arco transformer steel, Mumental foil and Aluminum were used for shielding their low-frequency noise measurements [Staffan 1999].

Gain (A/V)	Max DC Input Current	Noise Current at 1 kHz	Input Impedance at 1 kHz
10^{-5}	9 mA	10 pA/√Hz	< 0.1 Ω
10^{-6}	900 μA	5 pA/√Hz	< 1 Ω
10^{-7}	9 μA	135 fA/√Hz	< 100 Ω
10^{-8}	900 nA	45 fA/√Hz	< 1 kΩ
10^{-8}, low noise	90 nA	15 fA/√Hz	< 10 kΩ

Table 3.1. Maximum dc current and noise current at each sensitivity.

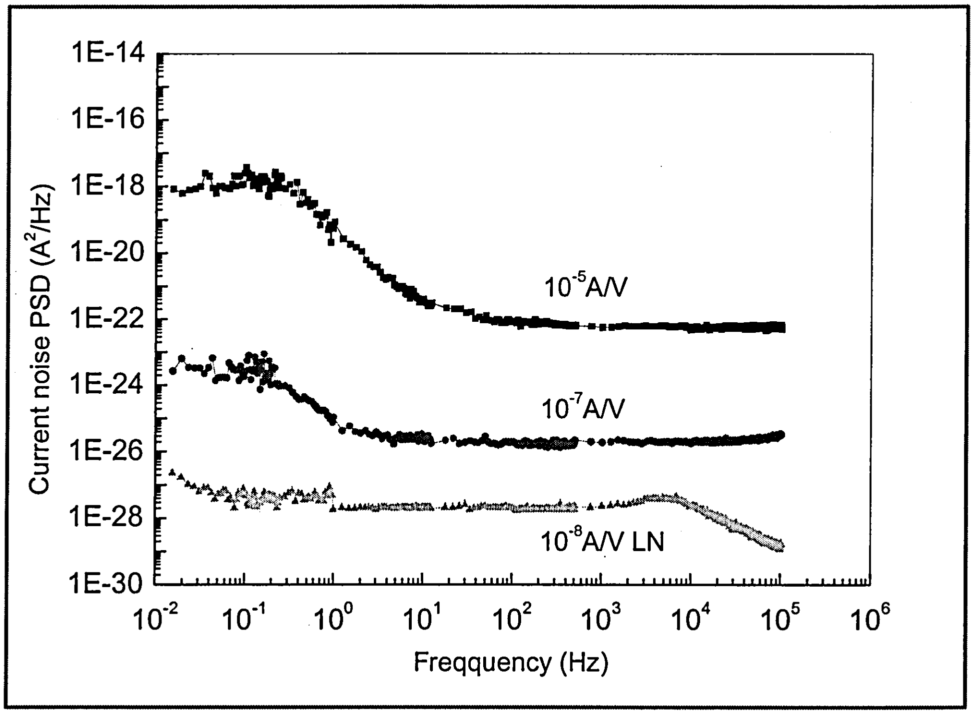

Figure 3.10. Current noise PSD of transimpedance amplifier with different gain setting.

However power-line interferences were still detected, but strongly suppressed. Blecher et al. have used an atom-bomb-proof shelter to reduce external interference from disturbing the measurements [Blecher et al. 1998]. As a rule of thumb, the test circuitry should be designed as compact as possible and placed in a small shielded box to avoid noise pickup from the power line since the pickup noise increases exponentially with increasing packaging size [Motchenbacher and Connelly 1993].

In this study, two metal boxes made from iron were used as shielding. The inner box was used to enclose the battery unit, and the printed circuit board (PCB) containing potentiometer and DUT. From practical experience, by using a PCB a less disturbing noise spectrum has been achieved. The circuit board layout with both top and bottom ground plates is shown in Figure 3.11.

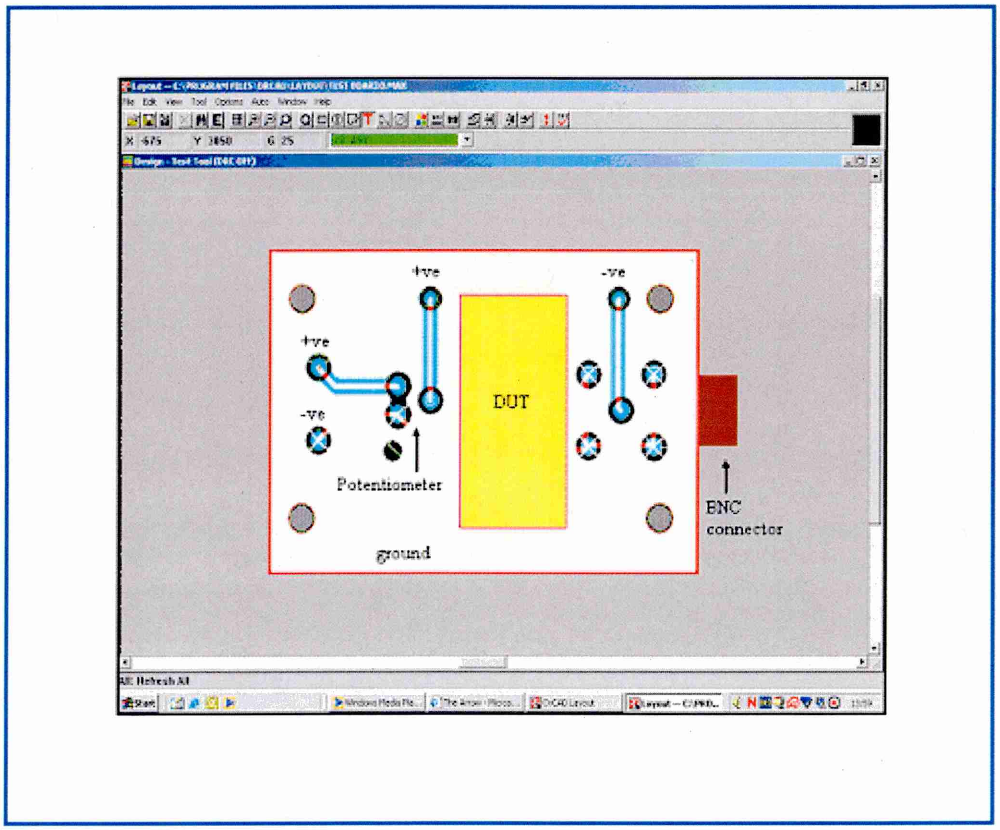

Figure 3.11. Printed circuit board layout.

The transimpedance amplifier and the inner box were then enclosed by the outer box. All electrical connections through the shielding box were made at one point for grounding purposes. By connecting both metal boxes to the mains earth [Necliudov et al. 2000], the 50Hz power line noise contribution has been minimized. On the other hand, power line interferences and its harmonics are easily detected as high peaks in the power spectra density at given frequencies and can easily be discarded from the measurement data.

The measurement set-up was placed in a basement room on a stable table to prevent mechanical vibrations from disturbing the measurement. No RF signal has been detected in this room even without shielding which means that high-frequency coupling effects can be neglected. Staffan (1999) has reported the detection of typical GSM time slots during unshielded measurements. As a rule of thumb, the shielding should be tight enough not to admit any light passing through, in order to prevent any high-frequency coupling through the shield [Stafan 1999]. Electromagnetic radiation from Cathode Ray Tube (CRT) from the PC monitor provides another source of low-frequency noise were reduced by moving the equipment away from the DUT.

Biasing of the DUT has been realized by using passive elements with low intrinsic noise. A wire-wound potentiometer was used as a voltage divider since it has the smallest inherent 1/f noise [Gunes et al. 2000; Van der Ziel 1976]. Double shielded low noise BNC (gold plated) cables were used to connect the device under test, transimpedance amplifier and the dynamic signal analyser. Since the input of the amplifier must be kept less prone to any external noise sources, the cable which connected DUT and transimpedance amplifier was made as short as possible.

The dynamic signal analyzer used was HP 35665A with built-in 12 bit A/D-converters. The dynamic range and average noise level are 72 dB and -110dBV respectively. It is a two-channel spectrum/network fast-fourier-transform (FFT) analyzer with a frequency range that extends from 244 μHz to 102.4 kHz in a single channel mode and from 122 μHz to 51.2 kHz in two channel mode. The FFT is based on the conversion of a time domain waveform to the frequency domain by sampling and digitising the signal of interest using an analogue to digital converter (ADC), and processed using the FFT algorithm by digital signal processing (DSP). Figure 3.12 shows the background noise of the dynamic signal analyser which is well below the background noise of the current amplifier.

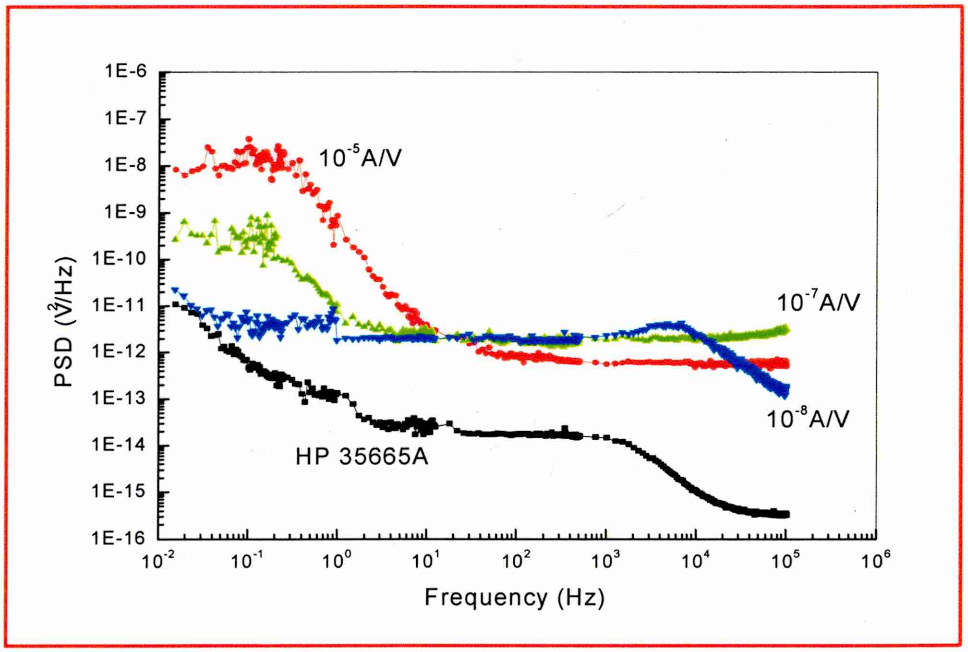

Figure 3.12 . Background voltage noise power spectral density of trans-impedance amplifier and dynamic signal analyzer.

Noise power spectra were measured with several forward dc bias currents in the low to moderate range, from 20nA to 100uA, as well as with no bias current in the frequency range 1 Hz to 100 kHz. With no bias current the DUT is under thermal equilibrium condition and the noise power spectrum obtained is the system background noise which consists of Johnson noise of the DUT and amplifier noise. However the noise added by the amplifier is sufficiently low and thus, does not affect the measurements.

A custom-made program was developed within the LabView software environment for acquiring the noise power spectral density data from the dynamic signal analyser via the HPIB bus by a personal computer. Figure 3.13 shows the LabView window panel, and the diagrams used to acquire the low-frequency noise PSD data are shown in Figure 3.14.

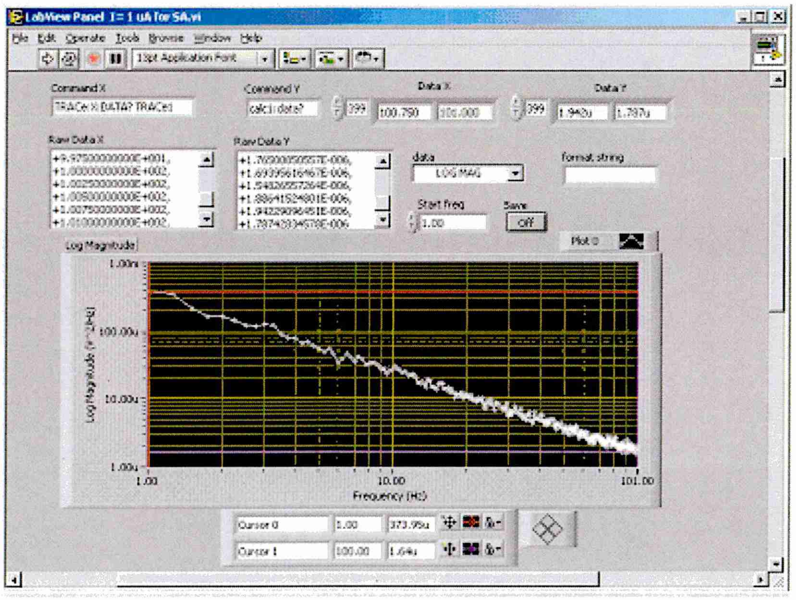

Command X: TRACe:X:DATA? TRACe1

Command Y: calc1:data?

Data X: 399 100.750 101.000

Data Y: 399 1.942u 1.787u

Raw Data X:
+9.97500000000E+001,
+1.00000000000E+002,
+1.00250000000E+002,
+1.00500000000E+002,
+1.00750000000E+002,
+1.01000000000E+002,

data: LOG MAG

format string:

Start freq: 1.00

Save: Off

Cursor 0 1.00 373.95u

Cursor 1 100.00 1.64u

Figure 3.13. LabView panel window for acquiring PSDs data.

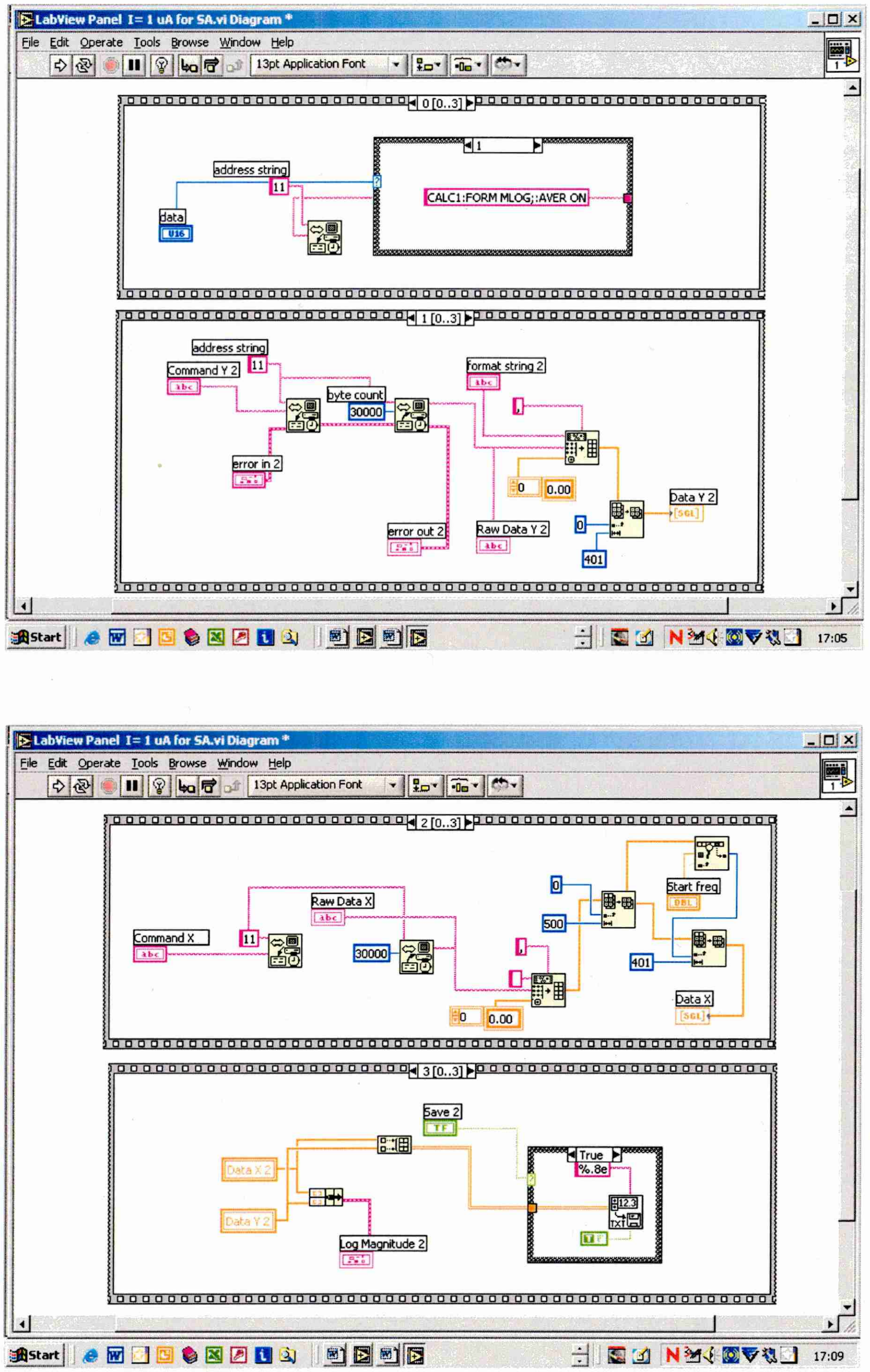

Figure 3.14. LabView program diagrams windows for acquiring PSDs data.

3.4.2 Averaging and Windowing

As noise is random in nature, a power spectral density based on a single measured time sequence will never give the expected spectral behaviour. This points out to the need of averaging the signal. This type of measurement picks out periodic frequency components and removes noise that is not correlated to the repeated signal. Figure 3.15 illustrates the effect of averaging in measuring the transimpedance amplifier noise power spectral density. In this work, averaging by 100 times in rms mode is found sufficient in order to obtained a meaningful result. The only disadvantage of averaging which cannot be avoided is the long time needed for the averaging of the PSDs, especially in the frequency range lower than 1 Hz, due to large amount of data to handle.

The other important and critical aspect when dealing with Fast Fourier Transform (FFT)-based dynamic signal analyzer is windowing. A window is a filter which was found useful in reducing signals that are not periodic within the input time record when using the FFT for spectral analysis. Depending on the type of window used, the analyzer attenuates different parts of the input time record to prevent leakage, that is the smearing of energy across the frequency spectrum, which is caused by transforming signals that are not periodic within the time record. The Hanning window was used in these measurements as with any other low-frequency noise measurements, since it is the most suitable window for narrow-band random signals (vibration data) [NI application note 041].

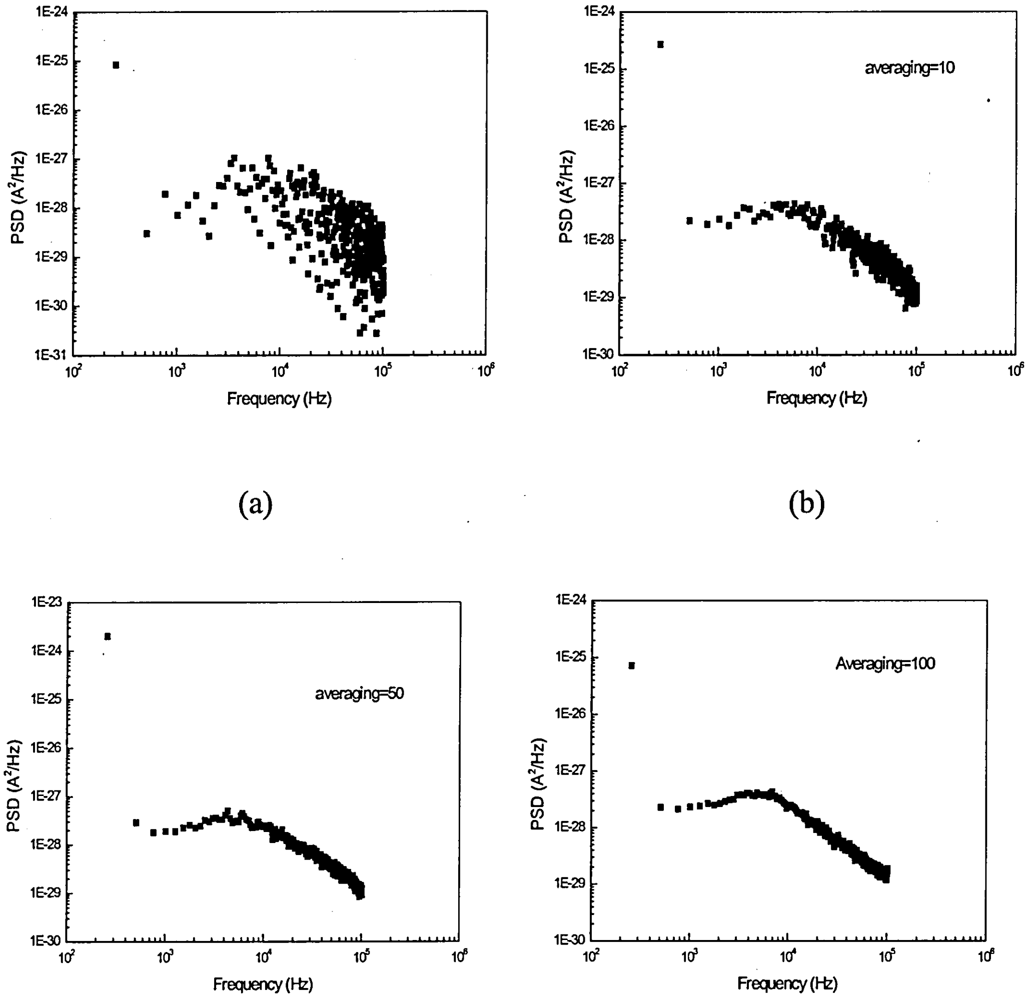

(a)

(b)

(c)

(d)

Figure 3.15. The effects of averaging on the PSDs data.
(a) Without any averaging
(b) 10 times averaging
(c) 50 times averaging
(d) 100 times averaging

3.4.3 Wide-band measurements

Noise signal has its energy present over a frequency band significantly wider than the spectrum analyser's resolution bandwidth. This means, measurements over several frequency sub-bands are necessary. This is because the commercial FFT signal analyzers have small sampling number either 400 or 800 points. For HP 35665A dynamic signal analyser, it has only 400 points which produce high error in low frequency range of a broadband measurement.

If only one frequency band is chosen for the whole measurement, approximately 90% of the frequency points will be found in the higher decade of the band leaving approximately 10% in the lower decade. This extreme variation of the points will not present the true spectral density of the noise in the devices as shown in Figure 3.16 (a). As can be seen, the majority of the points are in the highest decade, that is in the 10 kHz to 100 kHz range. The highest error of the measurement occurs in frequencies less than 1 kHz. To overcome this problem, 3 frequency sub-bands, each in two-decades of frequencies, have been chosen in order to get a meaningful result from the measurements. The frequency sub-bands used were 1 Hz to 101Hz, 100 Hz to 13 kHz, and 1 kHz to 103 kHz. The total PSD spectrum was then constructed from the PSDs of the different sub-band as shown in Figure 3.16 (b).

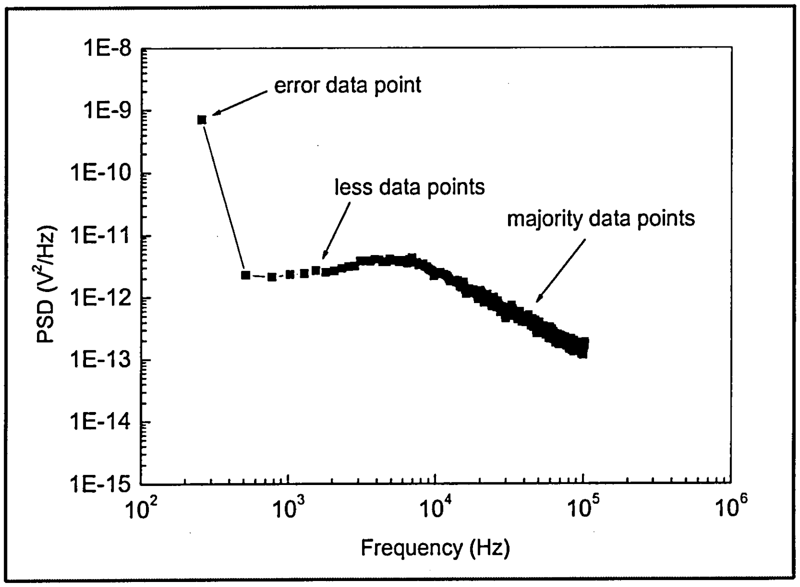

(a)

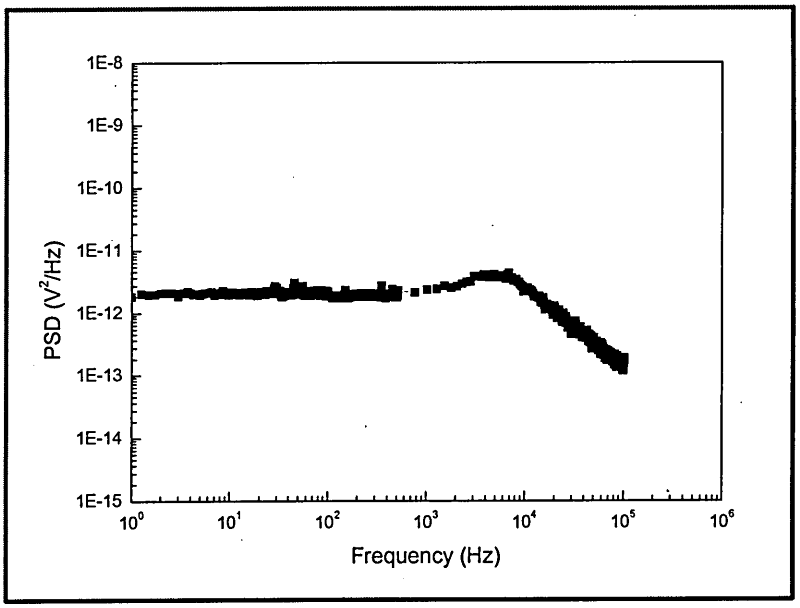

(b)

Figure 3.16. Wide-frequency measurement with (a) one and (b) three frequency bands

3.4.4 Validation of the System Performance

One of the requirements of any experimental measurement is to verify that the system set-up has been validated before performing any measurement. It becomes more critical when dealing with low-level signals. For low-frequency noise measurement, the validation needs to be performed in order to ensure that the experimental set-up measures the correct value of the device noise spectral density. This is not an easy task, but since the transimpedance amplifier and the potentiometer that we used have a very low level of current noise, the validation has been a straightforward matter.

The simplest method of performing system validation is by measuring the known value of noise sources. Using this approach, the validation of the experimental set-up, has been done by measuring the Johnson noise spectral density, of $10M\Omega$ and $5M\Omega$ resistors. The Johnson noise of a resistor can be calculated by using $S_I = 4kT/R$ and are found to be $1.65\times10^{-27} A^2/Hz$ and $3.31\times10^{-27} A^2/Hz$ for $10M\Omega$ and $5M\Omega$ respectively. In figure 3.17 we have observed that the noise power spectral density measured with the sensitivity of $10^{-8} A/V$ (low noise) is within the same order of magnitude of the theoretically calculated one. Similar noise spectral density for $10M\Omega$ resistor has been reported previously by Lambert et al. [Lambert et al. 2001]. Once it had been validated, the LFNM measurement set-up was ready for measurement.

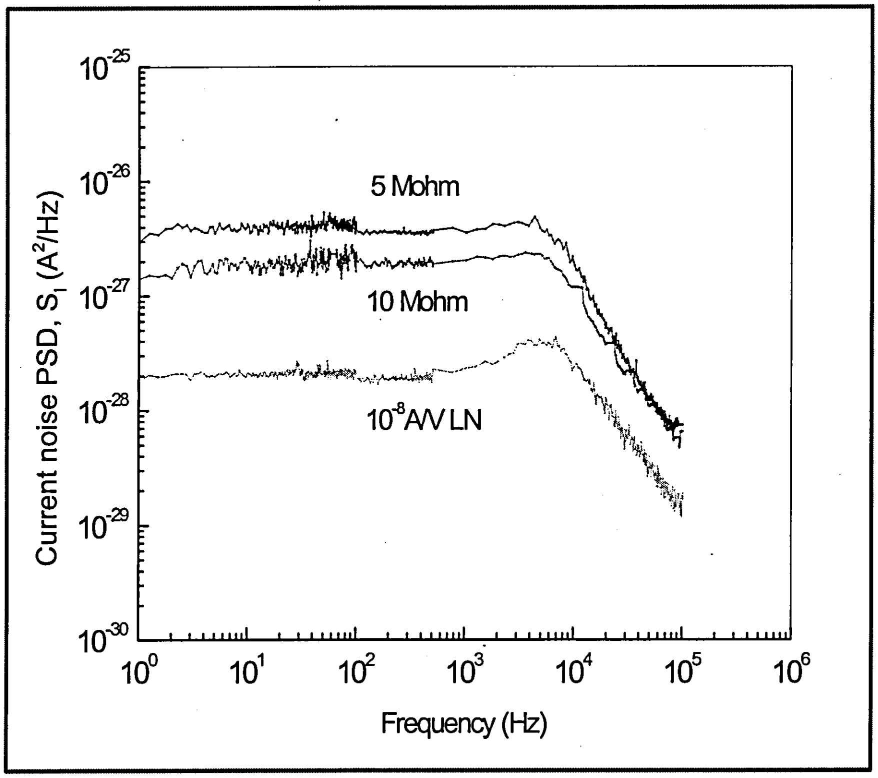

Figure 3.17 Validation of the measurement set-up.

CHAPTER 4

Admittance Spectroscopy: Results and Discussion

4.1 Introduction

The electrical admittance, (or impedance) spectroscopy is one of the most important nondestructive methods for obtaining information in the bulk and on the interfacial regions between semiconductor and dielectric medium of any kind of solid or liquid material. By applying an electrical field perpendicular to the surface (known as field effect), the occupancy of surface states in semiconductors can be varied which in turn will change the physical quantities of the devices i.e. capacitance and conductance.

Admittance measurements comprise the study of the capacitance and conductance of LB films of stearic acid (before and after treatment with H_2S gas) in metal-insulator-semiconductor (MIS) structure as a function of applied voltage (CGV) and frequency (CGF). Measurements were performed in the dark at room temperature and under vacuum in a cryostat with temperature range between 80K and 380K. Section 4.2 will present the result obtained from capacitance-voltage measurement whilst section 4.3 will discuss the dielectric behaviour of the LB films with and without the inclusion of CdS nanoparticles.

The main objective of this study is to investigate the effects of incorporating CdS nanoparticles in the stearic acid matrix (nanocomposite films) on the capacitance and conductance of the device.

4.2 Capacitance-Voltage (C-V) measurements

Capacitance-voltage (C-V) characteristics of MIS devices formed with the as-deposited 40-layer LB films of stearic acid (SA and SA+CdS) were investigated with varying modulating signal frequency and biasing voltage. A small a.c. signal of $20\text{mV}_{\text{r.m.s}}$ was applied across the sample while a d.c. electric bias was swept from -3V to $+3\text{V}$ i.e. from reverse to forward bias. Figure 4.1 depicts the C-V characteristics of the untreated device (SA) for three different modulating signal frequencies. As can be seen from the graph, the observed behaviours were different from those obtained for ideal MIS devices. The capacitance of the untreated device was found to be highly dependent on the a.c. modulating frequency. For a.c. signal frequency up to 100 kHz, a typical C-V behaviour of MIS structure showing three distinct regions: inversion, depletion and accumulation were observed when the biasing voltage was swept from -3V to up to approximately $0.8\,\text{V}$.

When a signal frequency is greater than $100\,\text{kHz}$, a drastic drop in capacitance occurred. The dip in the curve for SA at $V \geq 0.8\text{V}$ may be due to high leakage dc current flowing through the device in the accumulation region. As the frequency increased, the capacitance in the accumulation region decreased more than in the inversion region. Similar decrease of capacitance with frequency in accumulation region of a MIS capacitor formed by thermally evaporated stearic acid $(\text{thickness}\,120\,\text{nm})$ on p-silicon substrates with thin native silicon dioxide (SiO_2) was reported earlier [Alam 1991].

The decrease of capacitance with increasing frequency is called anomalous frequency dispersion. This type of behaviour is generally caused by the creation of higher density of surface states at the interface between insulator and semiconductor [Houston et al. 1997; Kochowski et al. 2000]. Also, frequency dispersion might arise from the series resistance from low substrate doping [Ramanathan et al. 2002]. Typical MIS behaviour was not observed at higher modulating frequency $(1\,\mathrm{MHz})$. A similar feature at $1\,\mathrm{MHz}$ was reported earlier in MIS capacitors on different substrate such as GaAs [Meiners 1978; Kohn and Hartnagel 1977], GaSb [Houston et al. 1997], Si [Kwa et al. 2003]. This showed that interface traps were no longer able to follow the probing a.c. signal in the high-frequency regime. The flattened C-V curve could also be due to the presence of a series resistance R_S due to the contacts and the substrate and this parameter was known to be significant in the high frequency regime.

A different behaviour was observed for treated devices. Figure 4.2 depicts the variation of capacitance C of Al/SA+CdS/Si/Al devices as a function of applied voltage V for three modulating frequencies (as for SA) of $50\,\mathrm{kHz}, 100\,\mathrm{kHz}$ and $1\,\mathrm{MHz}$. The capacitance showed smaller dependence on the a.c. signal frequency than untreated samples. An improvement was also achieved in the C-V behaviour. Measured C-V characteristics were, however, not ideal as expected of MIS capacitor of SiO_x [Sze 1981] but depletion and accumulation regions were found to be well-defined for all modulating frequencies.

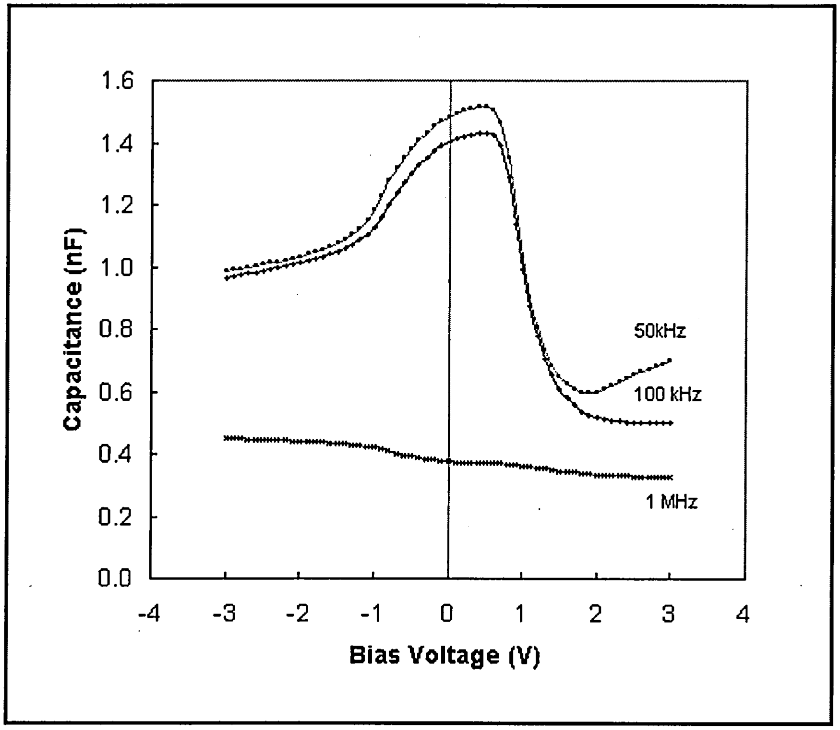

Figure 4.1: Capacitance versus voltage (C-V) characteristics of untreated devices at different frequencies.

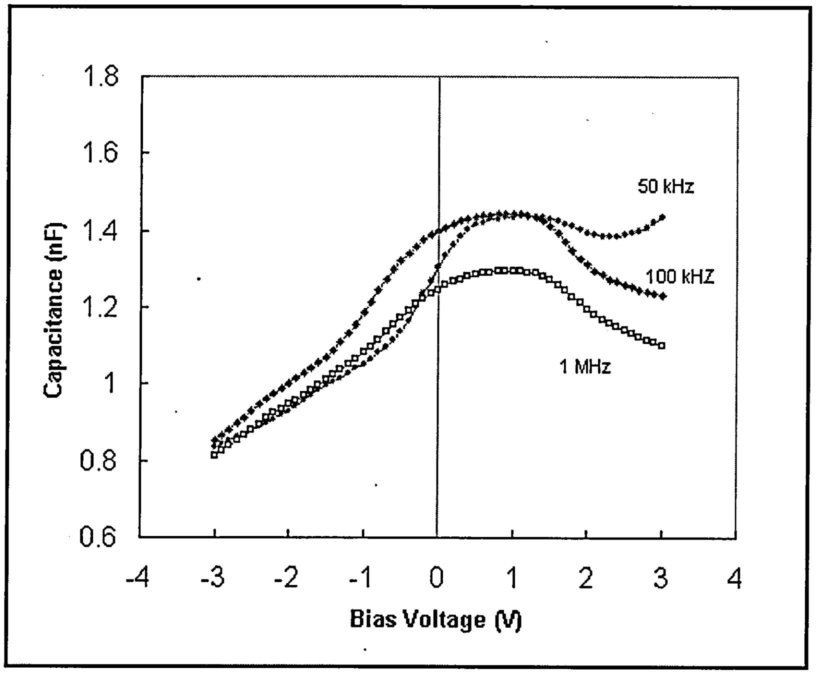

Figure 4.2: Capacitance versus voltage (C-V) characteristics of treated devices at different frequencies.

The presence of an inversion layer was not obvious and it was believed to occur at higher reverse voltage. Further decrease of the capacitance with increasing reverse bias voltage indicated that the space-charge layer was driven far into the inversion-layer regime without the production of any inversion-layer charge [Singh and Hartnagel 1975]. Similar C-V behaviour ($f = 500\,\text{kHz and}\,1\text{MHz}$) at room temperature was observed for MIS structure containing RF magnetron sputtered diamond-like carbon (DLC) films [Logothetidis et al. 1997]. The leakage current was reported to be very small, in order of $10^{-11}\,\text{A}$. DLC films was regarded as being composite material, consisting of amorphous diamond, graphite, and voids. The absence of inversion layer in the C-V characteristics was not well-understood.

In the present study, the capacitance of the LB films of stearic acid in the accumulation region became less dependent on the modulating signal frequency when CdS nanoparticles were embedded in the stearic acid matrix. The effect was attributed to the reduction in the dc leakage current as reported in section 4.2. As the biasing voltage increased, the device capacitance reached maximum value in the accumulation region and maintained it up to approximately $1.8\,\text{V}$. When the bias voltage exceeded this value the capacitance started to drop. The relaxation mechanism of the carriers was believed to be responsible for the dip in the curve for SA+CdS at $V \geq 1.8\,\text{V}$.

The method presented by Yang and Hu (see section 2.2.3) for MOS capacitor with thin SiO_2 dielectric and large dc leakage current [Yang and Hu 1999] was employed in order to determine the true insulator capacitance in our organic LB films. This modelling technique was found to be suitable for the frequency dispersion of C-V measurements in the accumulation region of MOS devices and has been explained by others [Lay et al. 2001; Clerc et al. 2001; Shriram et al. 2002; Chim et al. 2003; Zhu and

Liu 2003; Xu-bing et al. 2003]. Also, this technique has been recommended by Agilent (formally known as HP) in measuring a true oxide capacitance in MOS devices with high leakage current. Since the dielectric constant of SiO_2 is a well known value, the equivalent oxide thickness (EOT) was deduced from the obtained true capacitance value. In this study, since the thickness was already known, the technique was applied in order to determine the dielectric constant of the LB films.

The frequency-independent insulator (LB films) capacitance C_{LB} was determined from the measured values C_1 and C_2 of capacitance at two different frequencies f_1 and f_2, respectively is given by

$$C_{LB} = \frac{f_1^2 C_1\left(1+D_1^2\right) - f_2^2 C_2\left(1+D_2^2\right)}{f_1^2 - f_2^2} \tag{4.1}$$

where D_1 and D_2 are the dissipation factors at f_1 and f_2. Dissipation factor is related to quality factor as $Q = 1/D$.

Two sets of capacitance (C) and conductance (G) data at two different frequencies were chosen. We found that, for composite SA (untreated), data at $f_1 = 50\text{kHz}$ and $f_2 = 1\text{MHz}$, and $f_1 = 100\text{kHz}$ and $f_2 = 1\text{MHz}$ were suitable for the fitting. For SA+CdS (treated) the two set frequencies were $f_1 = 1\text{kHz}$ and $f_2 = 1\text{MHz}$, and $f_1 = 50\text{kHz}$ and $f_2 = 1\text{MHz}$.

Figure 4.3 shows the simulated capacitance as a function of bias voltage. As it can be seen from the graph, both set of frequencies chosen for calculating the true insulator capacitance were consistent with each other and frequency-independent. Also the treated devices have larger value of capacitances and better C-V characteristics as compared to the untreated one. Due to flattened capacitance at frequency of 1 MHz, the simulated capacitances for untreated device did not clearly show the MIS behaviour as compared to the treated one. Nevertheless we can still observe the flat accumulation region which is in the regime of our interest.

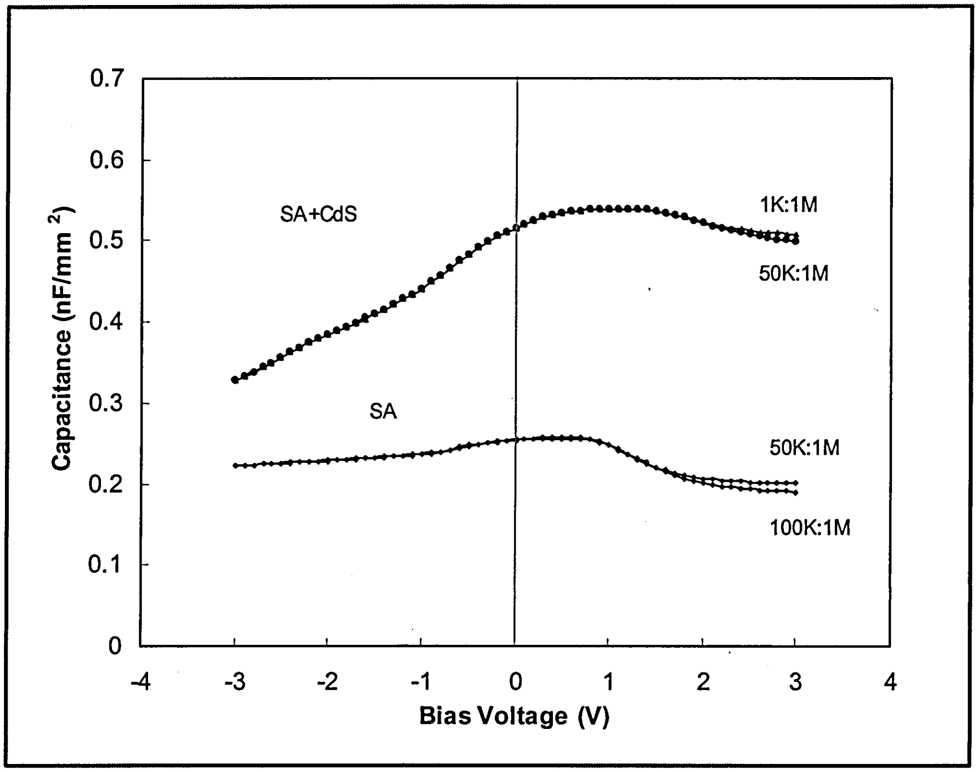

Figure 4.3: Simulated C-V characteristics obtained by using Yang's technique.

The flat accumulation capacitances taken from the graph in Figure 4.3 were 1.35nF and 0.9nF for treated and untreated devices respectively. The true insulator capacitance was determined when the device was biased in the accumulation region. Taking into consideration the parallel SiO_2 capacitance, the SiO_2 capacitance was estimated to be 0.22nF for treated and 0.17nF for untreated device. By subtracting the SiO_2 capacitance, the true capacitance value of LB films was found to be 1.13nF for treated and 0.73nF for untreated devices. The corresponding effective dielectric constant (ε_r) is estimated to be 2.3 and 5.1 for the SA film and LB films containing nanoparticles respectively.

Values of dielectric constants of Cd salt in stearic acid films ($CdSt_2$) were reported by several group of researchers. In 1939, Race and Reynolds [Race & Reynolds 1939] determined a value of $\varepsilon_r = 2.59 \pm 0.03$ for $CdSt_2$. Mann and Kuhn [Mann & Kuhn 1971] have reported a value of 2.71 ± 0.17 for monolayers of Cd salt in stearic acid films (n=18). Later, Roberts et al. reported a value of 2.52 obtained from reciprocal of capacitance $(1/C)$ at 1 kHz versus number of $CdSt_2$ layer (N) [Roberts et al. 1978]. A similar value of dielectric constant to Mann and Kuhn has been reported by Sugi et al. [Sugi 1979], $\varepsilon_r = 2.77 \pm 0.07$ for multilayer cadmium stearate (n=18) determined by a.c. measurement at $f = 10^{-3}$ Hz.

The dielectric constant found in this study (by C-V measurement) is lower than the above reported values which were extracted from the a.c measurements. According to Mann and Kuhn the capacitance in every measurement is dependent on the nature and concentration of the electrolyte used [Mann & Kuhn 1971]. On the other hand, since we obtained our dielectric constant based on a mathematical equation, $\varepsilon_r = Cd/\varepsilon_0 A$, certainly there were errors in measuring the device effective area A (length x width). We also believed that, there was also error in calculating the parallel SiO_2 layer capacitance, again due to the measured area which was involved in the calculation. However, if we assume 2.7 as the true dielectric constant for $CdSt_2$, then the error is about 15%, which is still acceptable in experimental works.

Once the value for the dielectric constant was found, the analysis was extended to determine the flat-band capacitance (C_{FB}) and the corresponding flat-band voltage (V_{FB}). By knowing these values the threshold voltage V_T and the surface charge density (N_{ss}) can be determined. The flat band capacitance is written in terms of the dielectric constants ε_s of the semiconductor substrate and ε_i of the insulating film, respectively [Sze 1981]:

$$C_{FB} = \frac{C_i}{1 + \frac{\varepsilon_i}{\varepsilon_S} \frac{L_D}{d_i}} \tag{4.2}$$

where C_i and d_i are the capacitance (before subtracting the SiO_2 capacitance) and the thickness of the LB film respectively. L_D is the Debye length and can be determined from the electron mobility μ_n as [Sze 1981]

$$L_D = \sqrt{\frac{kT\varepsilon_o\varepsilon_s\mu_n\rho}{q}} \tag{4.3}$$

Substituting a typical value of electron mobility $\mu_n = 1387\ \mathrm{cm^2V^{-1}s^{-1}}$ for a $\rho=4.5\Omega\mathrm{cm}$ n-type silicon substrate, $q = 1.6\times10^{-19}\,\mathrm{C}$, $\varepsilon_o = 8.85\times10^{-12}\,\mathrm{Fm^{-1}}$ is the permittivity of the free space, T is taken to be $300\mathrm{K}$, and the Boltzmann's constant $k = 8.625\times10^{-5}\,\mathrm{eVK^{-1}}$, into equation 4.3, L_D is estimated to be $0.13\mu\mathrm{m}$. A value of $0.73\mathrm{nF}$ (or 0.86nF before subtracting) and 0.58nF (or 0.72nF before subtracting) is estimated for the flat-band capacitance C_{FB} of the silicon/SA+CdS (treated) and silicon/SA (untreated) devices by using Equation 4.2. The corresponding flat-band voltage V_{FB} is, therefore, found from the graphs in Figure 4.3 to be $-2.1\mathrm{V}$ for the SA+CdS composite film and $-2.9\mathrm{V}$ for SA. It is well known that flat band voltage V_{FB} depends on the interface state density as well as the trap charge [Lee et al. 1994]. The shift of flat-band voltage along the negative voltage axis implies an increase in the positive fixed charge trapped at the insulator-silicon interface [Szė 1981]. A value of $5.0\times10^{11}\,\mathrm{cm}^{-2}$ for the surface charge density (N_{SS}) of the effective charge in the composite insulating materials was estimated from the value of the flat-band voltage V_{FB} by using the equation:

$$V_{FB} = \phi_{ms} - \frac{qN_{ss}A}{C_i} \tag{4.4}$$

where $\phi_{ms} = -0.33\,\mathrm{eV}$ is the difference in work functions of the aluminum electrode and silicon wafer. A lower N_{ss} value was found for SA which is $3.3\times10^{11}\,\mathrm{cm}^{-2}$. This is very plausible since CdS particles are likely to introduce additional ions in the SA matrix. The threshold voltage V_T is generally related to V_{FB} in the form [Sze 1981]:

$$V_T \cong \frac{A\sqrt{(4\varepsilon_0\varepsilon_s\varphi_B)/(\mu_n\rho)}}{C_i} + 2\varphi_B + V_{FB} \tag{4.5}$$

where the bulk potential φ_B of the silicon substrate is estimated to be $0.278\,\mathrm{V}$ from the equation:

$$\varphi_B = -\frac{kT}{q}\ln(q\mu_n\rho n_i) \tag{4.6}$$

It is found that the MIS containing the SA+CdS nanocomposite will turn on at $-1.24\,\mathrm{V}$ whilst at a lower value, $V_T = -1.64\,\mathrm{V}$, for MIS devices of untreated films. Table 4.1 lists all the parameters calculated in this section for both devices for ease of comparison. It was observed that by embedding the CdS nanoparticles into the stearic acid matrix, the ac properties of the film have changed.

LB films	C_i (nF)	ε_r	C_{FB} (nF)	V_{FB} (V)	V_{TH} (V)	N_{SS} x 10^{11} cm^{-2}
Untreated (SA)	0.73	2.3	0.58	-2.9	-1.64	3.3
Treated (SA+CdS)	1.13	5.1	0.73	-2.1	-1.24	5.0

Table 4.1. Parameters derived from C-V measurement.

4.3 Admittance measurements

The admittance (Y) of the treated (SA+CdS) and untreated (SA) devices were measured as a function of frequency by applying a sinusoidal voltage signal and monitoring the amplitude and phase shift of the resulting current. As a result the data obtained from these measurements are complex presentation, the real (Y') and imaginary parts (Y") of the admittance; $(Y = Y' - jY'')$.

The frequency was swept from 20Hz to 1MHz in a logarithmic scale. The measurements were performed in the dark at room temperature and also in a cryostat under vacuum better than 10^{-5} torr for temperature in the range of 80K to 380K. The amplitude of the a.c. signal voltage was $20mV_{rms}$ with d.c. bias voltage set to zero. Since d.c bias voltage $V = 0V$, the effect of d.c. leakage current on capacitance as observed previously in C-V measurements was ignored.

4.3.1 Dielectric loss: Room temperature

Figure 4.4 shows the variation of capacitance (C) and the frequency normalized conductance (G/ω) of LB film of stearic acid (SA and SA+CdS) measured at room temperature. In order to compare their results, both C and G/ω are normalized to device area, A. As previously observed in C-V measurements, by embedding the LB film of stearic acid with CdS nanoparticles, the device capacitance increased. Also the capacitance for LB film of stearic acid with Cd^{2+} (SA) showed almost no frequency dependence. This was similar to the result of LB films of cadmium arachidate measured at room temperature [Roberts et al. 1980]. No significant dispersion of capacitance was observed at frequency below approximately $80\,\mathrm{kHz}$.

On the contrary, the sample containing CdS nanoparticles exhibited strong frequency dependencies at frequency greater than $100\,\mathrm{kHz}$. Below this, the capacitance was less dependent on the signal frequency which is similar in behaviour to SA. For SA+CdS the capacitance went from a high value, at low frequency plateau (C_s), to low value at high frequency. Since the maximum sweep frequency of the HP 4284A LCR meter was only 1 MHz, the high frequency plateau in capacitance (C_∞) was not observed. It was found that by embedding CdS nanoparticles in stearic acid matrix, the capacitance of LB films increased primarily due to the increase in dielectric constant as seen previously by C-V measurement.

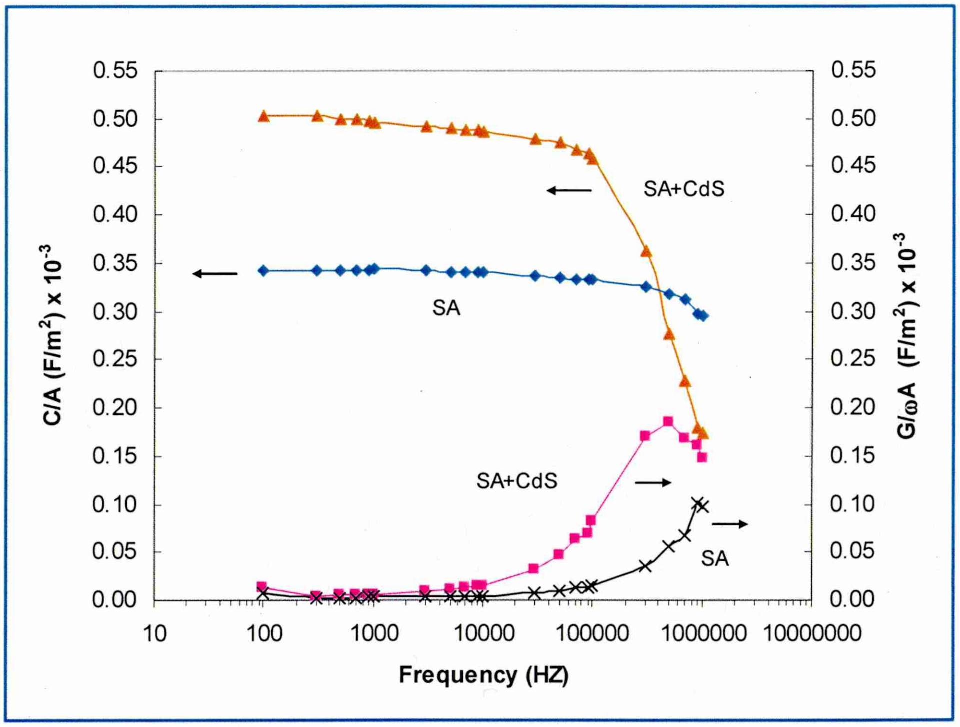

Figure 4.4. Capacitance per unit area versus modulating frequency for treated and untreated devices.

The variation in the capacitance of the device as a function of modulating signal frequency was due to the polarization of the dielectric medium in which positive and negative charges were displaced with respect to their equilibrium positions [Kasap 1997]. From the graph, the normalized conductance $(G/\omega A)$ of the treated device shows a peak at $500\,\text{kHz}$. No peak was observed for untreated devices within the range of investigation. The relaxation time (τ) due to the induced dipole moments for treated devices was estimated to be $2\,\mu\text{S}$ whilst untreated devices are believed to have smaller relaxation time. The increase in relaxation time was believed to be due to the increase in dielectric constant of the LB films when CdS nanoparticles were embedded in the strearic acid matrix.

The electrical conductivity of many different dielectric materials was known to depend on the modulating signal frequency. Jonscher has observed a similar pattern of a.c.

conductivity behaviour of different dielectric on modulating signal frequency and later proposed a universal dielectric response model which is represented by $\sigma(\omega) \propto \omega^n$, where $n \leq 1$ [Jonscher 1977]. Figure 4.5 shows the conductivity of the devices (SA and SA+CdS) as a function of frequency at room temperature. In contrast to the capacitance, the conductance for both devices have shown a different behaviour; increasing with the modulating frequency. For low signal frequency (below 1 kHz), the universal law is followed with the exponential constant $n \sim 0.8$.

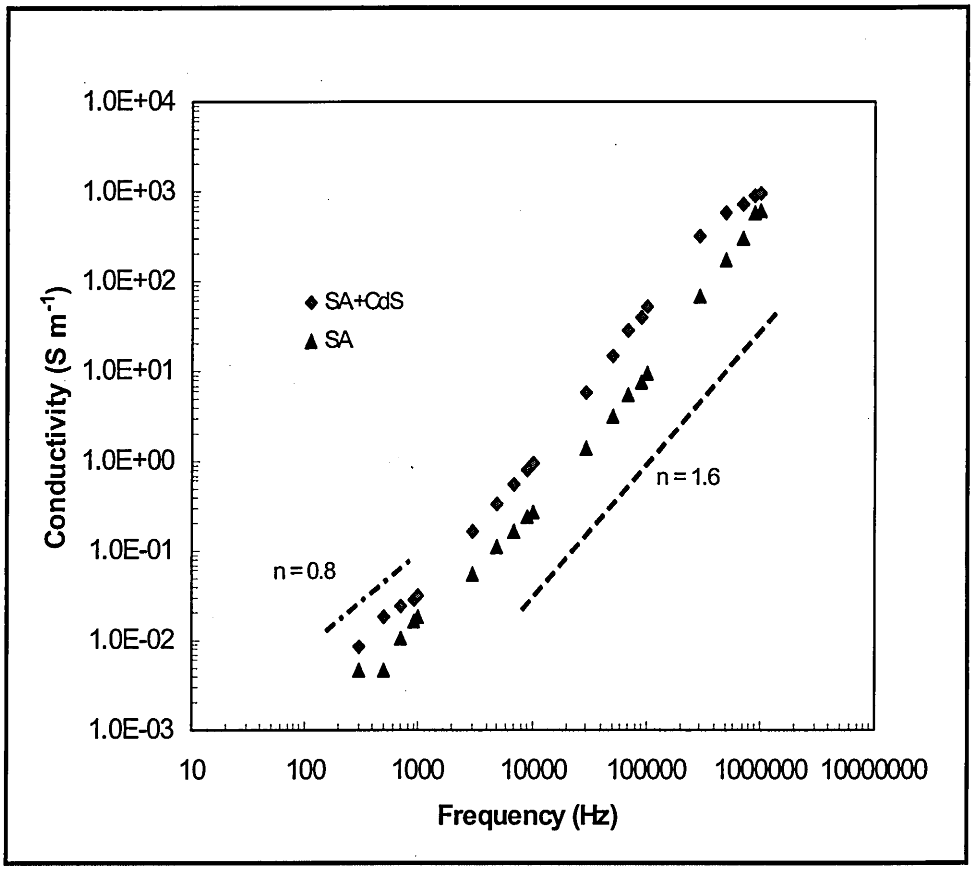

Figure 4.5. AC conductivity versus modulating frequency for treated and untreated devices.

This type of dependence agrees well with the prediction model describing hopping transport mechanism [Petty et al. 2000]. Deviation from Jonscher's universal law was seen for signal frequency greater than 1 kHz. For frequencies up to 100kHz the exponential constant was found to be greater than unity with $n \sim 1.6$. Since the n value is close to 2, it suggests that this was due to the dominance of series resistance (R_S) which is associated with the neutral region of the semiconductor between the depletion region and bottom contact [Rhoderick 1978] and also from the electrode contacts. As conductance $(G = 1/R)$ of a device is a representation of losses in the material, it shows that power losses in both devices are highly dependence on the signal frequency.

Figure 4.6 shows the dissipation factor, also known as dielectric loss $(\tan\delta)$ of treated and untreated devices as a function of modulating signal frequency measured in the dark at room temperature. As can be seen, the dielectric loss is highly dependent on the modulating signal frequency. A minimum in $\tan\delta$ is apparent over the frequency range investigated with a narrow-band curve. The dielectric loss decreases with increases in frequency till the loss minimum $(\tan\delta_{\min})$ is observed and thereafter, $\tan\delta$ increases linearly with frequency $(\tan\delta \propto f)$. These results agree well with a model by Goswami and Goswami [Goswami and Goswami 1973] which explain the variation of $\tan\delta$ with frequency and the appearance of $\tan\delta_{\min}$ in the audio range frequency. The resulting curve is similar to the band-pass filter response of a varactor diode [Sze 1981] which, suggests that the LB film of stearic acid cannot be modelled by a simple film resistance R_{LB} and capacitance C_{LB} in parallel with each other. The electrodes are assumed to contribute a resistance R_S in series with the sample as modelled by a three-element model reported earlier in C-V measurements section.

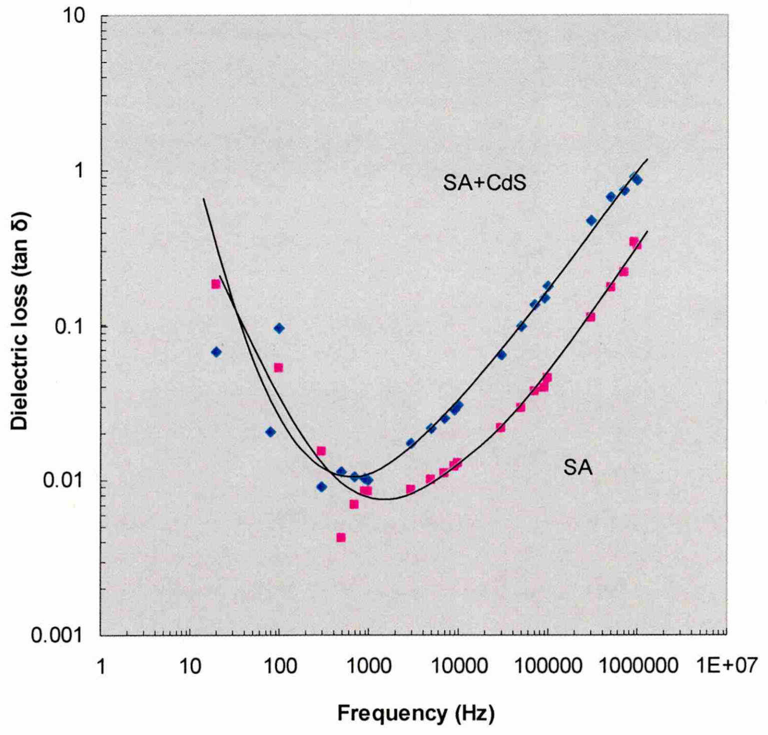

Figure 4.6. Dielectric loss as a function of modulating frequency for treated and untreated devices measured at room temperature.

Also as can be seen from the graph, the treated device has slightly larger dielectric loss when compared to the untreated one. This could be due to CdS nanoparticles formed in the stearic acid matrix which are believed to act as carrier traps. This comparison is in agreement with the finding of lower leakage current in treated devices as discovered previously in the I-V measurements. In general, the magnitude of dielectric loss for both devices was found to be falling for the most part of the interval $0.007 < \tan\delta < 1$ (or $0.4° < \delta < 45°$) with minimum dielectric loss $(\tan\delta_{\min})$ appeared at minimum frequency $(f_{min} = \omega_{min}/2\pi)$ of approximately $1\,\text{kHz}$ and $2\,\text{kHz}$ for treated and untreated devices respectively. The series resistance was dominant in the higher frequency range since the LB film resistance (R_{LB}) decreases with frequency. The effect was a large dielectric loss at high frequencies.

4.3.2 Dielectric loss: Temperature dependence

In order to study the frequency variation on the dielectric loss at different temperatures, the same samples were measured under vacuum better than 10^{-5} torr in a cryostat. Figure 4.7 shows the capacitance and ac conductance for both devices as a function of frequency at temperature between 80K and 380K. Less temperature dependence (except 380K) can be seen for untreated devices as compared to the treated one. This figure shows that the dielectric constant of the LB films of $CdSt_2$ was not temperature dependent. This is in agreement with a finding by Sugi which reported that the dielectric constant of Cd^{2+} salt films is insensitive to both temperature and frequency [Sugi 1985].

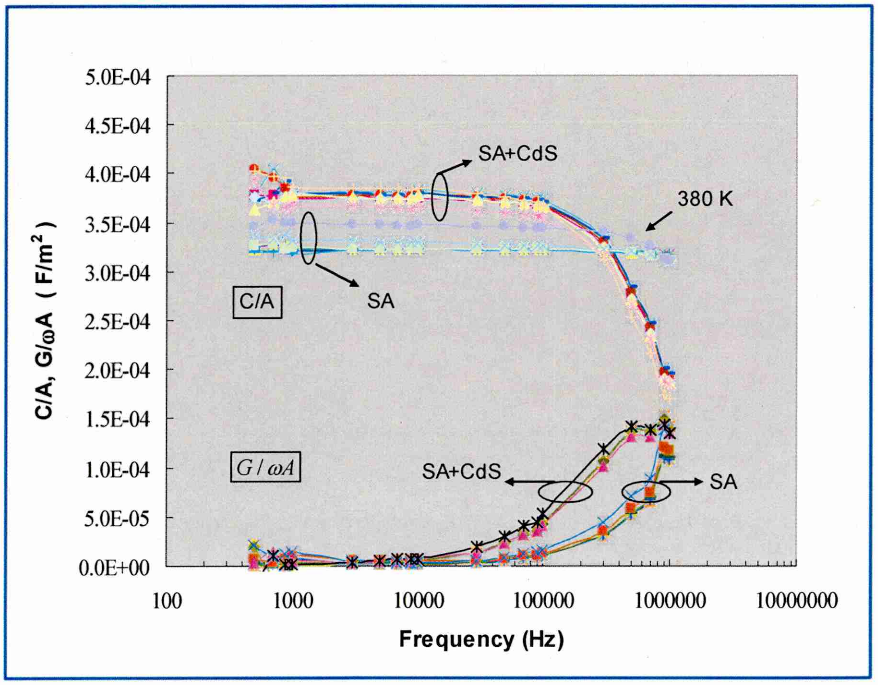

Figure 4.7. Capacitance and ac conductance of treated (SA+CdS) and untreated (SA) devices as a function of signal frequency at temperature between 80K and 380K.

Figure 4.8 and 4.9 show the dielectric loss at several fixed temperatures as a function of signal frequency for untreated and treated devices respectively. As can be seen from the figures, the dielectric loss for both devices shows weak temperature dependence at temperatures below room temperature and at high frequencies. At lower frequency (below 1kHz) evidence of temperature dependence was observed. For SA, as the temperature increases, $\tan\delta_{\min}$ occurred at minimum frequency $(f_{\min})$ of approximately 10kHz with almost no shift in $f_{\min}$. This feature is very different from the available published results in various dielectric materials such as thin-films of GaSe [Thamilselvan et al. 2004], AlNx [Gould and Awan 2004], Si_3N_4 [Awan and Gould 2003], which show the shift of $f_{\min}$ to higher frequencies as the temperature increases. This suggests that the dielectric constant $(\varepsilon = \varepsilon' + j\varepsilon'')$ of the LB films of Cadmium Stearate ($CdSt_2$) is independent of temperature.

Slightly different results have been obtained for SA+CdS (Figure 4.9). The $\tan\delta_{\min}$ occurred at lower frequency with a small shift in $f_{\min}$ to the right as the temperature increases, approximately 1kHz at 80K to 3kHz at 380K. At a higher frequency than $f_{\min}$, $\tan\delta$ increases linearly with the signal frequency. As previously mentioned, in this region, the series/contact resistance (R_S) is dominant which means that the increase in dielectric losses was most probably due to contact resistance of the device. However, for both treated and untreated devices, dielectric loss was found to increase with temperature for a frequency below $f_{\min}$. This is consistent with the Goswami & Goswami model as the ω^{-1} term becomes dominant since R decreases with temperature.

On the other hand, results of $\tan\delta$ versus frequency at several temperature on stearic acid capacitors by Kasilingam et al. has shown a single value of minimum frequency

$(f_{min} = 2\text{kHz})$ for temperature between 301K and 325K, and a lower value $(f_{min} = 1\text{kHz})$ for temperature at 180K and 183K [Kasilingam et al. 1980]. In the intermediate temperatures $183\text{K} < T < 310\text{K}$ they found that $\tan\delta$ (at f = 1kHz) has a maximum (broad peak) which they believed to be due to impurities in the LB films.

In this work, the $\tan\delta$ oscillation with the temperature at low signal frequencies was observed as shown in Figure 4.10 for SA and SA+CdS respectively. Since the magnitude of $\tan\delta$ variation is small, it can be suggested that formation of structural defects in the LB films of stearic acid is small. For high frequencies, $\tan\delta$ is independent of temperature variation below room temperature and only shows slight increase with temperature above room temperature. Again this was due to series resistance (R_S) dominated in high frequencies as predicted by Goswami & Goswami model.

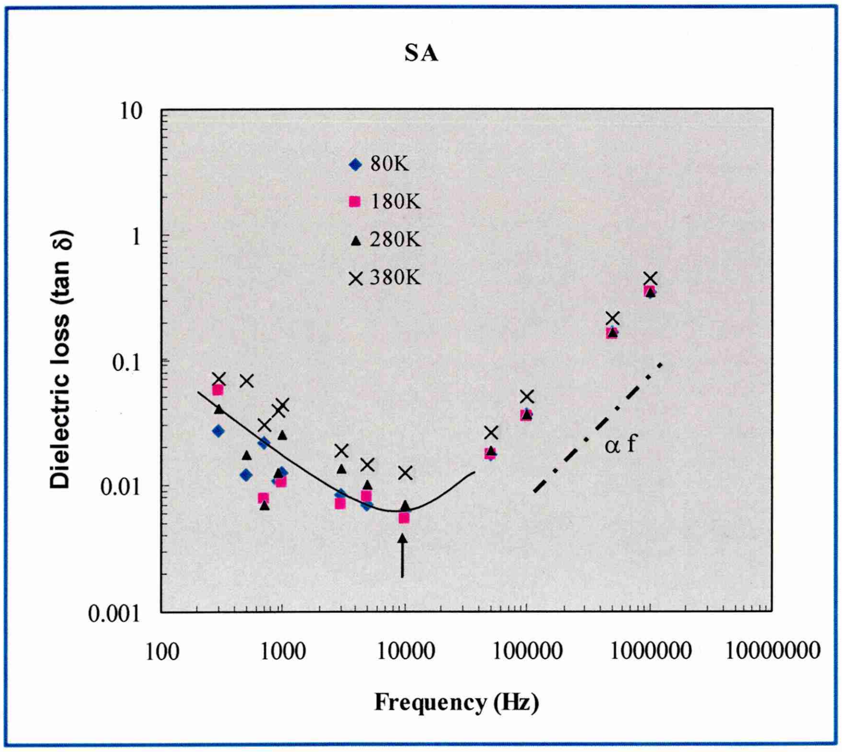

Figure 4.8. Dielectric loss as a function of modulating frequency for untreated device (SA) measured at four different temperatures.

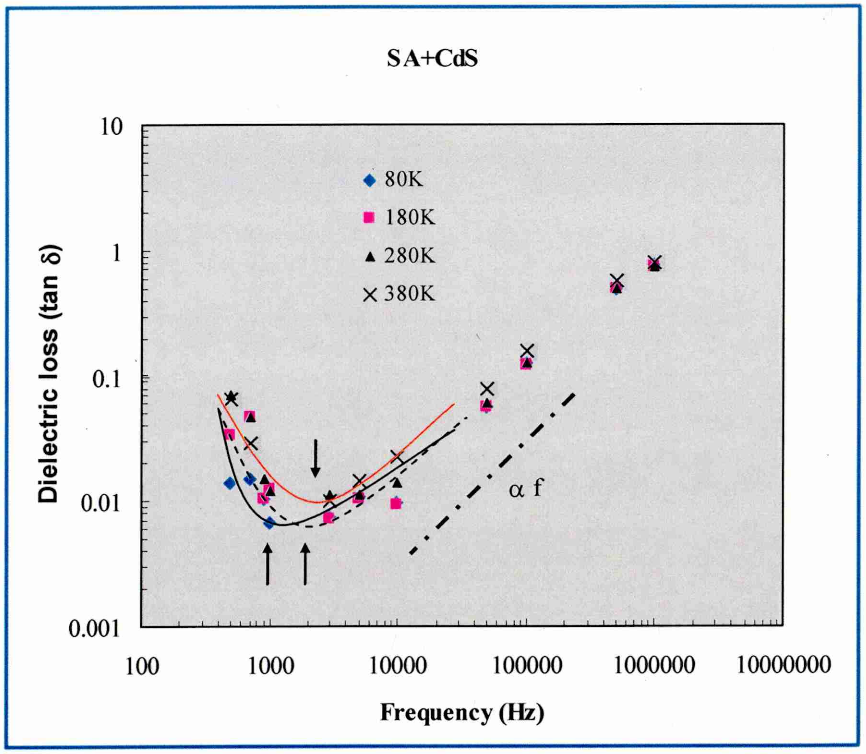

Figure 4.9. Dielectric loss as a function of modulating frequency for treated device (SA+CdS) measured at four difference temperature.

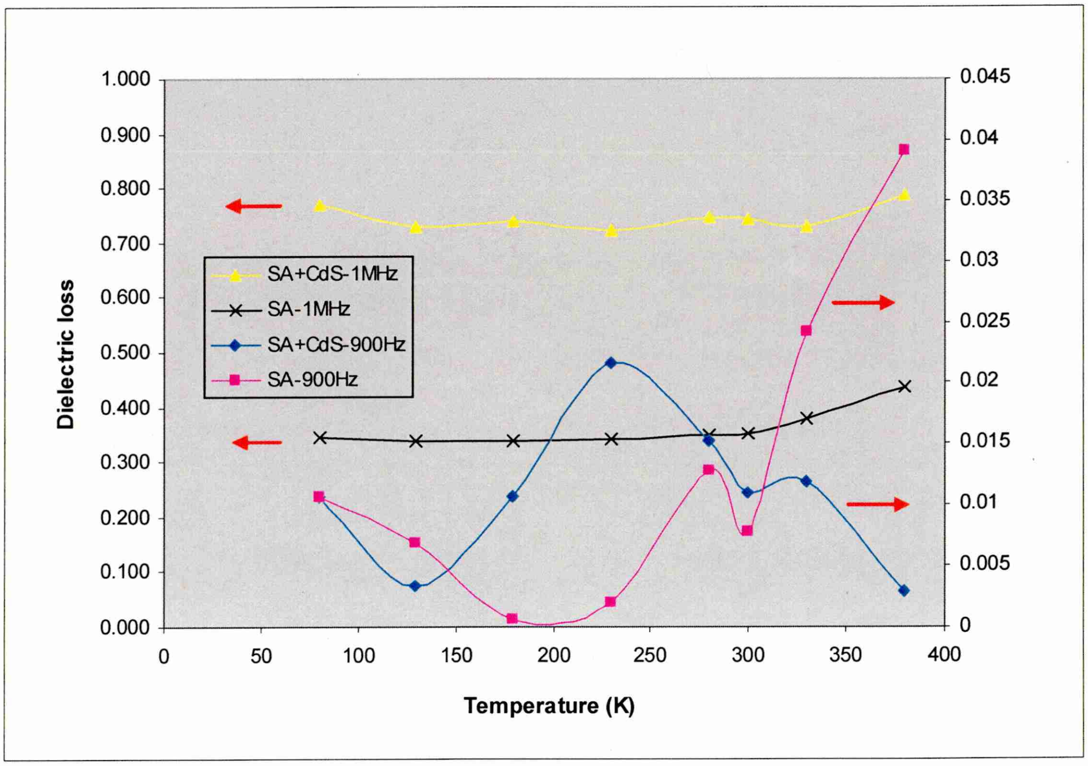

Figure 4.10. Dielectric loss as a function of temperature of treated (SA+CdS) and untreated (SA) devices at two difference frequencies, 900Hz and 1MHz.

4.3.3 Cole-Cole (Nyquist) Plot

An alternative representation of the ac electrical response can be obtained by plotting the imaginary part against the real part of the measured impedance. This plot is known as Cole-Cole or Nyquist plot. Figure 4.11 shows the Nyquist plot of the experimentally measured real and imaginary part of the treated device admittance at room temperature. A convincing plot is attained by fitting the experimental data to a second-order polynomial which resulted in an arc. Since the plot is not a semicircle, this means there was a distribution of relaxation times [Mahantappa et al. 2002].

A similar Nyquist arc which was fitted well by a second order polynomial was reported by Houston et al. on MIS structures of oxidized GaSb [Houston et. al 1997]. As can be seen from Figure 4.11, there are two intercept points on the x-axis. The high frequency intercept gives the depletion capacitance (C_d) whilst the low frequency intercept give the insulator capacitance (C_i) [Meiners et al. 1978] which is in this case, the capacitance of the LB film of stearic acid with CdS nanoparticles. The distance between the end points $(C_i - C_d)$ is equal to qAN_{ss} [Houston et al. 1997], where q, A and N_{ss} are electron charge, area of the MIS device and surface state density respectively.

From this capacitance, the dielectric constant of the film can be found since the film thickness and the area of the device are already known. From the x axis, the higher intercept value was found to be approximately 1250pF. The true capacitance value is obtained after subtracting the SiO_2 capacitance, which is approximately 115pF. The corresponding dielectric constant was found to be $\varepsilon_r = 5.1$, which is a similar value to that previously obtained by C-V measurements (Section 4.2). Surface state density (N_{ss}) is found to be $2.7\times10^{11}\ \text{cm}^{-2}$ which is half of the value obtained previously by C-

V method. The current value for N_{ss} is only an estimation and not accurate since the measurement data occupied only half of the arc [Houston et al. 1997]. Nevertheless it has given a good early estimation regarding the order of magnitude of the surface state density. An attempt to fit the experimental data for untreated devices failed to get a similar result. This could be due to the capacitance which is independent of frequency in this range.

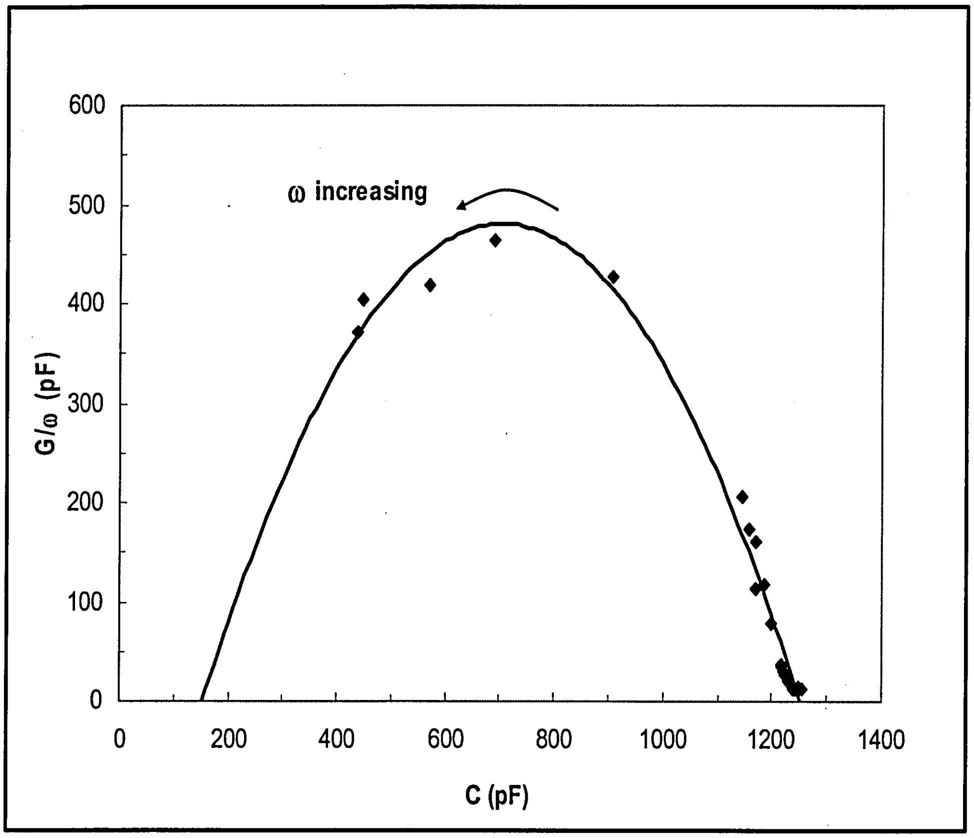

Figure 4.11. Nyquist plot of the experimentally measured admittance of treated device:- conductance normalized to the angular frequency versus capacitance. The points show the experimental data, the curve is a fit to a second-order polynomial.

4.4 Summary

A study on the dielectric behaviour of treated and untreated LB films in MIS structure has been performed in order to determine their dielectric permitivity (ϵ_{SA+CdS} and ϵ_{SA}) and dielectric loss by measuring the capacitance and conductance. Due to anomalous frequency dispersion in the accumulation region, it was not possible to determine the dielectric constant of the LB films. However, by using a two-frequency technique (Yang's model) a true LB film capacitance was extracted from the simulated C-V curve hence, the dielectric constant was obtained. It was found that the dielectric constant for untreated and treated devices are 2.3 and 5.1 respectively.

The inclusion of CdS nanoparticles in the stearic acid matrix have improved the frequency dispersion of the untreated capacitance (lossy dielectric), and caused an increase in dielectric constant. The increase in dielectric constant is related to a decrease in dc leakage current as observed in I-V characteristics which will be presented in Chapter 5. This is due to the addition of further polarisation sources, i.e. the ions modify the dipole moment distribution and are themselves polarisable entities.

The dielectric loss in both devices were fitted to Goswami & Goswami model. The treated device was found to have larger dielectric loss compared to the untreated one. This could be due to the embedded CdS nanoparticles in stearic acid matrix which act as electron traps.

CHAPTER 5

DC Analysis of Leakage Current: Results and Discussion

5.1 Introduction

In the previous chapter it was shown that by incorporating CdS nanoparticles in the stearic acid matrix, the dielectric constant of the device had increased and the C-V characteristics were improved tremendously. The works on the same devices were proceeded with the investigation of the transport mechanism due to leakage current and the results are presented in this chapter. The current-voltage (I-V) characteristics were obtained for LB films of cadmium stearate and stearic acid incorporating CdS nanoparticles in dark at room temperature and at a wide range of temperatures between 80K and 380K. The carrier transport mechanisms in the device were determined by analysing the experimental data of the I-V characteristics.

Conduction in the LB film of stearic acid has been reported earlier by several authors [Nathoo & Jonscher 1971; Mann & Kuhn 1971; Polymeropoulos 1977; Sugi 1985] but these investigations were performed in the metal-insulator-metal configurations. Stearic acid is regarded as being a good insulator and the measured current was leaking through the insulating film. The focus of the present work was on the quality of the LB film of stearic acid embedded with CdS nanoparticles for its possibility use in field effect transistors.

5.2 Transport mechanism: Room Temperature

DC electrical measurements were made in the dark at room ambient temperature on both treated and untreated samples. As shown in Figure 5.1, both devices have a metal-insulator-semiconductor (MIS) structure denotes, Al/SA/n-Si/Al and Al/SA+CdS/n-Si/Al, for untreated and treated (nano composite) devices respectively. The devices were fabricated from the same method and had similar dimensions. The only difference between them is that the treated device was exposed to H_2S gas for forming CdS nanoparticles inside the stearic acid matrix and details are described in Section 3.2.3. The back of the n-silicon substrate was connected to the ground during the entire measurements. The active device area was in the range of $2.5\,\mathrm{mm}^2$ to $3.0\,\mathrm{mm}^2$ and the thickness of the insulator layer was approximately $100\,\mathrm{nm}$.

A non-linear dependence of the leakage current I on the bias voltage V is observed in typical room temperature characteristics as shown in Figure 5.2. As can be seen from the graph, lower leakage current, about an order of magnitude in forward direction and three orders of magnitude in reverse direction, was measured in treated devices as compared to the untreated one. Similar reduction in leakage current, around two orders of magnitude, was reported by Nabok et al. (2002) on the same LB films in metal-insulator-metal (MIM) structures. It was caused by a reduction of the layer-by-layer film order due to formation of CdS nanoparticles. Because the leakage current has decreased, it is believed that the reduction in film order has created defects which cause additional energy states close to the band edge, called traps. These traps restrict the current flow because of a capture and emission process.

Exposure of LB films of stearic acid to H_2S gas has resulted in decreasing of dc conductivity and thus reduced the leakage current. From the I-V characteristics it can be seen that the built-in voltage (V_b) for untreated and treated devices are approximately $0.7\,V$ and $0.9\,V$ respectively. The inclusion of organic insulating layer between metal and semiconductor increased the turn-on voltage. The treated device turned on at a higher voltage and exhibited lower leakage current than the untreated one.

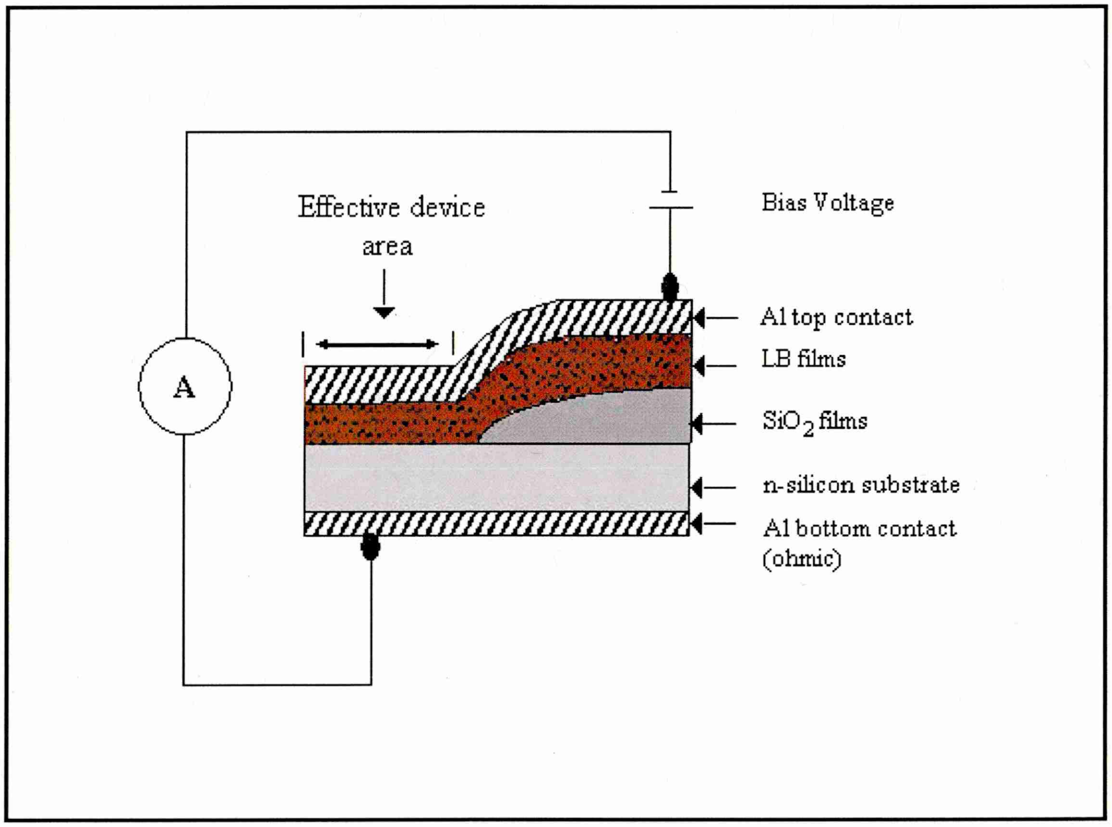

Figure 5.1. A schematic structure diagram of a fabricated device. The LB film is 40 layers of stearic acid incorporating cadmium ions ($CdSt_2$). The film thickness is approximately 100nm.

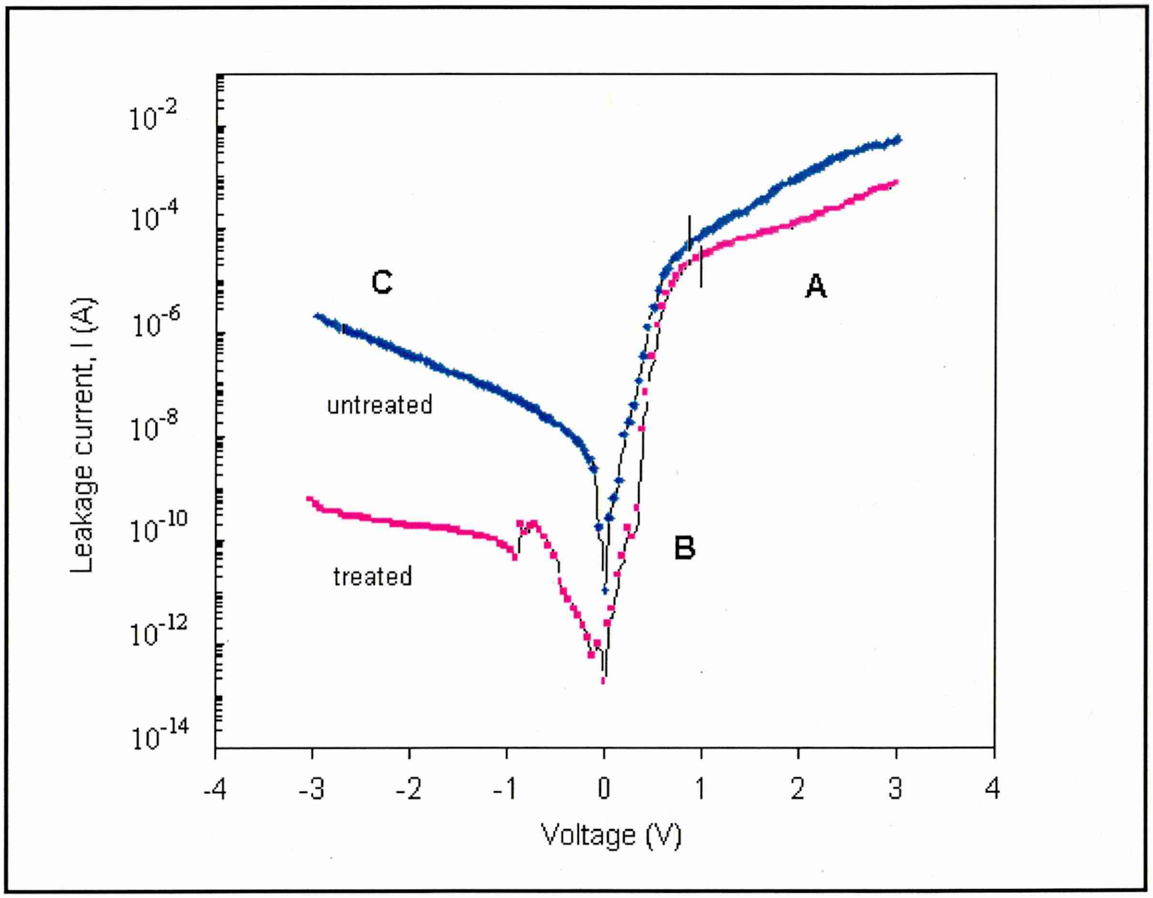

Figure 5.2. I-V characteristic for untreated and treated devices in log-linear scale at room temperature. A, B and C are the accumulation, depletion and inversion regions respectively.

The Al/LB films/n-Si/Al device consists of two different types of materials layers and the leakage current through the LB film can be interpreted in terms of three resistor model (see figure 5.3 so that

$$I = \frac{V}{R_D + R_{Si} + R_{LB}} \tag{5.1}$$

where the subscript D refers to the depletion region at the n-Si/LB film interface. R_{Si} stands for the resistance due to the non-active silicon substrate, interfacial layer and contacts. R_{LB} represents the dynamic resistance of the LB film. There exists three conduction regimes corresponding to the accumulation (Regime A), depletion (Regime B) and inversion (Regime C) modes of the MIS device as shown in figure 5.2.

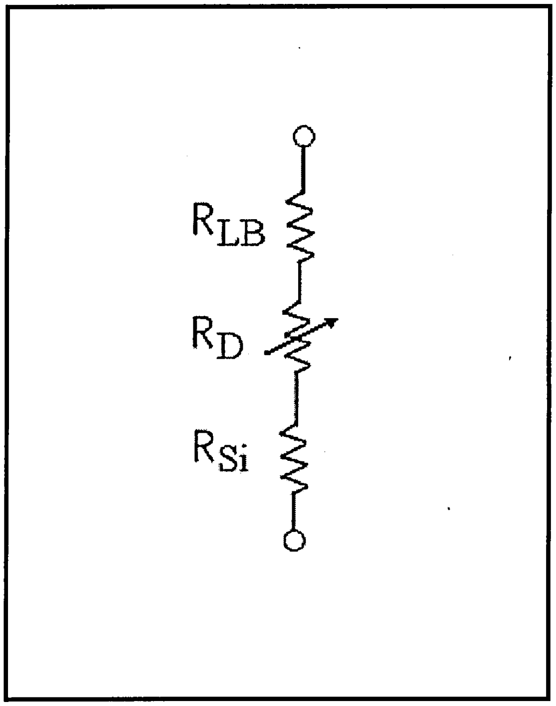

Figure 5.3 Three resistor model.

The leakage current in the insulator may be modelled as the MIS diode law [Chand S and Kumar J 1996] in the form of:

$$I = I_0 \exp\left(\frac{q(V - I(R_D + R_{Si}))}{\eta kT}\right) \tag{5.2}$$

where the parameter η is regarded as being the ideality factor, I_0 is the zero-bias current and $q = 1.6 \times 10^{-19}$ C is the value of an electronic charge. The quantity R_D is the voltage dependent resistance due to the depletion. The depletion layer in the silicon substrate near its interface with the stearic acid LB film is, therefore, primarily responsible for controlling the leakage current in the device.

For accumulation region (regime A), the depletion resistance R_D can be set to zero. Equation (5.2) may then be modified in the form:

$$I = I_0 \exp\left(\frac{q(V - IR_{Si})}{\eta_A kT}\right) \tag{5.3}$$

It is observed that

$$\frac{\partial V}{d(\ln I)} = IR_{Si} + \eta_A \frac{kT}{q} \tag{5.4}$$

The midpoint rule of differentiation was employed to determine values of $\frac{\partial V}{d(\ln I)}$ from Figure 5.2. The plot of $\frac{\partial V}{d(\ln I)}$ against I was found to be linear and the values of R_{Si} was extracted from the slope.

The inversion layer was formed when R_D reached its saturation value. The leakage current in the regime C may therefore be modelled:

$$I = I_0 \exp\left(\frac{q(V - I(R_D + R_{Si}))}{\eta_I kT}\right) \tag{5.5}$$

where the parameter η_I is regarded as being the ideality factor for the inversion regime and I_0 is the zero-bias current. It is observed that

$$\frac{\partial V}{d(\ln I)} = I(R_D + R_{Si}) + \eta_I \frac{kT}{q} \tag{5.6}$$

and the values for $R_D + R_{Si}$ was obtained. Now using Equation (5.1), it is found that the rectification ratio

$$RR = \left(1 + \frac{R_D}{R_{LB} + R_{Si}}\right) \approx \frac{R_D}{R_{LB} + R_{Si}} \tag{5.7}$$

from which R_{LB} was determined. The rectification factor (RR) is defined as the ratio of the leakage current in the accumulation regime to that in the inversion regime corresponding to a given value of $|V|$. From Figure 5.2, it was found that the rectification factor for treated and untreated devices, determined at 1V, are 4.4×10^5 and 1.3×10^3 respectively. By using Equation 5.7, the dynamic resistance of LB films for treated and untreated devices were determined to be $25\,\text{k}\Omega$ and $7.6\,\text{k}\Omega$ respectively. Table 5.1 compares all the resistances for both devices.

Sample	R_{Si} (Ω)	R_D (Ω)	R_{LB} (Ω)	*RR* (at 1V)
Untreated (SA)	1.5×10^3	1.0×10^7	7.6×10^3	1.3×10^3
Treated (SA+CdS)	1.8×10^3	1.2×10^{10}	2.5×10^4	4.4×10^5

Table 5.1. The extracted resistances of the untreated and treated devices.

5.3 Detailed analysis of conduction through LB films

The observed I-V characteristics in the accumulation region represent the true dc conductivity of the composite LB films. The analysis will be focused in this regime since it is the region where the carrier transport mechanism was predominantly controlled by the LB film resistance and the depletion resistance contribution was ignored. One of the most important aspects in analyzing the current-voltage experimental data is to identify the dominant mechanism of carrier transport through the device. As previously mentioned in Chapter 2.4, following Sze [1981] there are several possible conduction mechanisms in insulating films such as Poole-Frenkel effect, Schottky emission, tunnelling, space-charge-limited, Ohmic and ionic conduction.

Since the I-V characteristic for both devices show non-Ohmic behaviour, the current transport may be described by either a power law or an exponential law. The former relation is attributed to trap controlled space-charge-limited current (SCLC) modelled by $\left(I \alpha V^{m}\right)$, whilst the latter is interpreted in terms of either Schottky emission or Poole-Frenkel effect which can be modelled by $\left(\ln I \ \alpha \ V^{1/2}\right)$ or by Fowler-Nordheim tunnelling, modelled by $\ln\left(I / V^{2}\right) \alpha \ 1/V$.

The results were first analyzed by plotting the I-V data as $\log I$ versus $\log V$ according to the power-law. Figure 5.4 shows the I-V characteristics in term of $\log I$ against $\log V$ for both devices. As it can be seen from the graph, there is one linear region for untreated and 2 linear regions for treated devices at the high-field dc bias. By using least square fitting, the slope (m) of the graph at each region were determined and are shown in Figure 5.4.

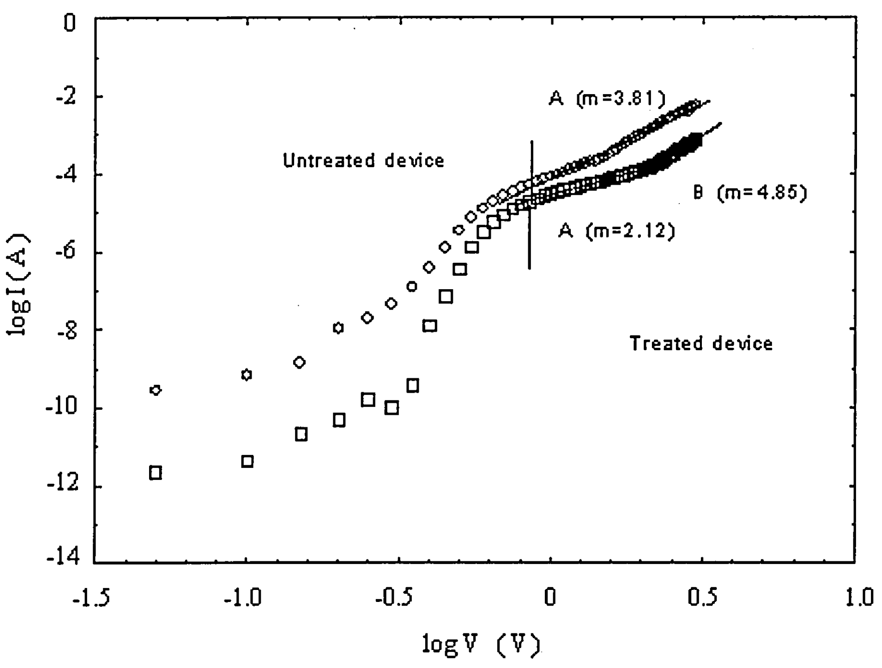

Figure 5.4. Log I versus Log V for treated (SA+CdS) and untreated (SA) devices. The slope (m) for each region is shown in bracket.

In order to consider the tunnelling mechanisms of electrons in LB films the Fowler-Nordheim plot was made for leakage current. The FN tunnelling current can be written as [Sharpe and Palmer 1996]

$$I_{FN} = 3.35\times10^{17}\left(\frac{A}{\phi d^2}\right)V^2 \exp\left[-0.69\frac{d\phi^{3/2}}{V}\right] \tag{5.8}$$

where I_{FN} is the current in mA, V is the bias voltage in volts, d is the thickness of the insulator in Å, ϕ the barrier height in eV, and A is the barrier area in m^2. From Equation 5.8, a plot of $\ln(I/V^2)$ versus $1/V$ yields a straight line whose slope equals $-0.69d\phi^{3/2}$ volts.

The value of slope carries information on barrier heights. The data in region A and B of Figure 5.4 were re-plotted as $\ln(I/V^2)$ versus $1/V$ as shown in Figure 5.5. Two linear curves with clear different slope have been observed for untreated device although they were from a same region (region A in Fig. 5.4). In this case the slope at higher voltages $(m=-4.93)$ is more negative than the slope at lower voltage $(m=-0.875)$. This indicate that a larger proportion of the tunnelling electrons are transported at higher voltages than at lower one. For treated device, linearity in the plot was observed only in region B whilst region A shown a flat response.

Since no linear dependence was observed in region A, the possibility of FN tunnelling in this region was dismissed. The corresponding barrier height ϕ values for both devices are shown in Table 5.2. The untreated devices show the possibility of current transport mechanism in the LB films due to Fowler-Nordheim tunnelling whilst there was possibility of FN tunnelling current in treated devices only at high electric field (region B). The high electric field across the films is thought to reduce the barrier width so the electron can tunnel through the barrier.

Finally, attempt has been made to fit the experimental data for the possibility of conduction mechanism due to Poole-Frenkel (PF) effect or Schottky emission. Schottky emission occurs due to thermal activation of electrons over the metal-insulator (or metal-semiconductor) interface barrier because of lowering of barrier height due to the applied field. On the other hand, the Poole-Frenkel effect is basically similar to the Schottky emission, except that it is applied to thermal excitation of electrons from traps into the conduction band of the insulator. Both mechanisms can be analysed by plotting the $\ln I$ against $V^{1/2}$.

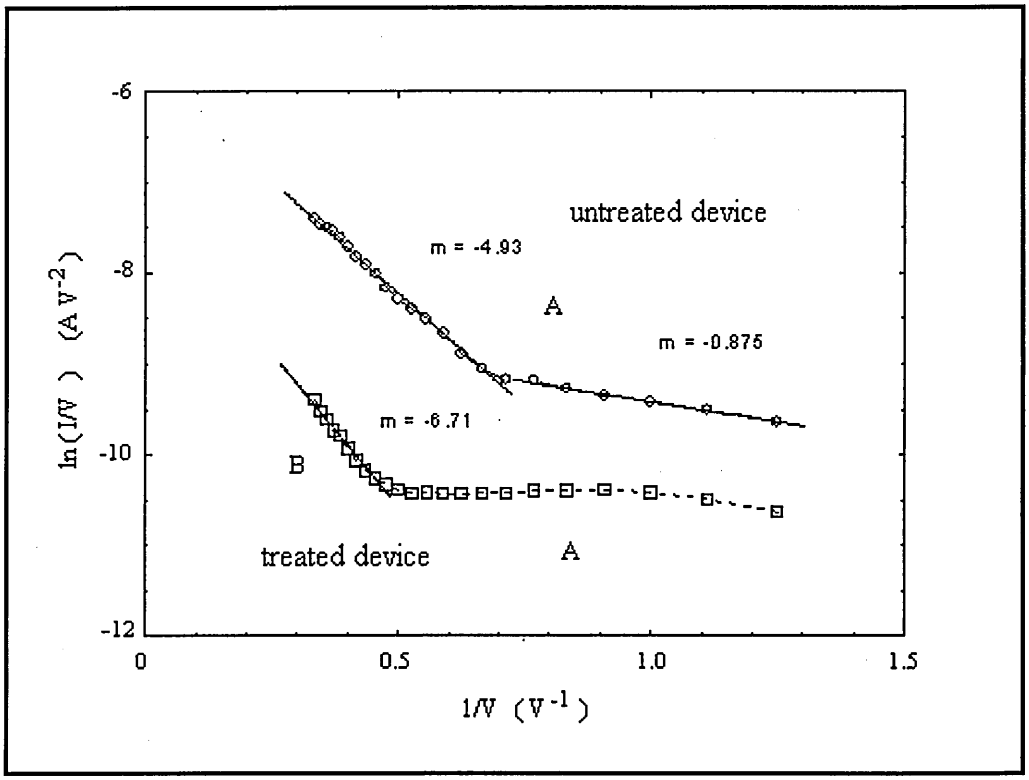

Figure 5.5. Leakage current characteristics of treated (region A and B) and untreated (region A) devices plotted as $\ln(I/V^2)$ against $1/V$ for possibility of Fowler-Nordheim tunnelling.

Device	slope (m)	Barrier height, ϕ, (eV)
Untreated	- 0.875	0.012
	- 4.93	0.037
Treated	- 6.71	0.046

Table 5.2. Tunnelling metal-insulator barrier height of the treated and untreated devices.

A linear relation of this type of graph is normally taken as evidence of either the Schottky or PF effects given as (see Section 2.3).

$$\ln I = \ln I_o + \frac{\beta V^{1/2}}{kTd^{1/2}} \tag{5.9}$$

where β is either PF or Schottky emission coefficient.

Experimentally, it is possible to distinguish between both types of conductions by comparing the obtained dielectric constant (ε_r) with the known value. Alternatively it is also possible to compare the experimental (exp) and theoretical (the) values of their specific coefficient (β) using a known dielectric constant value. The ratio between these two values $(\beta_{\exp}/\beta_{\text{the}})$ will determine the conduction process operative within the corresponding region of applied voltage. The later approach has been chosen in this work since the experimental dielectric constant for both devices were already obtained from C-V measurements. Either way, both procedures require once to know the thickness of the films.

The experimental value for β can be obtained from the slope of the graph, given by

$$\beta_{\exp} = \mathrm{mkTd}^{1/2} \tag{5.10}$$

where d is the thickness of the LB films estimated to be $100\,\mathrm{nm}$ as mentioned earlier in section 2.3.2. The theoretical value of β is given by [Gould and Shafai 1999]

$$\beta_{\text{PF (the)}} = \left(\frac{e^3}{\pi\varepsilon_r\varepsilon_o}\right)^{1/2} = 2\beta_{\text{S (the)}} \tag{5.11}$$

where e is the electron charge, ε_o and ε_r are the free space and material's dielectric constant respectively.

Forward bias data of Figure 5.2 in accumulation region are re-plotted in the form of $\ln I$ versus $V^{1/2}$ for both devices as depicted in Figure 5.6. As it can be seen from the graph, there are one linear region (A) and two linear regions (A and B) for untreated and treated devices respectively. These linear regions were analysed for the suitability of the two transport mechanisms mentioned above. Since $\beta_{PF\ (the)}$ is twice $\beta_{S\ (the)}$, the determination of both parameters are straight forward if one of them is already known.

First, the analysis began with determining the possibility of PF effect as the transport mechanism in the treated device. By using Equation 5.11, the theoretical PF coefficient $\beta_{PF\ (the)}$, was calculated to be $3.36\times10^{-5}\,\mathrm{eVm^{1/2}V^{-1/2}}$. The corresponding theoretical Schottky coefficient is half of this value, i.e. $\beta_{S\ (the)} = 1.68\times10^{-5}\,\mathrm{eVm^{1/2}V^{-1/2}}$. From the graph plotted in Figure 5.6 the slopes of the graph in every region were determined. The relative dielectric constant (ε_r) for CdS nanocomposite film (treated device) is taken as 5.1 which has been obtained earlier from the C-V measurement (see Section 4.2).

Using Equation 5.10, the experimental PF coefficients $\beta_{PF\ (exp)}$ for all regions were calculated. The completed results are given in Table 5.3 for both Poole-Frenkel and Schottky effects. From Table 5.3, it can be seen that, region A shows a strong Poole-Frenkel effect with β found to be $3.39\times10^{-5}\,\mathrm{eVm^{1/2}V^{-1/2}}$ in excellent agreement with the theoretical value. Further investigation of electron activation energy (see Section 5.3) has shown that saturation of Poole-Frenkel effect occurred in region D which is at higher electric field. This could be due to the fact that all traps were emptied and the electrons can drift in the electric field (Harrell and Gopalakrishnan 2002).

It is postulated that CdS particles act as electron traps in the bulk of the composite films. When the Coulombic potential barrier is sufficiently lowered by the application of the electric field, electrons can escape from these traps by thermal emission. Schottky emission was excluded, because the ratio between experimental and theoretical values is much greater than unity. Also the value of the relative dielectric constant extracted by assuming Schottky emission was unrealistic.

In order to compare the results, the same procedures were repeated for untreated device (SA). As can be seen from Figure 5.6 there is one linear region (A) for SA. The theoretical PF coefficient $\beta_{PF\ (exp)}$ was calculated to be $5.00\times10^{-5}\ \mathrm{eVm^{1/2}V^{-1/2}}$ by using relative dielectric constants of LB film of stearic acid (untreated device) as $\varepsilon_r = 2.3$ obtained from the C-V measurement (see section 4.2). The results were given in Table 5.4. Although it has shown an excellent agreement with the theoretical and experimental value of β, the possibility of Poole-Frenkel effect was excluded since the I-V characteristics in this area is not temperature dependent (see Figure 5.7 in Section 5.3).

By the using the same plot in Figure 5.6, the analysis was repeated for the possibility of conduction due to Schottky emission in untreated devices. The theoretical Schottky emission coefficient is calculated to be $2.50\times10^{-5}\ \mathrm{eVm^{1/2}V^{-1/2}}$. By using the same procedures as for PF effect, the ratio between experimental and theoretical values were determined. The results for each region were given in Table 5.4. No possibility of Schottky emission as a current transport mechanism and were therefore rejected.

As it has been discovered before, Fowler-Nordheim tunnelling is the most feasible current transport mechanism in untreated device. However, the barrier heights extracted from the slope of $\ln(I/V^2)$ versus $1/V$ were too small (see Table 5.2). According to Takagi's model, which is a modification of the trap-assisted-tunnelling model, the calculated low barrier height of FN tunnelling might be attributed to the dominance of direct tunnelling mechanism on both tunnelling into traps and out of traps towards the anode because of the energy relaxation at the trap site [Takagi et al. 1999].

This model was developed to successfully explain the smaller effective barrier height in the FN plot due to stress-induced leakage current (SILC) component in ultrathin SiO2 films. Therefore, the possibility of FN tunnelling is rejected. The carrier transport mechanism in LB film of stearic acid with Cd^{2+} ions ($CdSt_2$) as proposed by [Sugi 1985], which described a combination of thermally activated hopping within the plane of carboxylic head groups and electron tunnelling through each LB bilayer, is the most possible explanation for the current conduction in untreated device.

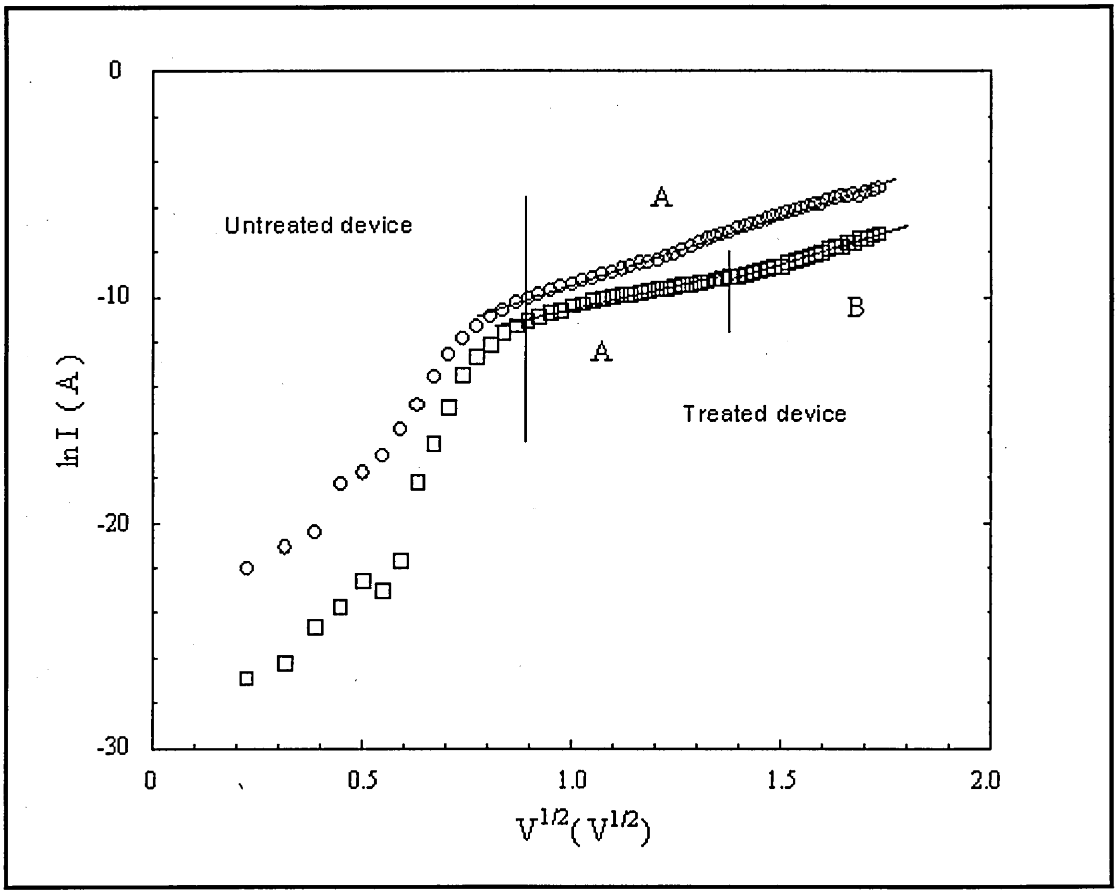

Figure 5.6. Plot of ln I versus $V^{1/2}$ for dark forward bias current-voltage characteristics of LB films for both untreated and treated samples at room ambient temperature.

Region	Slope (m)	(eV $m^{1/2}V^{-1/2}$) x 10^{-5}			$\beta_{PF\,(exp)}/\beta_{PF\,(the)}$	$\beta_{S\,(exp)}/\beta_{S\,(the)}$
		$\beta_{(exp)}$	$\beta_{PF(the)}$	$\beta_{S(the)}$		
A	4.16	3.39	3.36	1.68	1.01	2.02
B	5.71	4.67	3.36	1.68	1.39	2.78

Table 5.3. Poole-Frenkel and Schottky coefficients for treated device in region A and B.

Region	Slope (m)	$(\text{eV m}^{1/2}\text{V}^{-1/2}) \times 10^{-5}$			$\beta_{PF\,(exp)}/\beta_{PF\,(the)}$	$\beta_{S\,(exp)}/\beta_{S\,(the)}$
		$\beta_{(exp)}$	$\beta_{PF(the)}$	$\beta_{S(the)}$		
A	6.1	4.99	5.00	2.5	1.00	0.5

Table 5.4. Poole-Frenkel and Schottky coefficients for untreated device.

5.4 Temperature dependence and activation energy

The device was placed in a cryostat and under vacuum. Measurements were repeated over the temperature range between 80K and 380K. Figure 5.7 shows the I-V characteristics for untreated and treated devices respectively in semi log scale. Again lower leakage current is measured for treated device (SA+CdS) as measured previously in dark at room temperature. Both I-V characteristics show exponential behaviour. At room temperature and below, the current through SA was found to be independent of temperature variation for voltage higher than approximately 0.6V. This could suggest the electron hopping and tunnelling behaviour in multilayer LB film of stearic acid as proposed by [Sugi 1985].

Since the melting point for stearic acid is approximately 71.5°C (344.5K), the measurement for untreated device should has been stopped at temperature below than 330K at the highest point. There was an abrupt increased in current at 380K which could be due to the thermal disturbance of the stearic acid chain which made the multilayer of cadmium stearate unstable. Multilayer LB film of cadmium stearate remain stable up to approximately 100°C (373K) [Tredgold 1984].

In contrast, the results for treated device have shown a dependence on temperature throughout the biasing scheme up to about 2V. Higher than 2V, less temperature dependence behaviour was observed. However there was no abrupt increased in current due to temperature variation as observed in untreated device.

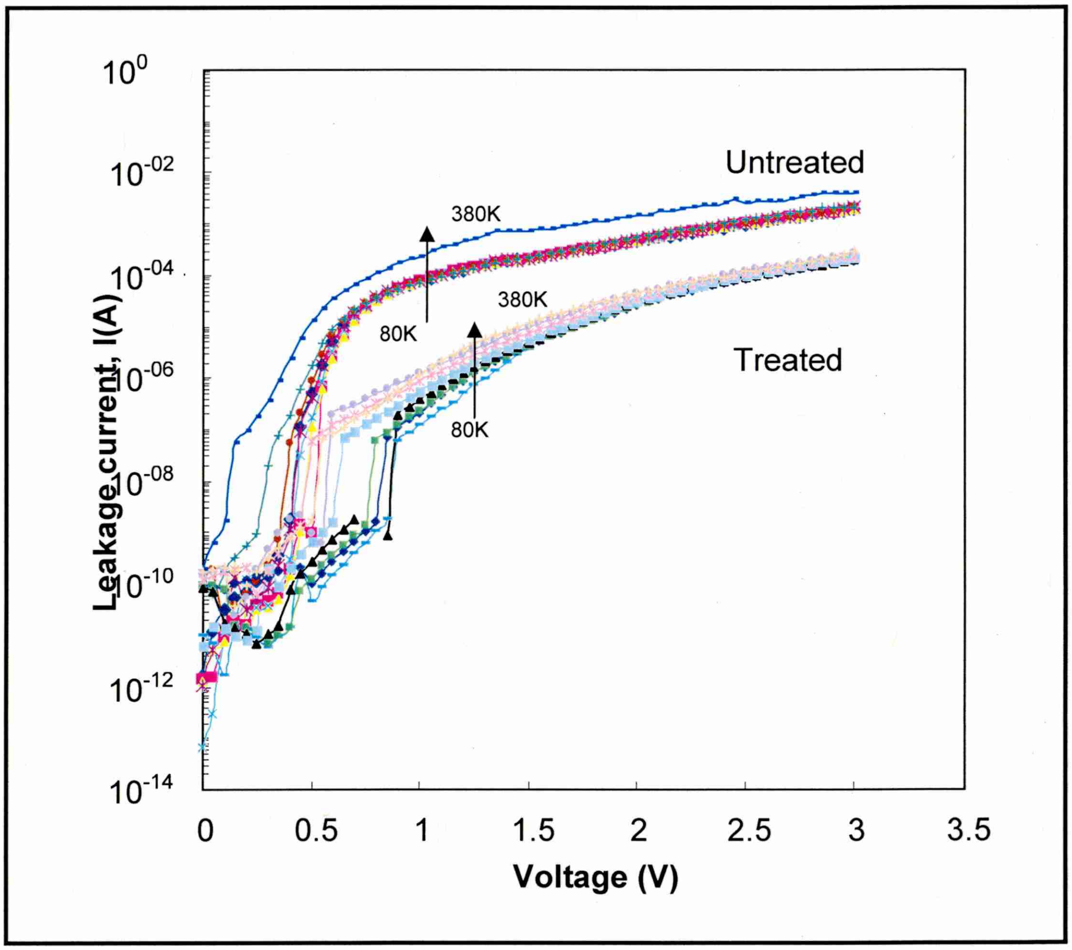

Figure 5.7. Log-linear scale of forward leakage current for treated and untreated devices over temperature range between 80K and 380K. The temperature is set at 80K, 130K, 180K, 230K, 280K, 300K, 330K, and 380K. Arrows (→) show the increase in temperature.

Further investigations were done to determine the activation energy (ΔE) by plotting the dc current density (or dc conductivity) as a function of inverse temperature. Figure 5.8 and 5.9 show the $\ln J$ vs. $1000/T$ for temperature in the range of 80K up to 380K for both SA and SA+CdS respectively at several different operating bias voltages. Both devices show different temperature dependence. The untreated device has clearly shown weak temperature dependence at temperature up to 330K for the whole biasing voltage as display in Figure 5.9. For temperature higher than 330K a strong dependence on temperature has been observed as shown by a steep increase in current. As previously mentioned, this was due to instable in stearic acid films at temperature higher than 344K.

Different types of the behaviour was observed for treated devices. For biasing voltage below 1.5V, strong temperature dependence was observed. A weak temperature dependence is observed when the operating voltage exceeded 1.5V. At above room temperature a strong temperature dependency is observed for the whole bias voltage as in untreated device but with less steep increase in current which suggest lower activation energy involved.

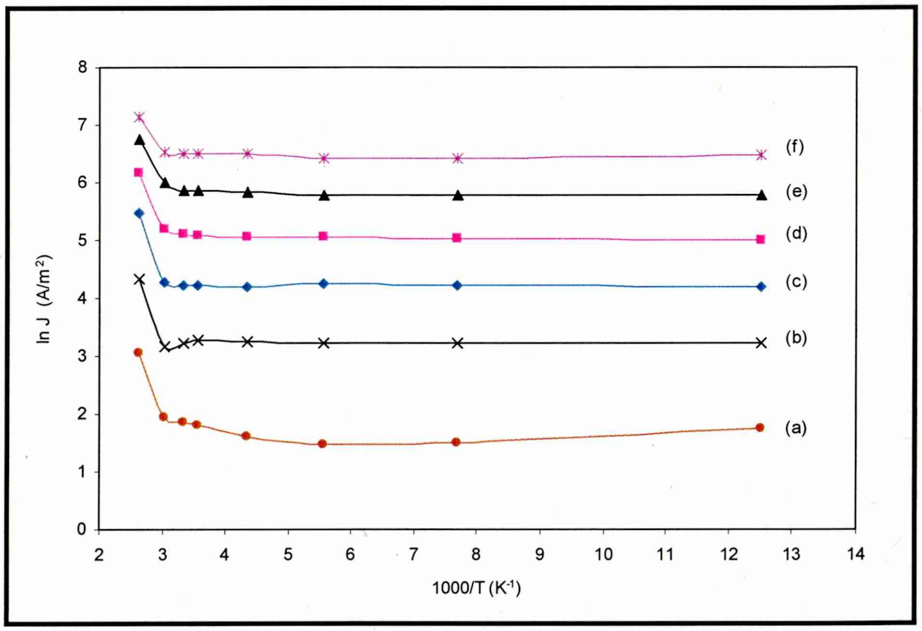

Figure 5.8. Plot of ln J versus 1000/T for untreated device at several bias voltage (a) 0.7V, (b) 1.0V, (c) 1.5V, (d) 2.0V, (e) 2.5V and (f) 3.0V

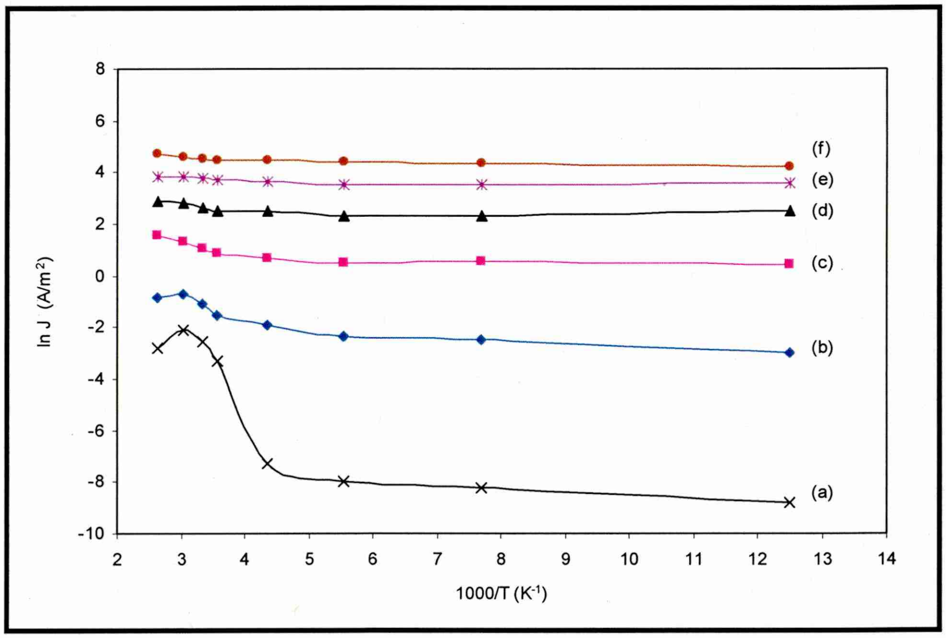

Figure 5.9. Plot of ln J versus 1000/T for treated device at several bias voltage (a) 0.7V, (b) 1.0V, (c) 1.5V, (d) 2.0V, (e) 2.5V and (f) 3.0V

In order to determine and compare the activation energy of the treated and untreated devices, the temperature dependence of the current at certain fixed bias voltage has been studied. Figure 5.10 depicts the temperature dependence of current density ***J*** at two different operating voltages, 1V, and 2.5V. Fixed voltage of 1V and 2.5V were chosen since they represent two different regimes in the I-V characteristics. At an operating voltage of 1V and 2.5V it can be seen that for SA the current is less dependent on temperature at below room temperature. For SA+CdS at V = 1V there is a strong temperature dependence while at higher applied voltage, V=2.5V, the temperature dependence becomes less pronounced.

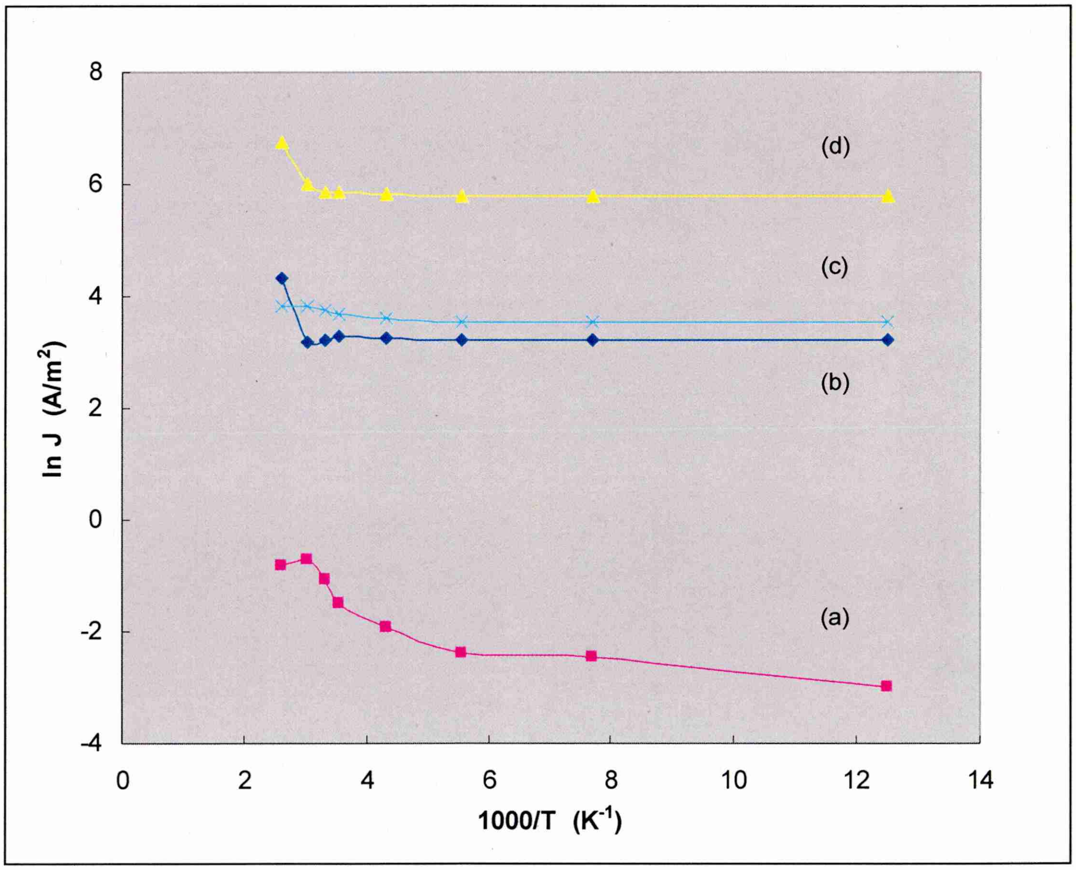

Figure 5.10. Plot of log J vs 1000/T for untreated [(b) and (d)] and treated devices [(a) and (c)] at 1V [(a) and (c)] and 2.5V [(b) and (d)].

The dependence of conduction current on temperature and applied voltage, can be described by the following equation:

$$J=J_0\exp\left[-\frac{\Delta E(V,T)}{kT}\right] \tag{5.6}$$

where ΔE is the electron activation energy. J_0 is the current density at infinity temperature. The Boltzmann's constant is $k=8.625\times10^{-5}\,eVK^{-1}$. The activation energy ΔE for low temperature $(<300\text{K})$ and high temperature $(>300\text{K})$ regions are deduced from $\ln J$ vs. $1/\text{T}$ and are listed in Table 5.5.

	untreated (SA)		treated (SA+CdS)	
Bias Voltage	1V	2.5V	1V	2.5V
Activation energy (< 300K) (meV)	0.34	0.16	8.13	0.23
Activation energy (> 300K) (meV)	250	110	130	13

Table 5.5. Activation energy of untreated (SA) and treated (SA+CdS) devices for two different ranges of temperature and at two different bias voltages.

As can be seen from Table 5.5 the activation energy for SA+CdS was found to be higher than the activation energy of SA at temperatures below room temperature (RT). This could be an indicator of a different carrier transport mechanism in both devices. Since the transport mechanism in treated device is the main goal, further investigation was done with a determination of activation energy at bias voltage in between 1V and 2V (region A in Figure 5.6).

An Arrhenius plot of conductivity (G) as a function of $1/T$ is shown in Figure 5.11 for the SA+CdS composite films at $1.5\,V$. The resulting graph shows two distinct activation regimes separated by temperature of $T = 280\,K$. Two mechanisms are believed to be operative over this entire temperature range [Harrel 1999]. For temperature regime $T \geq 280\,K$, the steep rise in conduction is primarily due to the increasing release of electrons from the traps with temperature as predicted by Roth et al. [Roth et al. 2002] and the value of Φ is estimated to be $65\,\text{meV}$.

At lower temperature regime $(T < 280K)$ the reduction of barrier due to the bias is a dominantly responsible mechanism for detrapping and the trapping sites which become active at these temperatures with a smaller barrier height of $1.3\,\text{meV}$. This variation in the barrier height Φ is possible due to the existence of a distribution of trap levels instead of the single level assumed in the original Frenkel's model. Electrons are believed to be released from the traps due to the combination of temperature and reduced barrier effects. Due to traps released, it is believed that Region B in Figure 5.6 refers to the saturation regime in which the trapped electrons are free. Using the criteria for saturation conditions [Harrell 2002], the saturation voltage V_S lies between $1.6\,V$ and $2.8\,V$.

The detrapping is no longer sensitive to temperature and the current is found to be temperature independent irrespective of applied voltages within this saturation range. All the above analysis has been performed by assuming the Poole-Frenkel effect in 1 dimension $(1D)$. The lateral dimensions are much larger than the film thickness so the probability of occurrence of the three dimensional Poole-Frenkel effects is small [Jonscher 1967].

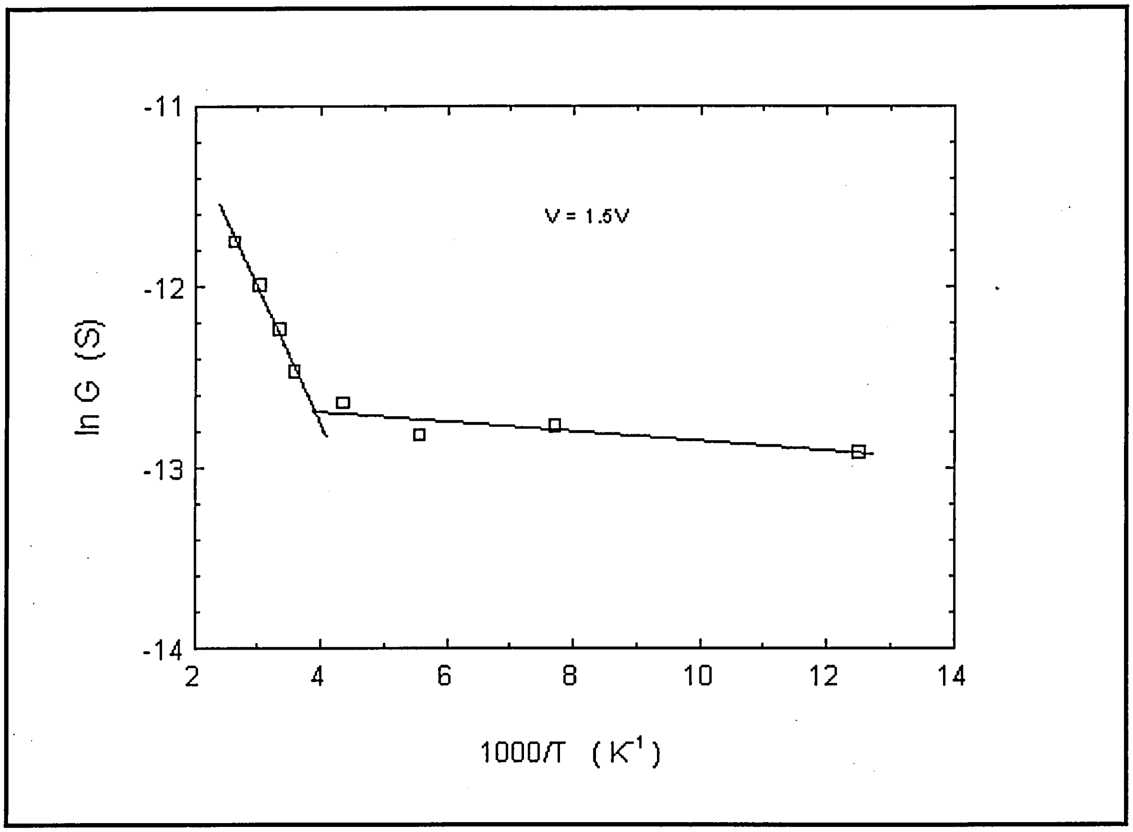

Figure 5.11. A plot of ln$G$ vs $^{1000}\!/_{T}$ for the SA+CdS composite films at V=1.5V.

5.5 Summary

The dc electrical measurements were performed on the treated and untreated LB films of cadmium stearate in metal-insulator-semiconductor (MIS) structure. Lower leakage current of one-order of magnitude was found in the device containing CdS nanoparticles embedded in the stearic acid matrix (treated device). This could be due to the increase in dielectric constant as found in C-V measurement in chapter 4 which means high device capacitance. This has interpreted in low leakage current flows in MIS capacitor. The treated device also exhibit higher rectification factor than the untreated one.

The analysis of leakage current-voltage characteristics to determine the possibility of current transport mechanism were done. Since the transport mechanism in the LB films of cadmium stearate is already known, the focus of the analysis was on the treated device. It was found that the Poole-Frenkel effect is prevalent for charge transport in the LB films containing CdS nanoparticles at the field higher than $10^7\ \mathrm{Vm}^{-1}$. The effect becomes saturated at higher fields.

CHAPTER 6

Low-Frequency Noise Measurement: Results and Discussion

6.1 Introduction

In chapter 4 and 5, the a.c. and d.c experimental results of the hybrid MIS structures of organic-inorganic LB films before and after treatment to H_2S gas have been explained in detail. It has been found that the treated devices have different a.c. and d.c characteristics compared to the untreated ones. The investigation was proceeded by measuring the low-frequency noise properties in the same device structures and the results are presented here.

The Low-frequency noise technique is known as a sensitive tool which is capable of probing down to localized microscopic phenomena of the devices. It can be regarded as a diagnostic tool for use in any application concerning the reliability of electron devices. One of the goals in any low-frequency noise measurements is to investigate the origin of the noise sources residing in the electron devices which is the main purpose of this study.

From literature, it was found that most of the research in low-frequency noise are in inorganic semiconductor devices mostly metal-oxide-semiconductor (MOS) devices in lateral configuration between source and drain. In contrast to semiconductor devices, noise investigations on organic and nanostructure devices are rare. Only recently studies on organic based devices such as OLED [Ferrari et al. 2002], organic transistor

[Necliudov et al. 2000; Martin et al. 2000; Deen et al. 2001; Vandamme et al. 2002; Marinov et al. 2004] and nanostructure devices such as WO_3 [Otten et al. 2000] and PbS [Hoel et al. 2002] nanoparticle films, LED with InAs quantum dots [Dobrzanski 2004], and carbon nanotubes [Collins et al. 2000; Ouacha et al. 2002] have been reported.

Also from literature it was found that, no low-frequency noise measurement on any LB films has been reported so far. Moreover, the scientific knowledge in electrical transport mechanism in nanocomposite systems requires further investigation. As a result, experimental data are few and far between and it is difficult to make a meaningful comparison for their physical interpretation. However, our results were analysed with available reports on inorganic MOSFETs, organic materials in TFTs and in diode-like structures. It is hoped that the experiments will contribute to some new knowledge in LB films of cadmium stearate with and without CdS nanoparticles.

6.2 Current Noise Spectral Density

The current noise power spectral density was evaluated for treated (SA) and untreated (SA+CdS) devices in MIS structure. Since both devices have input resistance greater than 10 kΩ, a transimpedance method, as described in Section 3.4.1, was chosen. The device was placed in series with the transimpedance amplifier and the fluctuations in the dc current were measured by biasing the device at a constant voltage. The detail of experimental setup technique and procedures are as presented in Section 3.4.

As the first step, the system background noise was measured . This was necessary in order to investigate the resistance/conductance behaviour of the device when not in bias. When no bias was applied to the device neither flicker nor generation and recombination (G-R) noise are expected. The device was said to be at thermal equilibrium and only exhibited thermal noise (or Johnson noise) of a conductance (G). The system background noise was then a system noise floor which was the lowest limit of any measurable measurements. Any noise level which is lower than this value will not be detected by the transimpedance amplifier. From the plot of ac conductance (G) versus frequency (f) it was found that (as is also described in Section 4.3) the ac conductivity of the devices are highly dependent on the modulating signal frequency, as shown in Figure 6.1. This implied that the thermal noise current power spectra density (PSD), $S_I(f) = 4kTG(f)$, also increases with the frequency. Similar behaviour has been observed in ferroelectric material which was reported by Gerard et al. [Gerard et al. 2001].

The system background noise for treated (SA+CdS) and untreated (SA) devices were measured by using two different amplifier sensitivities, 10^{-7} A/V and 10^{-8} A/V LN and the results were summarised in Figure 6.2. From the graph it can be seen that, for the frequency below about 100 Hz for 10^{-8} A/V LN and 1 kHz for 10^{-7} A/V, the system background noise was solely due to amplifier noise. This shows that the DUT background noise was much lower than the amplifier background noise thus cannot be resolved by the amplifier.

Due to bandwidth limitation of the amplifier at its highest sensitivity (10^{-8} A/V LN) (as was previously mentioned in Section 3.4.3), the amplifier gain at 10^{-7} A/V was used for the upper frequencies (above ≈ 4kHz) to determine the system background noise. Both DUTs had background noise power spectral densities which were highly dependent on the frequency. Because of this, the lowest level of measurable noise was limited by the system background noise. This was regarded as being the thermal noise of the device under test.

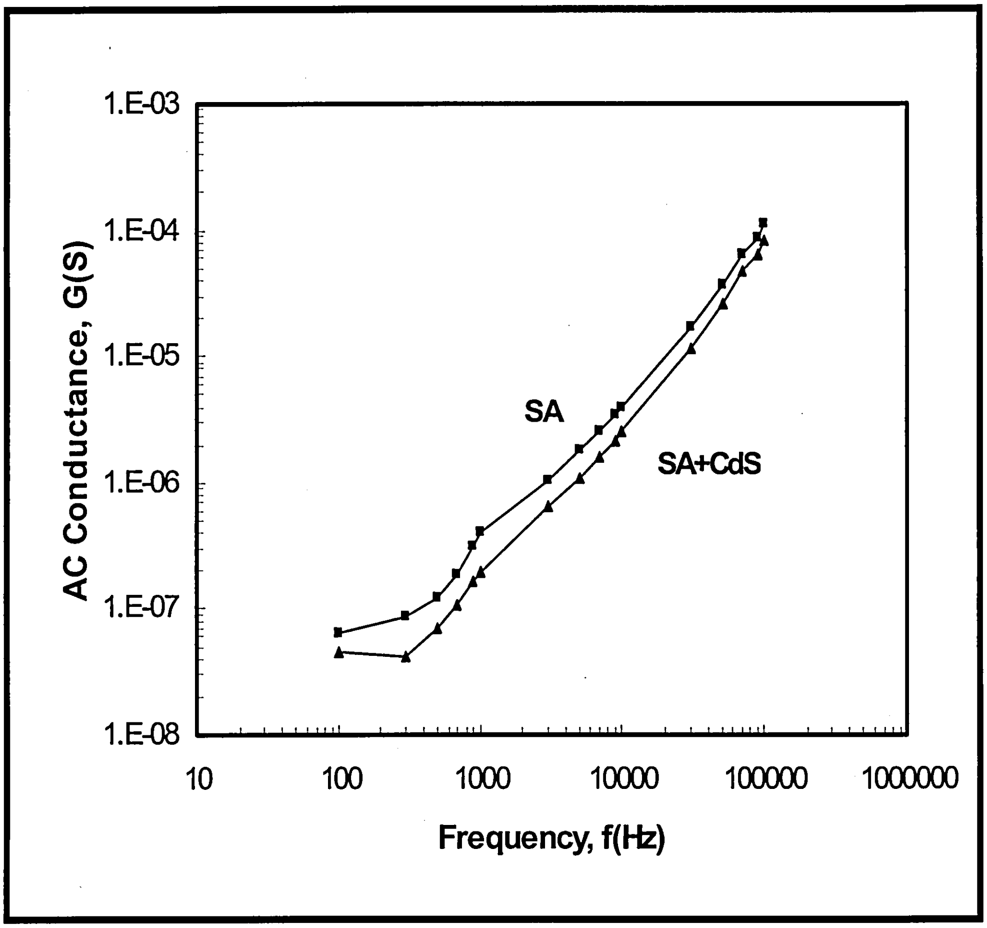

Figure 6.1. The measured ac conductance (G) of the treated and untreated devices.

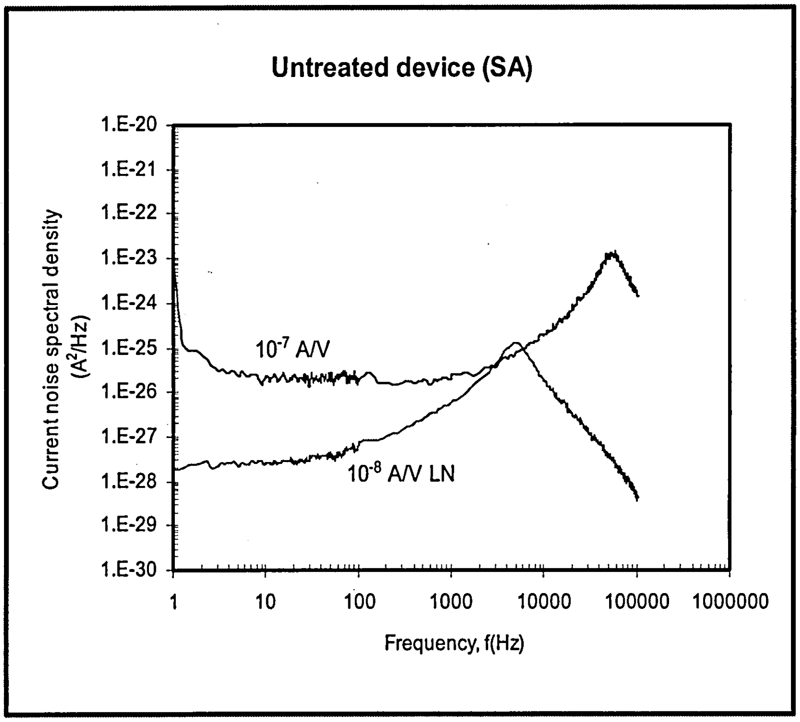

(a)

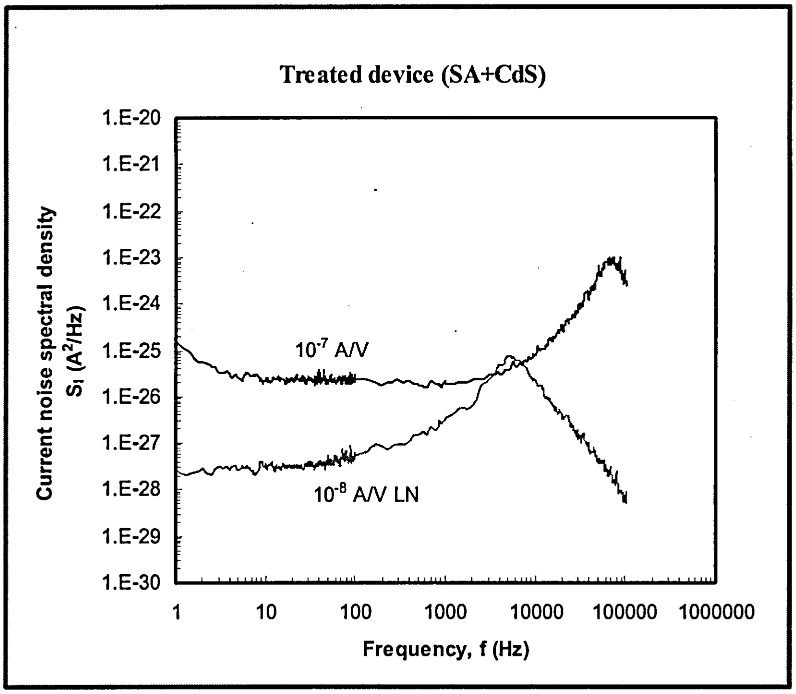

(b)

Figure 6.2. The measured system background (Johnson) noise for (a) untreated device and (b) treated device.

Once the system background noise was identified, low-frequency noise characterisation was continued by measuring the DUT at non-equilibrium condition. Since the goal of these measurements was to compare the two devices, the same current values were chosen for both DUTs. The electrical noise was measured with dc bias current varying from 20 nA up to 100 μA that is in the depletion and accumulation region of the device. The measurements were performed at frequencies ranging between 1 Hz and 100 kHz at room temperature. The I-V characteristics of both devices in the region of interest (A and B) are given in Figure 6.3.

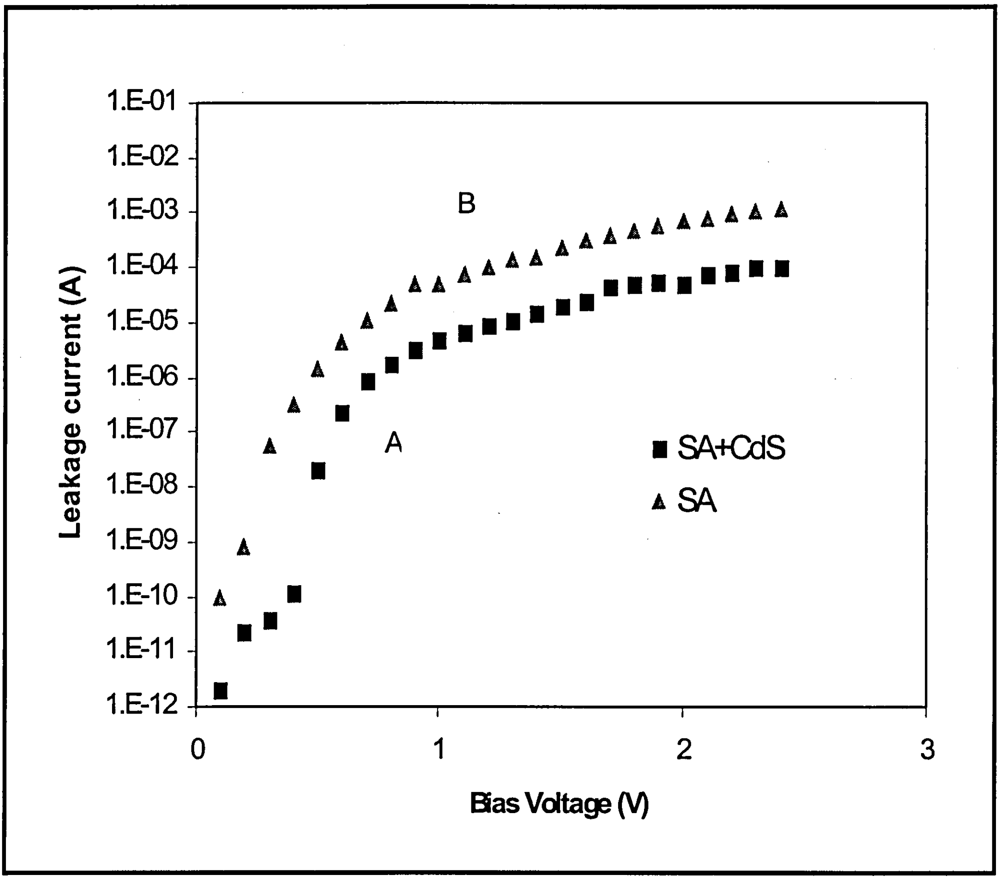

Figure 6.3 Forward bias I-V characteristics of treated (SA+CdS) and untreated (SA) devices in regime of interest A and B.

Figure 6.4 and 6.5 shows the current noise power spectral density (PSD) of untreated and treated devices as a function of frequency for different forward bias current. Noise spectra of $1/f$ type was observed experimentally over more than 4 orders of magnitude of frequency range for both devices for the whole range of leakage current. Noise PSDs were found to decrease with frequency but increase with bias current. For the same value of dc current, a treated device was found to have current noise PSD approximately two orders of magnitude higher than untreated device. This was expected since by incorporating CdS nanoparticles into a stearic acid matrix the surface structure of the films had changed, as seen by AFM. Nevertheless, such complicated structures still have noise behaviour comparable to ordinary devices.

Neither shot noise nor generation-recombination (G-R) noise was observed during the measurements and their contributions, therefore, were neglected. The peaks in the graph were due to the bandwidth limitation of the transimpedance amplifier as previously described in Section 3.4.

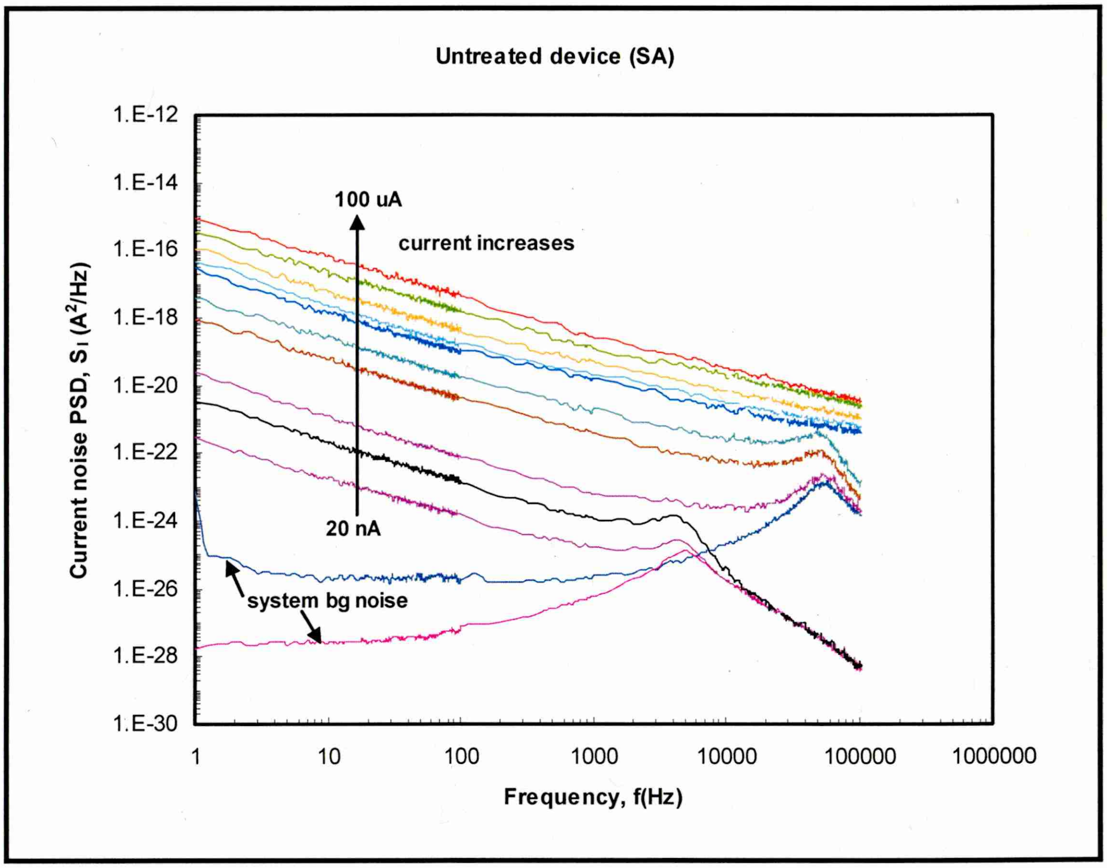

Figure 6.4. Current noise spectral density for untreated devices. System background noises are shown as reference.

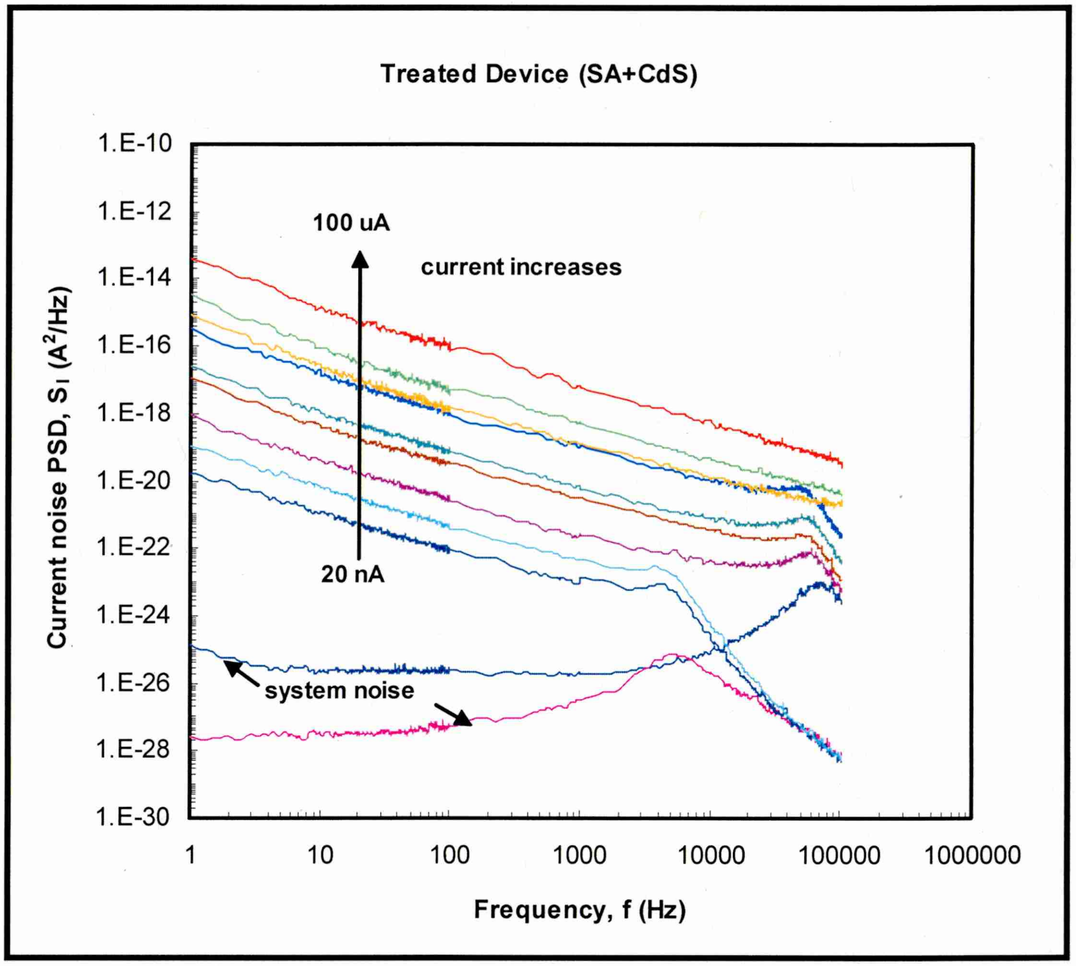

Figure 6.5. Current noise spectral density for treated devices. System background noises are shown as reference.

6.3 Parameters Extraction

As the current noise power spectra density $S_I(f)$ showed only $1/f$ noise behaviour, the experimental data were modelled empirically by Equation 2.65. The details were described in Section 2.4.5.3 in Chapter 2. It was successfully used to model the experimental $1/f$ data in semiconductor diodes [Chen et al. 2000; Blecher et al. 98]. A similar expression was also used [Martin et al. 2000] to quantify drain current noise spectral density in organic TFTs. This equation is written again here as

$$S_I(f) \propto \frac{I^\beta}{f^\gamma} = C\frac{I^\beta}{f^\gamma} \qquad (6.1)$$

where β, γ, and C are the $1/f$ noise constants that need to be extracted. I is the dc current flowing through the device where the $1/f$ noise is generated and f is the frequency at which the dc current is fluctuating. Both I and f are parameters which can be made constant when analysing the current noise spectral density data, $S_I(f)$. The $1/f$ exponent γ is a measure of the distribution of traps responsible for the carrier number fluctuations. The bias exponent β is a measure of the mixing of various noise sources in the device. The constant C is a $1/f$ noise magnitude which is a device-dependent factor and can be considered as a quality indicator of the device. For simplicity, C takes arbitrary unit. By applying the logarithm function to Equation 6.1, two linear equations (depending on which $1/f$ constant to be extracted) can be obtained as

$$\log S_I(f) = \log\left(C \cdot I^\beta\right) - \gamma \cdot \log f \qquad (6.2)$$

when I is set constant and varying f, and

$$\log S_I(f) = \log\left(\frac{C}{f^{\gamma}}\right) + \beta \cdot \log I \tag{6.3}$$

when f is set constant and varying I. The constant C is extracted by varying the bias current at fixed frequency and can be obtained from

$$C = \frac{f^{\gamma} \cdot S_I(f)}{I^{\beta}} \tag{6.4}$$

where the frequency exponent γ is determined from the slope of noise power $[S_I(f)]$ vs. frequency (Equation 6.2) at fixed current (I) while β from the slope of noise power vs. current (Equation 6.3) at fixed frequency (f).

The frequency index γ was obtained by a least squares fit of the measured spectrum (Equation 6.2) to be in between 1.06 and 1.18 and between 1.15 and 1.35 for untreated and treated devices respectively. The results are shown in Figure 6.6 (a) and (b) for frequency range from 1 Hz to 1 kHz. γ for untreated device was found to be less dependent on the biasing current. The results for untreated devices are close to pure $1/f$, which indicates a uniform distribution of trap energies in the LB films of stearic acid. This is a plausible observation in light of the fact that the LB films consist of periodically well-organised layer-by-layer structures. Martin et al. (2000) reported $\gamma \cong 1 \pm 10\%$ in organic thin-film transistors and this observation is attributed to the uniform distribution of trap energies.

A different behaviour was observed in treated devices. The exponent γ showed a trend of increasing with the bias current. After the inclusion of CdS nanoparticles in the stearic acid matrix, the distribution of traps energies in the films was believed to be perturbed resulting in increases of γ value. Nevertheless the value for γ was still within an acceptable range for the noise to be classified as $1/f$ which is in the range of $0.7 \le \gamma \le 1.4$ [Butler et al. 1996].

In contrast, Ferrari et al. (2002) reported a consistence high value of γ in between 1.24 and 1.35 and were independent of biasing conditions found in current noise spectroscopy of organic LEDs (oLEDs). It was attributed to the microphysics of the contacts between organic materials and metal contacts. The situation is similar to what were found in inorganic devices at the earliest stages of their development. The γ value was even higher in nanostructure materials. Ouacha et al. (2002) have reported an average value of γ of 1.56 for two crossing multiwalled carbon nanotubes and suggested that a diffusion of carriers between two different media (nanotubes) was responsible for the noise observed. Even in modern inorganic semiconductors there are reports regarding to high value of γ. Recently it has been reported [Jonghwan et al. 2003] that $1/f^{\gamma}$ noise of gate leakage current in ultrathin oxide MOSFETs has a value of γ in the range of 0.9 to 1.7. They concluded that the capture cross-sections depend strongly on the surface potential and decrease exponentially with the surface potential towards the midgap [Jonghwan et al. 2003]. This might explain the increase in γ for treated devices (SA+CdS) which was known to have a rough surface compared to untreated devices (as shown in AFM pictures).

The frequency exponent γ is related to the thermal energy kT and the trap distribution parameter E_t by a simple relationship [Hastas et al. 2000]

$$E_t = \frac{kT}{1-\gamma} \tag{6.5}$$

The $1/f^{\gamma}$ behaviour of the current noise spectra of Figure 6.4 and Figure 6.5 can be explained from the above tail state model to determine the origin of the noise. From experimental value of γ, and by using Equation 6.5, the distribution parameter E_t of the tail states can be evaluated. The distribution parameter E_t for both devices is shown in Figure 6.7(a) and (b) for untreated and treated devices respectively.

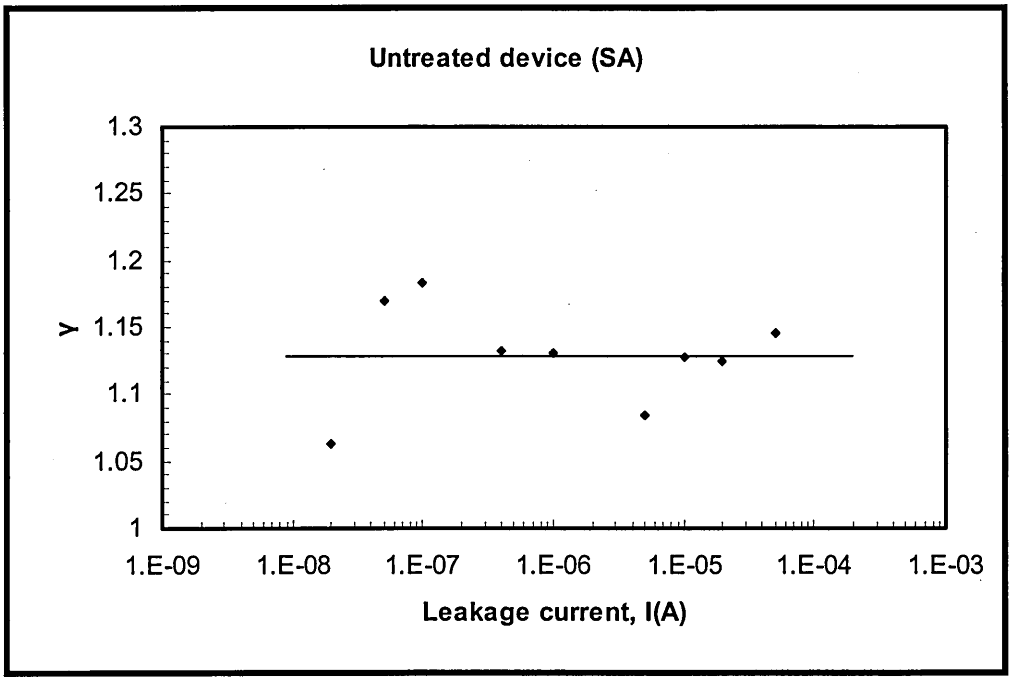

(a)

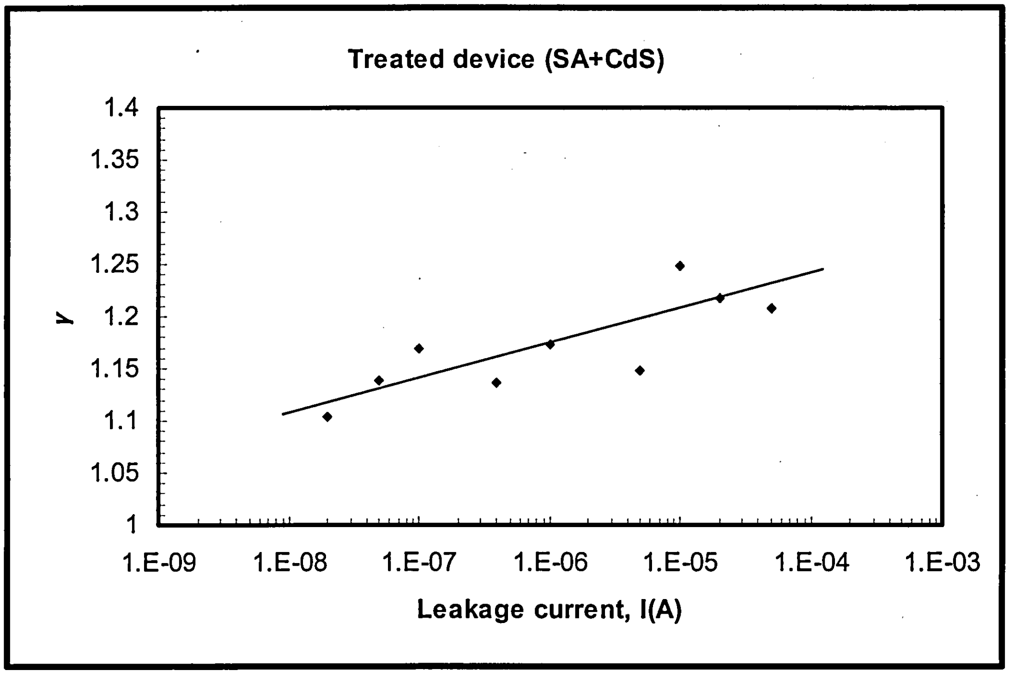

(b)

Figure 6.6. The dependence of exponent γ in the $1/f^{\gamma}$ spectrum on the bias current for frequency range 1 to 1 kHz for (a) untreated and (b) treated devices.

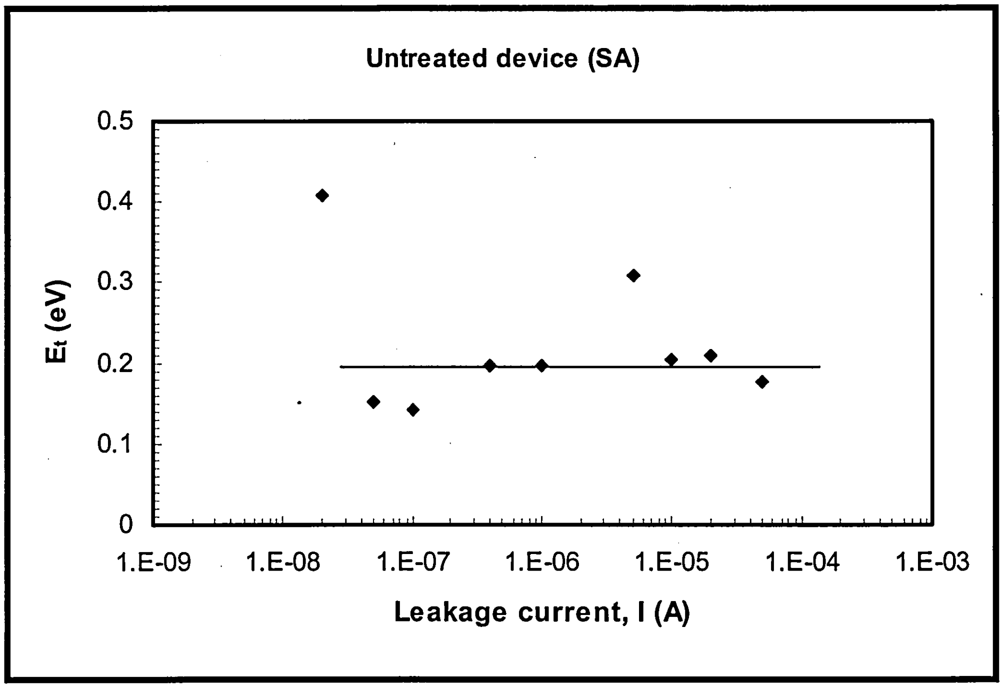

(a)

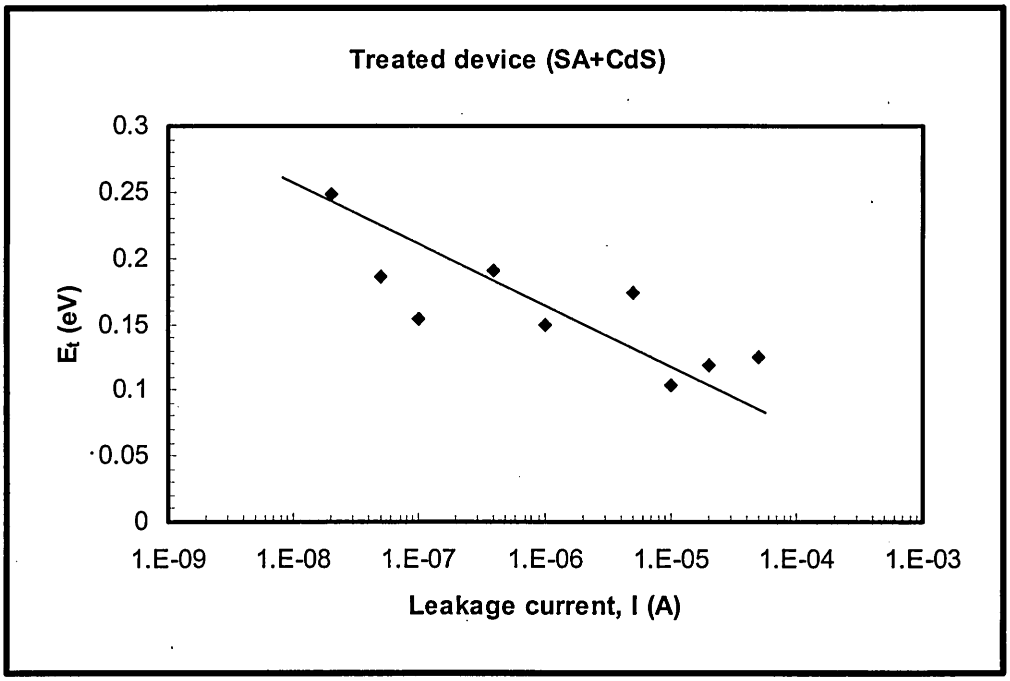

(b)

Figure 6.7. Trap distribution parameter, E_t as a function of leakage current for (a) untreated and (b) treated devices, corresponding to γ in fig.6.6.

By plotting the noise spectral density against dc leakage current at several fixed operating frequencies, a strong dependence on leakage current was observed for untreated devices as depicted in Figure 6.8. All measured spectra exhibited a simple two regions denoted as regime A and B. The two regimes observed were in accordance with the two current regimes in the I-V characteristics, as shown Figure 6.3. Regime A and B are in the depletion and accumulation region respectively. The bias dependence of the $1/f$ noise may reveal the location of the noise source(s). In the untreated device, the $1/f$ noise scale with $I^{2.7}$ when $I < 0.4\,\mu A$ and scale with I when $I > 0.4\,\mu A$. The constant β, was then extracted from the slope of the graph which gave two different values. For a current value below 0.4 uA (regime A), β is found to be approximately 2.7. For bias currents above $0.4\,\mu A$ (regime B), linear variation is observed with β approximately 1.

In regime A, since β deviates from the quadratic law ($\beta \approx 2.7$), it is believed that, more than one source of noise exist in this regime. It was also possible that the noise power could be a mixing of noise arising from resistance/conductance fluctuation in films, contacts, and bulk silicon substrate. The depletion in the silicon substrate, which controlled current in regime A, could be the major contribution of noise sources.

As the bias current increased into regime B, $S_I(f)$ scales with I. In this regime, the depletion region in the silicon substrate vanished and the current was believed to be controlled by the LB films. The $S_I(f)$ scaling with I was also found in organic-based devices. Martin et al. (2000) reported $\beta \approx 0.9$ for drain current in the saturation region of their organic thin-film transistors and proposed that the $1/f$ noise was due to carrier scattering occurring as surface trapping.

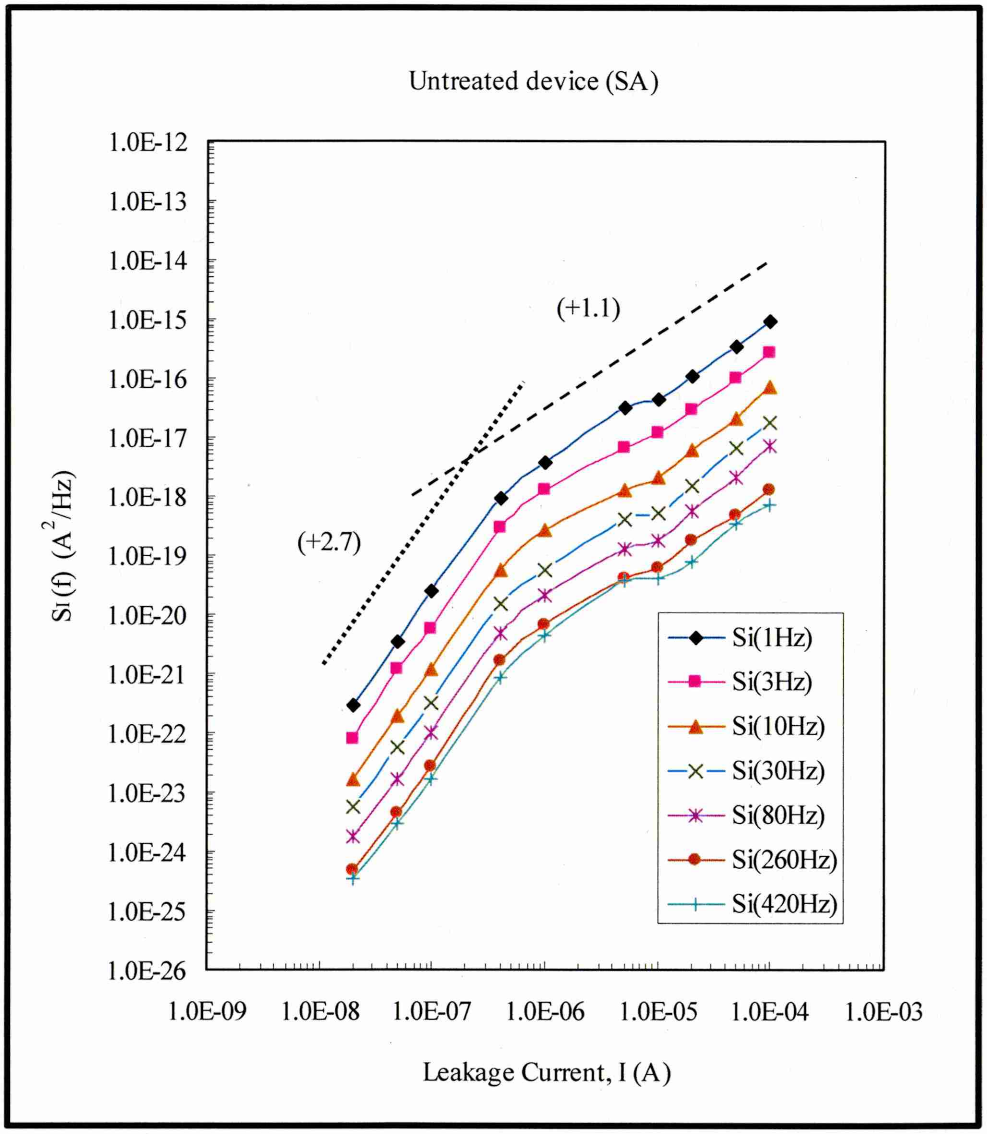

Figure 6.8. Current noise spectral density versus leakage current for untreated devices.

We believed that the $1/f$ noise, in our case, was dominated by the carrier-number fluctuation caused by electron hopping and tunnelling through the surface barrier in the LB films, which is a current transport mechanism in LB films of stearic acid [Sugi 1985]. It is suggested that in the LB films the origin of the noise could be due to fluctuation of the occupancy of the traps as the electron hoping from trap to trap. The interfacial barrier was believed to be responsible for the change in occupancy level of Poole type traps [Nathoo and Jonscher 1971]. The fluctuations of the carrier mobility (Δn) may have originated from the random nature of the hopping mechanism.

For a treated device, a linear change in the $1/f$ noise spectra was observed, as shown in Figure 6.9. These spectra were different from the untreated one. However since the aim of this work is to compare the noise behaviour of both devices, the same region which was used in analysing the $1/f$ spectra in untreated devices was followed for treated devices. In treated device, the $1/f$ noise scales with $I^{2.0}$ when $I < 0.4\,\mu A$ (regime A) and scales with $I^{1.6}$ when $I > 0.4\,\mu A$ (regime B). In the literature, the value of β can be found in the range of, $1.5 < \beta < 2.2$ in silicon diodes and $0.7 < \beta < 2.4$ for AlGaAs laser diodes [Chen 2001]. According to Van der ziel [1988] for $\beta \approx 1.5$ to 2, flicker noise was due to volume trapping. Since the $1/f$ noise spectra follows a quadratic law in regime A and a power of 1.6 in regime B, this might indicate that the noise source was from the bulk or volume. We suggest that in treated devices, the dominant noise source resides in the LB films which contains CdS nanoparticles.

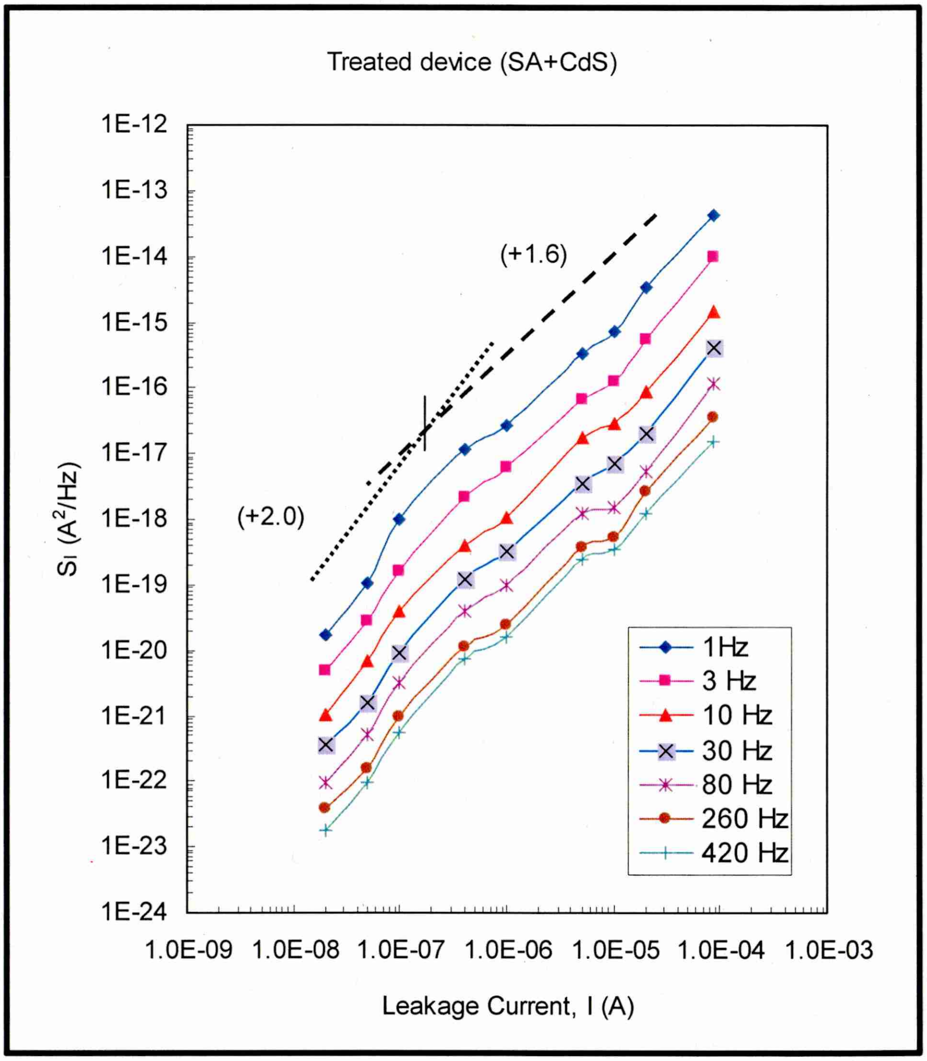

Figure 6.9. Current noise spectral density versus leakage current for treated device.

It is believed that by embedding the CdS nanoparticles in the stearic acid matrix, the film structure has changed from simple two dimensional (2D) to a complex 3D structure. Atomic Force Microscopy (AFM) images on similar samples which have been reported [Iwantono 2003] have shown the evidence of surface morphology differences for both devices (see Figure 6.12). A smooth stearic acid film surface has been observed for untreated samples while CdS nanoparticles with 20-30 nm in diameter and 2-3nm in thickness have been seen for treated samples. From LFNMs data it is believed that these nanoparticles have aggregated and become bigger clusters which give a volume effect of noise.

Equation 6.4 was used to characterise the $1/f$ noise magnitude (C) of the current noise spectral density. The results for both devices is shown in Figure 6.10 and 6.11 and were found to be 1.8×10^{-1} and 1.8×10^{-11} for regime A and B respectively for SA and 6.5×10^{-5} and 2.9×10^{-8} for SA+CdS. The results showed that the noise magnitude decreased when the forward bias current started to conduct in regime B. Celik-Butler et al. [Celik et al. 1987] have reported a similar behaviour in their n-MOSFETs devices. They found that the magnitude of the noise power decreases with gate bias.

It is also found that untreated device had higher noise magnitude in regime A than treated device. It is suggested that it was probably due to more than one noise source occurring in the untreated device at lower current range (regime A). Nevertheless, in general, untreated devices have lower noise magnitude than treated devices, as can be seen in regime B. It is believed that by embedding the CdS nanoparticles into the stearic acid matrix, electron trapping centres have been created which result in different conduction behaviour from the untreated devices [Malik et al. 2003], which give different values of noise parameters. For easy comparison between treated and untreated devices, the 1/f noise parameters and coefficients which have been extracted by using equation a, b and c are listed in Table 6.1.

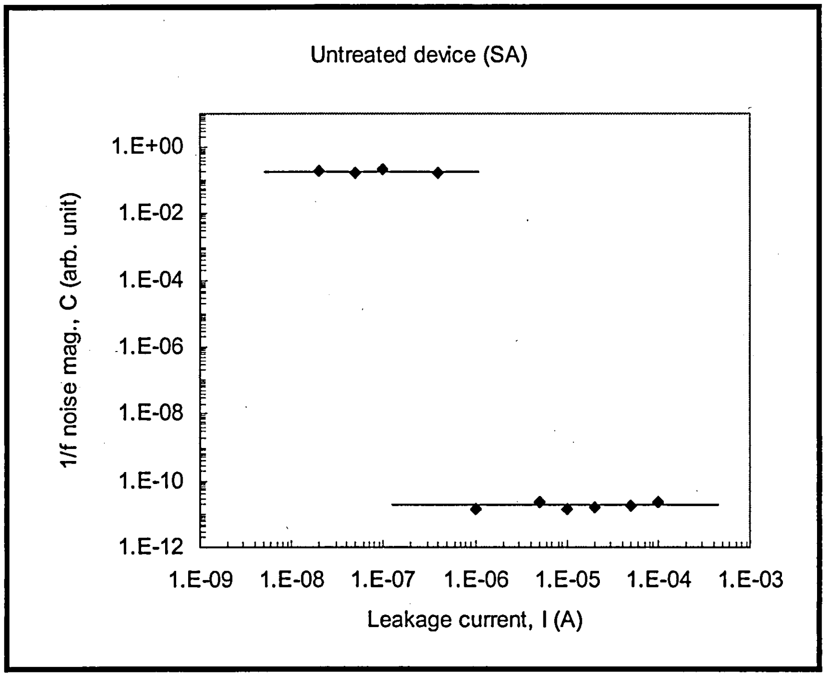

Figure 6.10. $1/f$ noise magnitude as a function of leakage current for untreated devices.

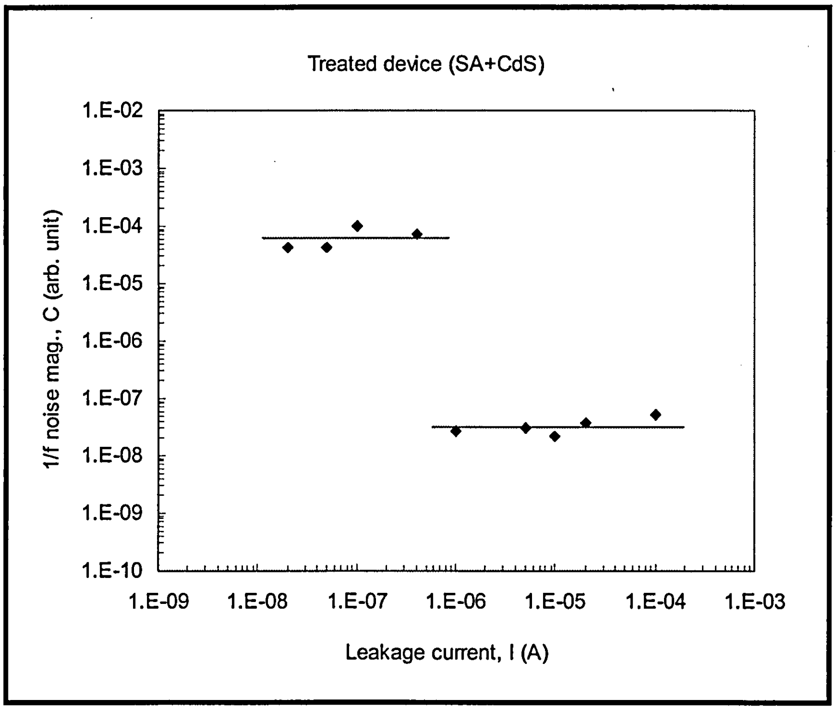

Figure 6.11. $1/f$ noise magnitude as a function of bias current for treated devices.

Current range	γ		β		$C_{1/f}$	
	SA	SA+CdS	SA	SA+CdS	SA	SA+CdS
20nA - 400nA	1.06-1.18	1.15-1.35	2.7	2.0	1.8×10^{-1}	6.5×10^{-5}
1uA - 50uA			1.0	1.6	1.8×10^{-11}	2.9×10^{-8}

Table 6.1. 1/f noise parameter for untreated (SA) and treated (SA+CdS) devices.

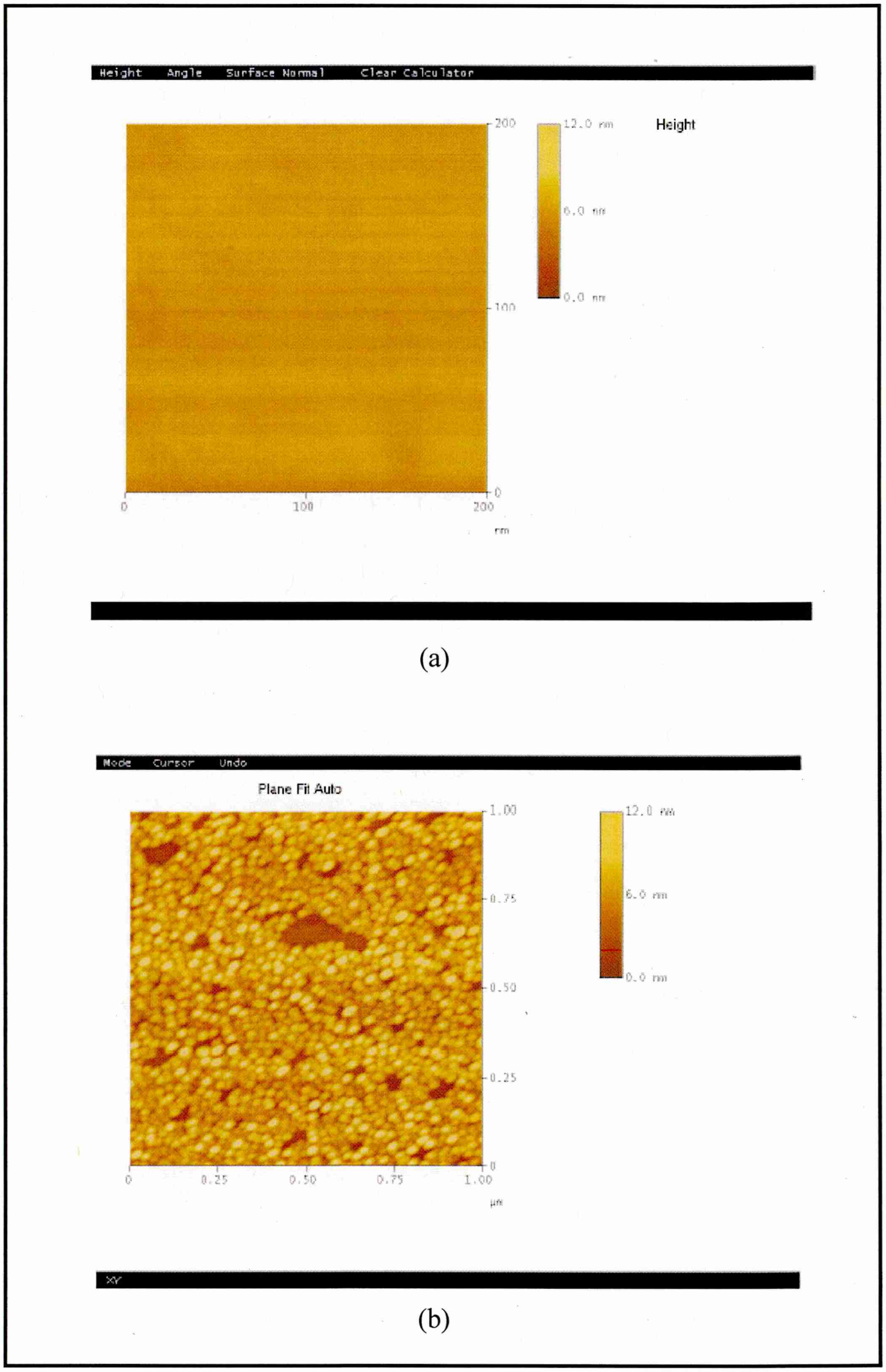

(a)

(b)

Figure 6.12 AFM image of 8-layer of Cd-salt LB films (a) before and (b) after H_2S treatment [after Iwantono 2003].

6.4 Summary

The works on low frequency noise studies in treated and untreated LB films of stearic acid on silicon substrate were done and the results were compared. The $1/f$ noise was found to be the only type of low frequency noise observed for both devices. Hooge empirical model was found to be invalid for this type of inhomogeneous materials. Instead a modified version of Hooge's model was used. The origin of the noise was found strongly dependence on the bias current range.

From the measurement data the $1/f$ noise parameters and coefficient have been extracted. The frequency exponent parameter γ was found to be lay close to unity but increases with biasing current when CdS nanoparticles were formed. Nevertheless the value for γ was still within an acceptable range for the noise to be classified as $1/f$ which is in the range of $0.7 \leq \gamma \leq 1.4$ [Butler et al. 1996]. On the other hand, the value for β for both devices was incomparable to that found in BJTs which is typically in the range $1 < \beta < 3$ [Leach 1994]. Flicker noise magnitude was higher in treated devices than in untreated devices. It is believed that energy trap density has increased by embedding the CdS nanoparticles into stearic acid matrix.

CHAPTER 7

Conclusions and Suggestions for Further Work

7.1 Thesis Summary

Two types of metal-insulator-semiconductor (MIS) capacitors based on hybrid organic-inorganic materials sandwiched between metal and semiconductor were fabricated. The insulators were 40 layers of Y-type Langmuir-Blodgett (LB) films of stearic acid incorporating cadmium ions (Cd^{2+}). This device is known as cadmium stearate ($CdSt_2$) LB films or untreated device. Prior to contacts formation, CdS nanoparticles were formed in the stearic acid matrix by exposing the cadmium stearate LB films to hydrogen sulphide (H_2S) gas for a period of 12 hours at room temperature. This sample is known as treated device. The substrate was n-type silicon (100) and aluminium films were used for metal contacts. Aluminium was used since it makes Ohmic contact with n-type silicon. The top and bottom electrical contacts were deposited by thermal evaporation technique. Care was taken when depositing the top metal contact in order to avoid damage to the LB films due to high temperature in the vacuum chamber and also to prevent LB films being short-circuited by the aluminium films.

Investigations of the electrical characterisations were performed on both devices by measuring the ac, dc and low-frequency noise properties. From the capacitance-voltage (C-V) characteristics, the capacitance of MIS capacitor of $CdSt_2$ LB films at accumulation region exhibits a significant dependence on measurement frequency with a drastic drop in capacitance at higher d.c. bias voltage. This was believed to be due to high d.c. leakage currents in the accumulation region. It was found that, by embedding

CdS nanoparticles into the stearic acid matrix, less frequency-dependent C-V curves were obtained. It is believed that CdS nanoparticles act as trap centres in the LB films which capture and release the electrons.

Since the accumulation capacitance of both devices was not totally independent of modulating frequency, a problem arises in the determination of the true insulator capacitance. Using Yang's model, which is widely used in determining the thickness of the ultra-thin oxide in MOSFETs, the true insulator capacitance was determined at the accumulation region and the corresponding dielectric constant was calculated through a simple capacitance equation. The dielectric constant of LB films of $CdSt_2$ and LB films of stearic acid embedded with CdS nanoparticles were found to be 2.3 and 5.1 respectively. The total surface state density was estimated to be $3.3 \times 10^{11}\,\mathrm{cm}^{-2}$ for $CdSt_2$ films and increased to $5.1 \times 10^{11}\,\mathrm{cm}^{-2}$ when incorporating CdS nanoparticles in the stearic acid matrix. The results from the dielectric loss measurement show that both devices agree well with the Goswami and Goswami model which explains the variation of $\tan\delta$ with frequency and the appearance of $\tan\delta_{\min}$ in the audio range frequency. By incorporating CdS nanoparticles in the stearic acid matrix, the dielectric loss was found to increase which could be due to electrons being trapped by the CdS nanoparticles.

The I-V characteristics of LB films of cadmium stearate MIS capacitor at room temperature showed exponential behaviour with large current density which gave the evidence of rectification behaviour of a leaky dielectric. The temperature dependent I-V characteristics as shown in figure 5.8 in section 5 for untreated devices, clearly shown that current is independent of temperature, in the accumulation region. These behaviours were similar to the results published by several researchers which explained the current conduction mechanism in term of electron hopping and tunnelling through each bilayer of the LB films. The large currents in the LB films were believed to be the reason for the drastic capacitance drop in the C-V measurements at the accumulation region. In contrast, the currents of the LB films of cadmium stearate after treatment to H_2S gas, were found to have reduced by one-order of magnitude. This was due to the fact that by embedding the CdS nanoparticles in the stearic acid matrix, the LB films resistance has increased as given in table 5.1. The temperature dependent of the I-V characteristics showed the dependence of current on the device temperature at low electric field densities. Less temperature dependence was observed at higher electric field density. Further investigation into the carrier transport mechanism, has found that the Poole-Frenkel effect was the dominant mechanism in the treated devices.

After completing the a.c. and d.c. electrical measurements, electrical current fluctuations in both devices were measured at room temperature for low-frequency noise characterisations. For this purpose, the low-frequency noise measurement (LFNM) system was designed and set-up. Before any measurement was made, the measurement setup was validated with respect to Johnson noise of the commercial resistors. The flicker or $1/f$ noise was the only low-frequency noise observed in both devices for frequency up to $1\,\text{kHz}$. The current noise power spectral density (PSDs) was found to be dependent on the bias current for both devices. The PSDs for treated devices were found to be approximately two-orders of magnitude higher than the untreated one although they were measured at the same bias current value. These results show that low-frequency noise measurement can probe into the microstructure of the electron devices. From the analysis of the PSD data, it was found that the Hooge mobility fluctuation and McWhorter number fluctuation models were invalid for both devices. This could be due to the fact that both carrier mobility and number of carrier fluctuations occurred simultaneously and not as a separated identity. The measurement data were found to fit well to a simple mathematical equation which is a modification of Hooge's empirical model. The $1/f$ parameters ($\gamma, \beta,$and C) for both devices were then extracted and compared. It was found that by embedding CdS nanoparticles into the stearic acid matrix, all parameters have increased which give evidence of different microscopic structure between the insulating films. The $1/f$ noise magnitude (C) for treated devices have increased to about three-orders of magnitude at higher bias current. It was believed that by embedding the CdS nanoparticles into the stearic acid matrix, electron trapping centres have been created which result in different current conduction behaviour from the untreated LB films of cadmium stearate.

7.2 Contribution to new knowledge

The research has produced several contributions to new knowledge of LB films of hybrid organic-inorganic materials which are listed below.

1. Improvement in the dielectric properties of hybrid composite LB films of $CdSt_2$ by incorporating CdS nanoparticles in the stearic acid matric films (nanocomposite). The dielectric constant has increased from 2.3 for a hybrid composite device to 5.1 for a hybrid nanocomposite device.

2. Identification of the carrier transport mechanism in hybrid nanocomposites films as Poole-Frenkel effect as apposed to hopping and tunnelling in the hybrid composite LB films of $CdSt_2$.

3. Quality assessment of hybrid composite and nanocomposite devices by LFNMs. The hybrid nanocomposite film has been found to be noisier than the composite one, due to the formation of nanoparticles in the stearic acid matrix.

4. Identification of the origin of low frequency noise in hybrid composite and nanocomposite devices. It was found that the $1/f$ noise in hybrid composite and nanocomposite devices is dependent on the bias current, where the dominant noise source in hybrid nanocomposite device is believed to reside in the LB films which contain CdS nanoparticles.

7.3 Suggestions for further work

The present investigation on the low-frequency noise measurement has given interesting results regarding to the hybrid organic-inorganic LB films with and without CdS nanoparticles, on silicon wafer. The findings are new and should contribute to new knowledge in electron devices especially in strengthening the application of the LB deposition technique. However, in order to obtain a better understanding of the low-frequency noise properties in the LB films, further experimental work needs to be done to improve this pioneering investigation and are listed here;

1. Further investigation should be done on treated and untreated devices at various temperatures from liquid nitrogen (77K) up to room temperature (300K).

2. With a better ultra low-noise amplifier and dynamic signal analyser the measurement setup can be made to measure the low-frequency noise in the μHz range.

3. The work should be expanded to other metal salts LB films and thus other metal-sulphide nanoparticles.

4. The work should be focused on the study of the fundamental physics of low-frequency noise in functional organic-inorganic materials such as Phthalocyanine (Pc) on silicon.

REFERENCES

Abdulkhadar, A., and Thomas, B., 1998, Nanostructured Materials, vol. 10(4), p.593

[**Agilent**], "Evaluation of MOS capacitor Oxide C-V Characteristics Using the Agilent 4294A", Product Note 4294-3, USA, Januari 14, 2002.

Alam M.S., 1991, "Capacitance Voltage Characteristics of Stearic Acid Insulating Films in MIS Devices" Conference on Electrical Insulation and Dielectric Phenomena, CEIDP, p.672.

Awan, S.A., and Gould, R.D., 2003, Thin Solid Films, vol. 423(2), p.267.

Bathaei, F.Z., and Anderson, J.C., 1987, Philos. Mag. B, vol. 55(87), p.87.

Beenakker, C. W. J., Kindermann, M., and Nazarov, Y.V., 2003, Phys. Rev. Lett. 90, art. no.176802

Bernamont, J., 1937, Proceedings of the Physical Society, vol. 49(4S), p.138.

Blecher, F., Seibel, K., and Bohm, M., 1998, MRS spring Meeting, San Francisco, April 13-17.

Briggs, A.T.R., and Stagg, J.P., 1988, Semicond. Sci. Technol., vol. 3(5), p.469.

Bruschi, P., Nannini, A., Serra G., and Stussi, E., 1996, Thin solid Films, vol. 289, p.242.

Burgess, R.E., 1955, Proceedings of the Physical Society, Section B, vol. 68(9), p. 661.

Bykov V.A., 1996, Biosensors & Bioelectronics, vol. 11, p.923.

Capan, R., "The pyroelectric effect in Langmuir-Blodgett films containing linear polysiloxanes", PhD Thesis, University of Sheffield, 1998.

Celik-Butler Z., and Hsiang T.Y., 1987, Solid-State Electronics, vol. 30(4), p.419.

Celik-Butler Z., Zhang R., and Patel N., 1996, Solid-StateElectron. Vol. 39, p.281.

Chand, S., and Kumar, J., 1996, J. Appl. Phys. vol. 80(1), p.288.

Chang, J.M., Abidi, A.A., and Viswanathan, C.R., 1994, IEEE T Electron Dev., vol. 41(11), p.1965.

Chen, F., Hoilien, N.P., and Campbell, S.A., 2004, Microelectronic Engineering, vol. 72(1-4), p.160.

Chen, X.Y., Deen, M.J., and Peng, C.X., 2000, J. Appl. Phys., vol. 88 (11), p. 6746.

Chen, X.Y., Pedersen,A., and van Rheenen, A.D., Microelectronics Reliability, vol. 41(1), 2001, p.105.

Chim, W.K., Ng, T.H., Koh, B.H., Choi, W.K., Zheng, J.X., Tung ,C.H., and Du, A.Y., 2003, J. Appl. Phys., vol. 93(8), p.4788.

Christensen, C. J., and Pearson, G. L., 1936, Bell System Technical J, vol. 15, p.197

Christensson, S., LundstrÄom, I., and Svensson, C., 1968a, Solid-State Electronics, vol. 11, p.797.

Christensson S., and LundstrÄom I., 1968b, Solid-State Electronics, vol. 11, p.813.

Ciofi C., and Neri B., 2000, J. Phys. D: Appl. Phys., vol. 33, p.R199.

Claeys C., and Simoen E., 1998, J. Electrochem. Soc., vol. 145(6), p.205.

Clerc R., Spinelli A.S., Ghibaudo G., Leroux C., and Pananakakis G., 2001, Microelectronics Reliability, vol. 41(7), p.1027.

Collins P.G., Fuhrer M.S., and Zettl A., 2000, Appl. Phys. Lett., vol. 76(7), p.894.

Crupi F., Iannaccone G., Ciofi C., Neri B., Lombardo S., and Pace C., 2002, Solid-State Electronics, vol. 46(11), p. 1807.

Depas M., Vermeire B., Mertens P.W., Vanmeirhaeghe R.L.,and Heyns M.M., 1995, Solid State Electron, vol.38(8), p.1465.

Dhanabalan A., Kudrolli H., Major S.S., and Talwar S.S., 1996, Solid State Comms, vol. 99(11), p.859.

Dobrzanski L., J. Appl. Phys., 2004, vol. 96(8), p.4135.

Dutta P., and Horn P. M., 1981, Rev. Mod. Phys., vol. 53, p.497.

Elliot D.J., Neil Furlong D., and Grieser F., 1999, Colloids and Surfaces A: Physico-chemical and Engineering Aspects, vol.155, p.101.

Erokhin V, Feigin L, Ivakin G, Klechkovskaya V, Lvov Y, and Stiopina N, 1991, Makromol Chem-M Symp, vol. 46, p.359.

Erokhin V., Facci P., Carrara S., and Nicolini C., 1995, J. of Phys. D: Appl. Phys, vol. 28, p.2534.

Erokhin V., Facci P., Gobbi L., Dante S., Rustichelli F., and Nicolini C., 1998, Thin Solid Films, vol. 327-329, p.503.

Evangelos K., Stelios G., and Evangelou S.N., 1997, Nonlinear Analysis, vol. 30(4), p.2007.

Facci P., Erokhin V., Tronin A., and Nicolini C., 1994, J. Phys. Chem., vol. 98, p.13323.

Ferrari G., Natali D., Sampietro M., Wenzl F.P., Scherf U., Schmitt C., Güntner R., and Leising G., 2002, Organic Electronics, vol. 3(1), p.33.

Fox A.M., 1996, Contemporary Physics, vol. 37(2), p.111.

Frenkel, J., 1938, J. Phys. Rev., vol. 54, p.647.

Gardner, M., 1978, Scientific American, vol. 4, p.16.

Gerard, L., Joel, G. and Pierre, T., 2001, Fluctuation and Noise Letters, vol. 1(3) , p.L125.

Ghibaudo, G., Clerc, R., Vincent, E., Bruyere, S., and Autran, J.L., 2000, CR Acad Sci IV-Phys, vol. 1(7), p.911.

Ginnai, T.M., Oxley, D.P., and Pritchard, R.G., 1980, Thin Solid Films, vol. 68, p.241.

Goswami, A., and Goswami, Amit, P., 1973, Thin Solid Films, vol. 16, p.175.

Gould, R.D., and Ismail, B.B., 1998, Vacuum, vol. 50(1-2), p.99.

Gould, R.D., and Lopez, M.G., 1999, Thin Solid Films, vol. 344, p.94.

Gould, R.D., Awan, S.A., 2004, Thin Solid Films, vol. 469(70), p.184.

Grieser, F., Furlong, D.N., Scoberg, D., Ichinose, I., Kimizuka, N., and Kunitake, T., 1992, J. Chem. Soc. Faraday T, vol. 88 (15), p.2207.

Grunfeld, F., 1993, Rev. Sci. Instrum. vol. 64 (2), p.548.

Gunes, M., Jahanson, R.E., and Kasap, S.O., 2000, Journal of Non-Crystalline Solids, vol. 266-269, p.304.

Gupta, P., Pal R., Bhattacharyyya, D., Chaudhuri, S., and Pal, A.K., 1995, Phys. Stat.Sol., vol. 148, p.459.

Haddab, Y., Friedrich, A.P., and Popovic, R.S., 1999, Solid-State Electronics, vol. 43, p.413.

Hajji, B., Temple-Boyer, P., Olivie, F., and Martinez, A., 1999, Thin Solid Films, vol. 354 (1-2), p.9.

Harrell, W.R., and Frey, J., 1999, Thin Solid FIilms, vol. 352(1-2), p.195.

Harrell, W.R., and Gopalakrishnan, C., 2002, Thin Solid films, vol. 405, p.205.

Hastas, N.A.,. Dimitriadis, C. A, Panayiotatos, Y.,. Tassis, D. H, Patsalas, P., and Logothetidis, S., 2000, J. Appl. Phys. vol. 88, p.5482.

Herzog, G.B., and van der Ziel, A., 1951, Phys. Rev., vol. 84, p.1249.

Hoel, A., Vandamme, L.K..J, Kish, L.B.., Olsson, E, J. Appl. Phys., vol. 91(8), 2002, p.5221.

Hooge, F.N., Phys. Lett. A, 1969, vol. 29A, p.139.

Hooge, F.N., 1976, Physica B, vol. 83, p.14.

Hooge, F.N., IEEE Transactions on Electron Devices, 1994, vol. 1(11), p.1926.

Hooge, F.N., and Hoppenbrouwers, A.M.H., 1969, Physica A, vol. 45, p.386.

Hooge, F.N., and Kleinpenning, T.G.M., 1975, Appl. Phys. Lett., vol. 27(3), p.160.

Hooge, F.N., Kleinpenning, T.G.M., and Vandamme, L.K.J., 1981, Reports of Progress of Physics, vol. 44, p.481.

Houston, G.L.B., Chen, Y., Singleton, J., Mason, N.J., and Walker, P.J., 1997, Semicond. Sci. technol., vol. 12, p.1140.

Hsu, S.T., 1970, Solid-State Electronics, vol. 13(11), p.1451

Huang, J., Yang, Y., Xue, S., Yang, B., Liu, S., and Shen, J., 1997, Appl. Phys. Letts., vol. 70(18), p.2335.

[ITRS]- http://www.itrs.net/

Iwantono, B., 2003, "Studies on Cadmium Sulphide Nanoparticles formed by the Langmuir-Blodgett technique", PhD Thesis, Sheffield Hallam University.

Jamal, M.D., Marinov, O., Jianfei, Y., Steven, H., and Woods, W., 2001, IEEE Trans. Electron Devices, vol. 48 (8), p.1688.

Jang, S.L., and Wu, J.Y., 1993, Solid-State Electronics, vol. 36(2), p.189.

Jason, R.D., 2002, Current Opinion in Colloid & Interface Science, 7, p.186.

Jevtic, M.M, 1995, Microelectro. Reliab., vol. 35(3), p.455.

Johanson, R.E., Scansen, D., and Kasap, S.O., 1996, Philos Mag B, vol. 73(4), p.707.

Johnson, J., 1928, Phys. Rev. vol. 32, p.97.

Jonscher, A.K., 1977, Nature, vol. 267, p.673.

Jonscher, A.K., 1967, Thin Solid Films, vol. 1, p.213.

Kajzar, F., Girling, I.R., and Peterson, I.R., 1988, Thin Solid Films, vol. 160, p.209.

Kasap, S.O., 1997, "Principles of Electrical Engineering Materials and Devices", McGraw-Hill, New York,

Kasilingam, A.R., Balasubramanian, C., and Radhakrishnan, M., 1980, J. Phys. D: Appl. Phys., vol. 13(5), p.853.

Klaassen, F.M., 1971, IEEE Transactions on Electron Devices, vol. 18(10), p.887.

Kleinpenning, T.G.M., 1976, J. Phys. Chem. Solids, vol. 37, p.925.

Kleinpenning, T.G.M., 1985, Journal of Vacuum Science & Technology A, vol. 3, p.176.

Kleinpenning, T.G.M, 1998, J. Phys.: Condens. Matter., vol. 10, p.4245.

Kochowski, S., Paszkiewicz, B., and Paszkiewicz, R., 2000, Vacuum, vol. 57(2), p.157.

Kogan, S.H., 1996, "Electronic Noise and Fluctuations in Solids", Cambridge University Press.

Kohn, E., and Hartnagel, H.L., 1977, Solid State Electron. Vol. 21, p.409.

Kurdak, C., Kim, J., Kuo, A., Lucido, J.J., Farina, L.A., Bai, X., Rowe, M.P., and Matzger, A.J., 2005, Appl. Phys. Letts., vol. 86 (7), art. no. 073506.

Kwa, K.S.K., Chattopadhyay, S., Jankovic, N.D., Olsen, S.H., Driscoll, L.S., and O'Neill, A.G., 2003, Semicond. Sci. Tech., vol. 18(2), p.82.

Lamb, D.R., "1967, Electrical conduction mechanisms on thin insulating films", Mathuen and Co. Ltd, London.

Lambert, B., Malbert, N., Verdier, F., Labat, N., Touboul, A., and Vandamme, L.K.J., 2001, IEEE Trans. Electron Devices, vol. 48(4), p. p.628.

Lampert, M.A., 1964, Rep. Prog. Phys., vol. 27, p.329.

Lay, T.S., Hong, M., Kwo, J., Mannaerts, J.P., Hung, W.H., and Huang, D.J., 2001, Solid State Electron, vol. 45(9), p.1679.

Leach, M.W.jr., 1994, Proc. IEEE, Vol. 82(10), p.1515.

Lee, J., and Bosman, G., 2003, Solid-State Electronics, vol. 47(11), p.1973.

Lenzlinger, M., and Snow, E.H., 1969, vol.40(1), p. 278.

Liang, E.Z., and Lin, C.F., 2001, IEEE-NANO, p.363.

Li, H., Mao, G., and Ng, K.Y.S, 2000, Thin Solid Films, vol. 358(1-2), p.62.

Lin, T. K., 1990, Chinese Journal of Physics, vol. 27(5), p.351.

Logothetidis, S., Evangelou, E., and Konofaos, N., 1997, J. Appl. Phys., vol. 82(10), p.5017.

Lu, X.B., Liu, Z.G., Wang, Y.P., Yang, Y., Wang, X.P., Zhou, H.W., and Nguyen, B.Y., 2003, J. Appl. Phys., vol. 94(2), p.1229.

Lukyanchikova, N.B., 1997 "Noise Research in Semiconductor Physics", IoP, London.

Lvov, Y.M., and Decher, G., 1994, Kristallografiya, vol. 39(4), p.628.

Machlup, S., 1981, "Earthquakes, Thunderstorms, and Other 1/f Noises. In:Sixth International Conference on Noise in Physical Systems", Meijer P.H.E., Mountain R.D., Soulen R.J.Jr., (Eds), National Bureau of Standards-Special Publication, vol. 614, p.157.

Mahantappa, S.J., and Ducharme, S., 2002, Current Science, vol. 83(4), p.472.

Mann, B., and Kuhn, H., 1971, J. Appl. Phys., vol. 42, p.4398.

Marinov, O., Deen, M.J., Yu J., Vamvounis, G., Holdcroft, S., and Woods, W., 2004, Nanoelectronics, IEE Proc. Circuits Devices Syst., vol. 151(5), p. 466.

Martin, P., and Szablewski, M., 1995, "Tensiometers and Langmuir-Blodgett Throughs Operating Manual", Nima, Cranfield University Milton Keynes, England.

Martin, S., Dodabalapur, A., Bao, Z., Crone, B., Katz, H.E., Li, W., Passner, A., and Rogers, J.A., 2000, J. Appl. Phys., vol. 87(7), p.3381.

Mayya, K.S., Patil, V., Kumar, P.M., and Sastry, M., 1998, Thin Solid Films, vol. 312(1-2), p.300.

McWhorter, A.L., 1955, Massachusetts Institute of Technology Tech. Rep. No. 295.

McWhorter, A.L., 1956, "1/f noise and related surface effects in germanium", in Semiconductor Surface Physics, ed. Kingston R.H., Univ. Penn. Press.

McWhorter, A.L., 1957, "1/f noise and germanium surface properties", in Semiconductor Surface Physics, Univ. Pennsylvania Press, p.207.

Meiners, L.G., 1978, J.Vacuum Science and Technology, vol. 15(4), p.1402.

Min, B.G., Devireddy, S.P., Celik-Butler, Z., Shanware, A., Green, K., Chambers, J.J., Visokay, M.V., and Colombo, L., 2005, Appl. Phys. Letts., 86 (8), art. no. 082102.

Montgomery, H.C., 1952, Bell System Tech. J., vol. 31, p.950.

Mott, N.F., and Gurney, R.W., 1940, "Electronic Processes in Ionic Crystals", Oxford University, New York,

Motchenbacher C.D., and Connelly J.A., 1993, "Low-Noise Electronic System Design", John Wiley & Son, New York.

Murgatroyd, P.N., 1970, J. Phys. D: Appl. Phys., vol. 3, p.1488.

Nabok, A.V., Richardson, T., McCartney, C., Cowlam, N., Davis, F., Stirling, C.J.M., Ray, A.K., Gacem, V., and Gibaud, A., 1998, Thin Solid Films, vol. 327-329, p.510.

Nabok, A.V., Ray, A.K., Hassan, A.K., Titchmarsh, J.M., Davis, F., Richardson, T., Starovoitov, A., and Bayliss, S., 1999, Mat. Sci. Eng. C: Bio. S., vol. 8-9, p.171.

Nabok, A.V., Iwantono, B., Hassan, A.K., Ray, A.K., and Wilkop, T., 2002, Materials Science and Engineering C, vol. 22, p.355.

Nabok, A.V, Ray, A.K, Iwantono, B., Hassan, A.K., and Simmonds, M,. 2003, IEEE Transactions on Nanotechnology, vol. 2(1), p.44.

Nataraj, D., Senthil, K., Narayandass, S.A.K., and Mangalaraj, D., 1999, Cryst. Res. Technol., vol. 34(7), p.867.

Nathoo, M.H., and Jonscher, A.K., 1971, Journal of Physics C: Solid State Physics, vol. 4(15), p.L301.

Nauen, A., Hohls, F., and Könemann, J., and Haug R.J., 2004, Phys. Rev. Vol. 69, art. no. 113316

Necliudov, P.V., Rumyantsev, S.L., Shur, M.S., Gundlach, D.J., and Jackson, T.N., 2000, J. Appl. Phys., vol. 88(9), p.5395.

NI application note 041, by **Cerna, M., and Harvey, A.F.**, http://alpha.science.unitn.it/~bassi/Signal/NInotes/an041.pdf

Nyquist, H., 1928, Phys. Rev., vol. 32, p.110.

O'Dwyer, J.J., 1973, "The Theory of Electrical Conduction and Breakdown in Solid Dielectrics", Clarendon Press, Oxford.

Oliva, A. I., Castro-Rodríguez, R., Ceh, O., Bartolo-Pérez, P., Caballero-Briones, F., and Sosa, V., 1999, Applied Surface Science, vol. 148 (1-2), p.42.

Otten F., Kish L.B., Granqvist C.G., Vandamme L.K.J., Vajtai R., Kruis F.E., and Fissan H., 2000, Appl. Pyhs. Lett., vol. 77(21), p.3421.

Ouacha H., Willander M., Yu H.Y., Park Y.W., Kabir M.S., Persson S.H.M., Kish L.B., and Ouacha A., 2002, Appl. Phys. Lett., vol. 80(6), p.1055.

Ouennoughi Z., 1997, Phys Status Solidi, A vol. 160 (1), p.127.

Pavelka, J., Sikula, J., Vasina, P., Sedlakova, V., Tacano, M., and Hashiguchi, S., 2002, Microelec. Reliab. vol. 42(6), p.841.

Pearson, C, Dhindsa, A.S., Petty, M.C., and Bryce, M.R., 1992, Thin Solid Films, vol. 210(1-2), p.257.

Peterson, I. R., 1990, Langmuir-Blodgett films: Review article, J. Phys. D: Appl. Phys., vol. 23, p.379.

Petty, M.C., 1991, J. Biomed. Eng., vol. 13(3), p.209.

Petty, M.C., Bryce, M.R., and Bloor, D., 1995, "Introduction to Molecular Electronics", Edward Arnold, London, p.244.

Petty, M.C., 1996, "Langmuir-Blodgett Films: An Introduction", Cambridge University Press

Petty, M.C., Pearson C., Monkman, A..P, Casalini, R., Capaccioli, S., and Nagel, J., 2000, Colloid Surface A, vol. 171(1-3), p.159.

Pillonnet, A., and Ongaro, R, 1989, Rev. Phys. Appl., vol. 24(1), p.109.

Polymeropoulos, E.E., 1977, J. Appl. Phys. vol. 48, p.2404.

Ramanathan, S., Park, C.M., and McIntyre, P.C., 2002, J Appl. Phys., vol. 91(7), p.4521.

Ravindra, N.M., and Zhao, J., 1992, Smart Mater. Struct. Vol. 1, p.197.

Rhayem, J., Rigaud, D., Valenza, M., Szydlo, N., and Lebrun, H., 2000, J. Appl. Phys. vol. 87, p.1983.

Rhoderick, E.H., and Williams, R.H., 1988, "Metal –Semiconductor Contacts", 2nd ed., Clarendon Press, Oxford.

Richardson, T.; 1995, **"An Introduction to Molecular Electronics"**, edited by M.C Petty, Edward Arnold Publishers.

Roberts, G.G., 1990, Ed. Langmuir-Blodgett Films, Plenum Press, New York.

Roberts, G.G., McGinnity, T.M., Barlow, W.A., and Vincett, P.S., 1980, Thin Solid Films, vol. 68, p.223.

Roberts, G.G., Vincett, P.S., and Barlow, W.A., 1978, J. Phys. C: Solid State Phys., vol. 11, p.2077.

Roth, K.M.; Gryko, D.T., Clausen, C., Li J., Lindsey, J.S., Kuhr W.G., and Bocian, D.F., 2002, J. Phys. Chem. B. vol. 106(34), p.8639.

Salata, O.V., Dobson, P.J., Sabesan, S., Hull, P.J., and Hutchison, J.L., 1996, Thin Solid Film, vol. 288, p.235.

Schottky, W., 1918, Ann. Phys., Leipzig, vol. 57, p.541.

Samokhvalov, A., Gurney, R.W., and Lahav, M., 2002, J. Phys. Chem. B., vol. 106(35), p.9070.

Sanchez, J. E., and Bosman, G., 2000, Microelectronics Reliability, vol. 40(11), p.1839.

Sharpe, R.G., and Palmer, R.E., 1996, Thin Solid Films, vol. 288(1-2), p.164.

Simmons, J.G., 1970, "Handbook of Thin Film Technology", ed. Maissel L.I., and Glang R., McGraw-Hill, New York.

Simoen, E., Bosman, G., Vanhellemont, J., and Claeys, C., 1995, Appl. Phys. Lett., vol. 66(19), p.2507.

Singh, J., 2001,"Semiconductor devices : basic principles", Wiley, New York .

Singh, R., and Hartnagel, H.L., 1975, "Reduction in surface charge density by new GaAs passivation method", J. Phys. D: Appl. Phys., vol. 8, p.L42.

Streetman, B.G., and Banerjee, S., 2000, "Solid State Electronic Devices" 5th edition, New Jersey, Prentice Hall.

Sugi, M., 1985, J. Mol. Electron. vol. **1**, p.3.

Sugi, M., Fukui, T., and Iizima, S., 1975, Appl. Phys. Lett. vol. 27, p.559.

Sugi, M., and Iizima, S., 1979, "Single layer conductance of cadmium behenate in the Langmuir multilayer assembly system", Appl. Phys. Lett. vol. 34(4), p.290.

Sugi, M., Nembach, K., Möbius, D., and Kuhn, H., 1974, Solid State Comms., vol.15, p.1867.

Stroeken, J.T.M., and Kleinpenning, T.G.M., 1976, J. Appl. Phys., vol. 47(10), p.4691.

Staffan B., 1999, "Silicon Germanium Heterojunction Bipolar Transistors: Large-SIGNAL modeling and Low-Frequency Noise Characterization Aspects", PhD Thesis, University of Uppsala, Sweden,

Swalen, J.D., Allara, D.L, Andrade, J.D., Chandross, E.A., Garoff, S., Israelachvili, J., McCarthy, T.J,, Murray, R., Pease, R.F., Rabolt, J.F., and Wynne, K.J., Yu, H., 1987, Langmuir vol. 3(6), p.932.

Sze, S.M., 1981, “Physics of Semiconductor Devices”, 2nd. edition, John Wiley & Sons, New York,

Takagi, S., Yasuda, N., and Toriumi, A., 1999, IEEE Trans. Electron Dev., vol. 46(2), p.335.

Takanashi, Y., and Fukano, H., 1998, IEEE Trans. Electron Dev., vol. 45(12), p.2400.

Taneja, T., Vasa, P., and Ayyub, P., 2002, Materials Letters, vol. 54, p.343.

Thamilselvan, M., PremNazeer, K., Mangalaraj, D., Narayandass, S.K., and Yi, J.S., 2004, Materials Research Bulletin, vol. 39(12), p.1849.

Tredgold, R. H., 1966, “Space Charge Conduction in Solids”, Elsevier, Amsterdam.

Tredgold, R.H., and Winter, C.S., 1981, J. Phys. D: Appl. Phys., vol. 14, p.L185.

Tredgold, R.H., Jones, R., Evans, S.D., and Willams, P.I., 1986, J. Mol. Electron. vol. 2, p.147.

Tredgold, R.H., Vickers, A.J., and Allen, R.A., 1984, J. Phys. D: Appl. Phys., vol. 17(1), p.L5.

Trindale, T., 2001, Chem. Mater., 13, p.3843.

Van der Ziel, A., 1976, "Noise in Measurements" John Wiley & Sons

Van der Ziel, A., 1986, “Noise in Solid State Devices and Circuits”, Wiley.

Van der Ziel, A., 1988, Proceedings of the IEEE, vol. 76(3), p.233.

Vandamme, L.K.J., 1974, Journal of Applied Physics, vol. 45(10), p.4563

Vandamme, L.K.J., Feyaerts, R., Trefan G., Detcheverry, C., 2002, J. Appl. Phys., vol.91(2), p.719.

Viktorovitch, P., Rojo-Romeo, P., Leclercq, J.L., Letartre, X., Jacques, T., Oustric, M., and Gendry M., 1996, IEEE Transactions on Electron Devices, vol. 43(12), p.2085.

Voss, R.F., and Clarke, J., 1978, Journal of the Acoustical Society of America, vol. 63(1), p.258.

Werkman, P.J., 1998, “Langmuir-Blodgett film formation of polymerisable amphiphilic metal complexes: a structural investigation”, Ph.D Thesis, University of Groningen, Netherland.

Werner, A., Blochwitz, J., Pfeiffer, M., and Leo, K., 2001, J. Appl. Phys. Vol. 90, p.123.

Wieczorek, H., 1995, J. Appl. Phys., vol. 77(7), p.3300.

Wu, Y., Chen, Q., Takeguchi, M., and Furuya, K., 2000, Surface Science, vol. 462, p.203.

Wong, H., 2003, Microelectron. Reliab., vol. 43(4), p.585.

Yang, B. L., Lai, P. T., and Wong, H., 2004, Microelectronics Reliability, vol. 44(5), p.709.

Yang, K.J., and Hu, C., 1999, IEEE Trans. Electron Devices, vol. 46(7), p.1500.

Yang, X.M., Wang, G.M., and Lu, Z.H., 1998, Supramolecular Science, vol. 5(5-6), p.549.

Zhang, H., Ma, X., Xu, J., Sha, J., and Yang, D., 2002, Journal of Crystal Growth, vol. 246, p.108.

Zhao, E., Celik-Butler, Z., Thiel, F., and Dutta, R., 2004, Microelectron. Reliab., vol. 44(1), p.89.

Zhavnerko, G.K., Gurin, V.S., Rogach, A.L., Gallyamov, M.O., and Yaminsky, I.V., 1999, J. Inclusion Phenomena and Macrocyclic Chem., vol. 35(1-2), p.157.

Zhu, J., and Liu, Z.G., 2003, Microelectronic Engineering, vol. 66(1-4), p.849.

Zhu, J., Liu, Z.G., Zhu, M., Yuan, G.L., and Liu, J.M., 2005, Appl. Phys. A: Mater., vol. 80(2), p.321.

Zylberajch, C., Ruaudelteixier, A., Barraud, A., 1988,Synthetic Met., vol. 27(3-4), p.B609.